Developing Novel STING-activating Metalloimmunotherapy

By

Xiaoqi Sun

A dissertation submitted in partial fulfillment
of the requirements for the degree of
Doctor of Philosophy
(Pharmaceutical Sciences)
in The University of Michigan
2021

Doctoral Committee

Professor James J. Moon, Chair
Associate Professor Yu Leo Lei
Professor David H Sherman
Professor Duxin Sun
Professor Peter Matthew Tessier

Xiaoqi Sun
sunxqi@umich.edu
ORCID iD 0000-0003-0752-1928

Dedication

To my grandfather, Yizhen Sun, Uncle Youjun Ren, whose strength and struggle with cancer encouraged the research documented within

To my parents Lichun Sun and Jianli Hu, and parents-in-law Xia Hua and Wei Chao

To my wife Tianyi Hua

Acknowledgments

First, I would like to thank my advisor and role model, Dr. James Moon. I am very grateful to become Dr. Moon's student. Over the past five years, Dr. Moon has given me a lot of freedom/support to try various new ideas and explore different projects. He is always available with patience to help and support me when I had questions or even made mistakes. Such balanced freedom and support make me really enjoy the time and research in the lab. Dr. Moon has also guided me to grow into an independent scientist and provided me many opportunities to practice scientific papers/grant proposals writing, oral presentations, and developing collaborations. His training, guidance, and investment in me have greatly shaped my science attitude and thinking. What I learned from him would be part of my academic DNA and valuable assets for me forever. I really appreciate it.

Second, I would like to thank other committee members: Dr. Yu Leo Lei, Dr. David H Sherman, Dr. Duxin Sun, and Dr. Peter Matthew Tessier. Dr. Lei is not only a good committee member but also a wonderful collaborator and mentor. He has provided me a lot of immunological insights and technical support for my projects. Dr. Sherman has provided me a lot of help on high-throughput screening of microbial metabolites for new STING agonists discovery. Dr. Sun and Dr. Tessier have given me many valuable

suggestions and comments from the very beginning of my projects, which helped me better understand and improve my research.

Third, I would like to thank all of my lab members, Yao Xu, Xingwu Zhou, Charles Park, Xuehui Huang, Rui Kuai, Marisa Aikins, Yu Zhang, Kai Han, Jutaek Nam, Cheng Xu, Xiaoyue Shi, Xinran An, Jin Xu, Sejin Son, Emeka Okeke, Lindsay Scheetz, Ali Hassani and so on. I am sorry that I cannot list all the names here, but please know that I am very grateful for being able to work with you and I really appreciate help from you. My experiments would not have succeeded without you.

Fourth, I would like to thank all of the collaborators, core facility staff, veterinary staff, and the COP administrators. I would especially like to thank Jiaqian (Leah) Li and Wang Gong for help on western blotting experiments, NOOC1 tumor studies and single-cell analysis. I would like to thank Dr. Osama Mohamed and Dr. Ashu Tripathi from UM Natural Drug Discovery Core for close collaboration on the HTS project and helps on microbe regrow, natural products isolation and analysis. I also would like to acknowledge Justin Hong for aiding with isothermal titration calorimetry (ITC) analysis, Angela Dial at Michigan Element Analysis Lab for Mn biodistribution analysis, Krishnapriya Chinnaswamy at University of Michigan Center for Structural Biology for aiding with protein thermal shift assay, Joel Whitfield at the University of Michigan Cancer Center Immunology Core for ELISA analysis, Dr. Carlson Heather at University of Michigan for molecular dynamic analysis, and Taryn Hetrick at ULAM for assistance on animal monitoring.

Fifth, I would like to thank all my friends and the other wonderful people I met in the College of Pharmacy, University and Ann Arbor. I would like to thank Hongxiang Hu,

Minzhi Yu, Lucy Her and Justin Hong for their tremendous help and friendship. Thank you for the relaxing happy hours and hotpots throughout the past five years.

Finally, I would like to give special thanks to my family. To my dear wife, Tianyi Hua, thank you for your love and your warm support for my work, career passion and every decision I made. I am so grateful to meet kind you in Ann Arbor and travel together to many memorable places. I love you so much! To my parents and parents-in-law, thank you for your constant unconditional support for Tianyi and me!

Table of Contents

List of Figures

Abstract

Nutritional metal ions play critical roles in many important immune processes. Hence, effective modulation of metal ions may open up new forms of immunotherapy, termed as metalloimmunotherapy. The immunology studying how the metal ions regulate immune processes is defined as metalloimmunology. In the introduction, I firstly reviewed metalloimmunology from three aspects: 1) metal ions' role in innate immunity, 2) metal ions' role in adaptive immunity, and 3) metal ions' role in host-microbe interface. The mechanisms of metal ion-mediated immune modulation have been unraveled and summarized accordingly. Next, I systematically reviewed the status of metalloimmunotherapy and categorized metalloimmunotherapy into five categories: 1) metal supplement for immune modulation; 2) metal ion-mediated immune cell reprogramming for cell therapy; 3) metal-based vaccine adjuvants; 4) synergistic metal ion-drug combination for immunotherapy; 5) metallodrug-induced immunogenic cell death for cancer immunotherapy. The purpose is to provide a route map for metalloimmunotherapy development.

In the first project, I discovered cobalt (Co^{2+}) and manganese (Mn^{2+}) metal ions augmented Stimulator of Interferon Genes (STING) agonist activity, wherein Mn^{2+} promoted a 12- to 77-fold potentiation effect across the prevalent human STING haplotypes. CDA + Mn^{2+} combination significantly amplified STING activation, increased

antigen-presenting cell activation, induced antigen-specific T cell response, leading to complete regression of 80% CT26 tumors after IT injection. The survivors also formed an immune memory against second CT26 re-challenging.

In the second project, I demonstrate a prototype of effective cancer metalloimmunotherapy using cyclic dinucleotide (CDN) STING agonists and Mn^{2+} in an optimized pharmaceutical formulation. Notably, I have found Mn^{2+} coordinates with CDNs to self-assemble into a nanoparticle (CDN-Mn^{2+} particle, CMP) that effectively delivered STING agonists to immune cells. CMP administered by either local intratumoral or systemic intravenous injection initiated robust anti-tumor immunity, achieving remarkable therapeutic efficacy with minute doses of STING agonists in multiple murine tumor models, including the immune checkpoint blockades-resistant tumors. In a benchmark study, CMP also performed significantly superior therapeutic efficacy than the leading STING agonists in clinical trials.

In the third project, I highlighted coordination interaction as a new mechanism for CDN formulation because the available formulation technologies relying on encapsulation and charge absorption are inefficient and/or unstable. I screened different metal ions and found interesting crystal structures formed between zinc ion (Zn^{2+}) and cyclic di-adenosine monophosphate (CDA). To design an efficient nanoparticle formulation, I also introduced Mn and $(histidine)_{33}$-polyethylene glycol (H33-PEG) in the coordination system given the potentiation effect of Mn on STING activation and the ionizable property of H33-PEG for endosome escape. By simple one-pot synthesis, I got homogeneous nanoparticles, CDA-Zn/Mn@H33-PEG (CZMP). In animal studies, CZMP could not only induce higher immune activation for cancer immunotherapy but also

function as an effective vaccine adjuvant for COVID-19 vaccine. Overall, coordination-based formulation CZMP represents a versatile platform for STING agonist delivery for disease treatment and prevention.

Chapter 1. Introduction

Metal elements have been conceived as medicines by alchemy for disease cure millennia ago and have been recorded for disease treatment hundreds of years ago[1-3]. However, until the discovery of the antiproliferative activity of platinum complex by Rosenberg et al. in the 1960s, metal-based drugs did not arouse extensive interest in modern medicine[4-5]. Nowadays, the platinum-based drug has become widely used as indispensable chemotherapy for many types of cancers. Nevertheless, like other cytotoxic chemo drugs, platinum drugs have unsolvable toxicity, severe adverse effects on healthy tissues, and risk of drug resistance by malignant cells. Another fact of metal drugs is that very few other metal drugs except platinum drugs have been proven successful in the clinic up to now even though the potential of the metal drugs has been widely recognized and emphasized[2]. So, instead of focusing on the cytotoxic activities, it is time to rethink the design principle and mechanism for developing a new generation of metal drugs.

Interestingly, various metal ions have been found to play important functions in the regulation of many important immune processes[6-7]. For example, Potassium (K+) was found to be able to preserve T cell stemness and metabolic reprogramming of T cells with a high concentration of K+ could increase the in-vivo persistence and multi-potency[8-9]. Calcium (Ca2+), increased within the cell after T-cell receptor (TCR)-antigen engagement, was found to facilitate the TCR-CD3 complexes phosphorylation and act

as a second messenger for dephosphorylation of nuclear factor of activated T-cells (NF-AT) via the calmodulin-calcineurin pathway[10-11]. K+, Na+, and Ca2+ were found to play an important role in the regulation of NLRP3 inflammasome activation[12-14]. Zn2+ was found critical for cGAS recognition of cytosol DNA in infection and inflammation while Mn2+ was found essential for host defense against DNA virus infection by increasing sensitivity of cGAS and STING[15]. These findings on the involvement of metal ions in immune processes with clearly revealed mechanisms have greatly extended the boundary of our knowledge of metal ions. And this has generated a newly defined field, “metalloimmunology”. These metalloimmunological studies have also provided new principles and perspectives for the next generation of metal drug discovery and development.

Cancer immunotherapy has revolutionized the therapy of various cancers and fundamentally changed our understanding of disease treatments. Given the important roles of metal ions in the regulation of immune processes, targeted modulation of the metal ions in the related immune process is possible to realize therapeutic immune modulations, opening chances for disease immunotherapy. We define such therapy as “metalloimmunotherapy”: therapeutical manipulation of the immune processes by metal ions for disease treatments. This is not a new-born field as some pioneer works have used metal ions to modulate the immune process for disease treatment or prevention, such as Alum salts as vaccine adjuvants in clinic and Mg^{2+} for anti-EBV treatment. However, few people realize that this could generate a whole class of new immunotherapy and no guideline for people to develop metalloimmunotherapy. Here we try to picture this on-forming frontier of immunotherapy by reviewing the previous

scattered reports and the latest exciting advancements in the field. We will classify metalloimmunotherapy into five categories and will discuss each category in detail with principles and examples. Also, we would share some perspectives of the future development of metalloimmunotherapy and discuss new technologies that be used to advance the development. In this way, we hope we could arouse more recognition of metalloimmunotherapy for various disease treatments and catalyze the fundamental and translational studies of metalloimmunotherapy. This will be a paradigm shift of metallodrugs development.

1.1. Metal ion in immunity

Metal ions play important roles in immune-related pathways and thus affect the associated immune responses. The mechanisms of their mediations with the immune systems have been gradually unraveled, which greatly improves current understanding of metal ions' immunological roles at molecular levels. Specifically, we categorized "Metalloimmunology" into three aspects (**Fig. 1-1**): metal ions' role in innate immunity, metal ions' role in adaptive immunity, and metal ions' role in host-microbe interface, where the functions of metal ions are achieved through their catalytic, structural, or regulatory interactions with various immune "sensors", ion transporters, enzymes, and downstream effector proteins. Proposed interactions of metal ions mediated in immunity are summarized below.

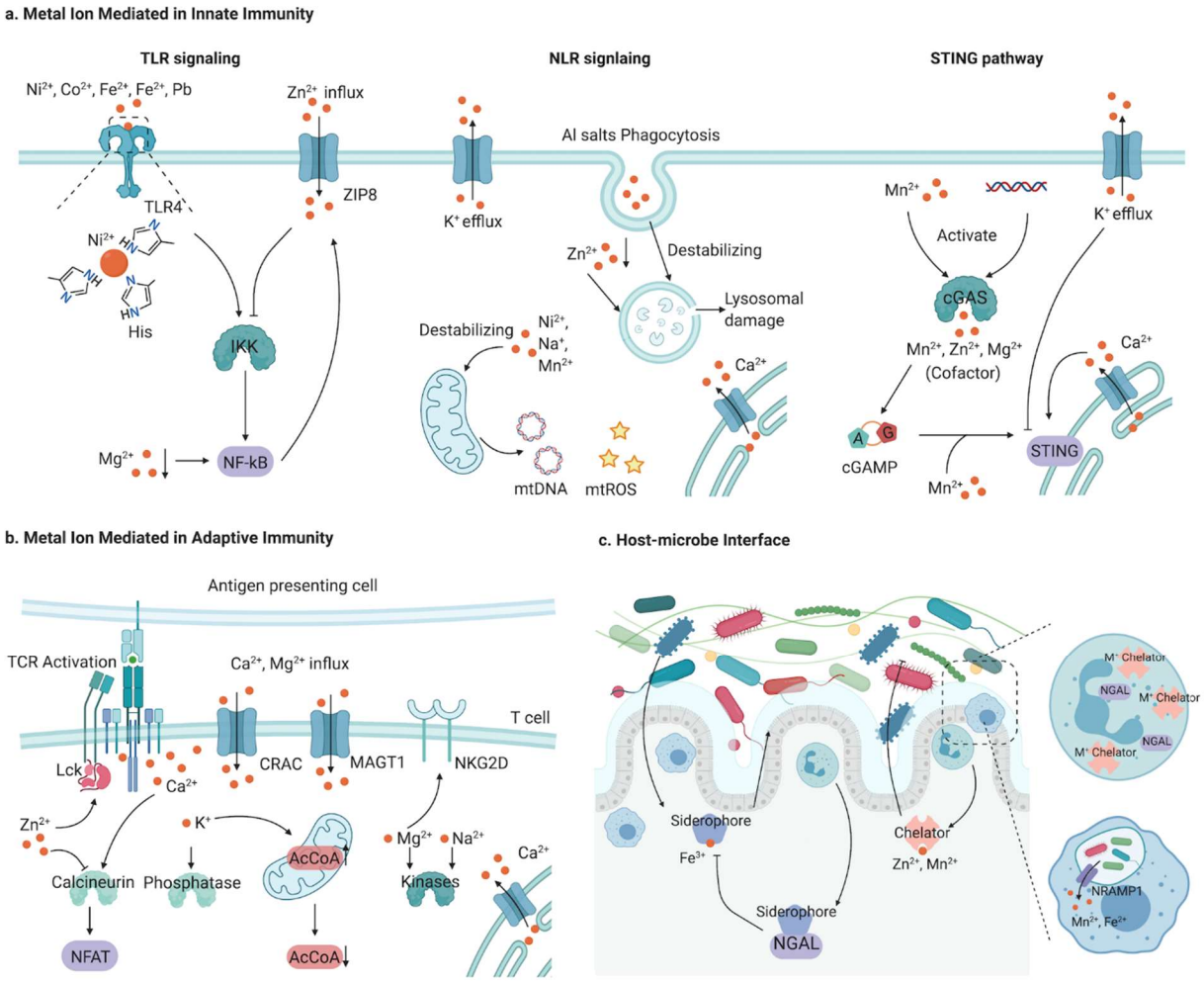

Figure 1-1. Metal ions-mediated immune processes. a) Metal ions' role in innate immunity. Some metal ions, such as Ni^{2+}, Co^{2+}, Fe^{2+}, Fe^{3+}, Pb, Zn^{2+}, Mg^{2+}, could affect TLR signaling pathway; Some metal ions, such as K^{+}, Zn^{2+}, Al, Ni^{2+}, Na^{+}, Mn^{2+} and Ca^{2+}, could modulate NLR signaling; Some metal ions, such as Mn^{2+}, Zn^{2+}, Mg^{2+}, K^{+} and Ca^{2+}, could regulate cGAS-STING activation and signaling. b) Metal ions' role in adaptive immunity. Some metal ions, such as Ca^{2+}, Mg^{2+}, Zn^{2+}, K^{+} and Na^{+}, could affect T cell functioning to modulate adaptive immune response. c) Metal ions' role in host-microbe interface. Host immune system could control level of metal ions, Zn^{2+}, Mn^{2+} and $Fe^{2/3+}$, in host-microbe interface to regulate the composition of microbiota or control the growth of invading pathogens.

1.1.2 Innate immunity

Innate immune response is the first line of host defense to the presence of invading pathogens. The detection of microbes significantly relies on pattern recognition

receptors (PRRs) to sense pathogen-associated molecular pattern (PAMP), such as lipopolysaccharide (LPS), flagellin, RNA and CpG DNA[16-17]. Interestingly, certain metal ions could also activate these PRRs, like Toll-like receptors (TLRs) and nucleotide-binding oligomerization domain (NOD)-like receptors (NLRs). Ni^{2+} could directly activate human TLR4 to trigger an inflammatory response comparable to the traditional TLR4 ligand LPS. Three non-conserved histidine residues within the leucine-rich repeats (LPR) of TLR4 could be potentially responsible for Ni^{2+} binding. Two histidine mutations would significantly abolish the Ni^{2+}-induced activation while LPS is still capable of inducing the cytokine production, indicating the distinct TLR binding and activation mechanisms between LPS and Ni^{2+}[18]. Other metal ions or metals also demonstrated the TLR-dependent activation, such as Co^{2+}[19] and Pb[20]. Fe^{2+} or Fe^{3+} associated heme molecules could directly activate TLR4 with a mechanism different from the LPS activation. Both porphyrin ring and iron ion coordination are indispensable for TLR activation[21]. The innate immune functions commonly lead to the activation of transcriptional factors nuclear factor-kB (NF-kB) and mitogen-activated protein kinase (MAPK) signaling pathways to stimulate cytokines production. A variety of metal ions have indicated their proinflammatory activating functions showing the stimulation of the NF-kB and the MAP kinase[22]. For instance, Fe^{2+} but not Fe^{3+} could function as an agonist to directly activate NF-kB pathway and induce the TNF-a production.[23] Low extracellular levels of Mg^{2+} could upregulate the expression of NF-kB.[24] As a regulatory pathway, NF-kB could also regulate the expression of zinc transporter protein (ZIP8) and allow the Zn^{2+} intake.[25] The influx of Zn^{2+} in turn downregulates the IKK activity by

binding to a specific site in the kinase domain, which in turn negatively modulates NF-kB pathway.

The recognition by NLRs is required for the activation of caspase-1 via the assembly of a multiprotein complex called 'inflammasome'.[26] This would subsequently lead to the production of various pro-inflammatory cytokines, such as interleukin-1b (IL-1b) and IL-18.[27] Several identified inflammasomes are defined by the NLR proteins they contained, such as NLPR1, NLPR3, and IPAF. NLRs can not only recognize the microbial stimuli but also endogenous markers of cellular damage (such as adenosine triphosphate (ATP) and uric acid crystals). The activation of NLRP3 inflammasome by the crystalline form of uric acid further triggered the hypothesis of other immunostimulatory crystals could be similarly recognized by NLRP3 inflammasome.[28] It was demonstrated that the production of IL-1b and IL-18 in macrophages can be induced by aluminum (Al) particles and deficiency in each component of NLRP3 inflammasomes (NLRP3, adaptor protein ASC, or caspase-1) failed to trigger their production.[29] Mechanistically, Al salts could undergo phagocytosis and result in the damage of lysosomes, which could induce the NLRP3 inflammasome activation.[30] Similarly, it is reported that sustained Zn^{2+} depletion may cause the destabilization of lysosomes and stimulate the NLRP3 inflammasome and IL-1b secretion.[30-31] Mitochondrial damages have also been linked to the inflammasome activation[32] and a variety of metal ions could mediate in this process. Mn^{2+} can act as an amplifier in NLRP3 inflammasome signaling by causing mitochondrial defects in microglial cells, which further increased the release of ASC containing exosomes and transfer the inflammasome activation through these exosomes from cells to cells.[33] Ni^{2+} induced

mitochondrial ROS (mtROS) accumulation and the release of mitochondrial DNA (mtDNA);[34] hyperosmotic stress from high levels of NaCl could induce mtROS accumulation as well;[35] both contribute to the activation of inflammasome. Apart from metal ions in mediating lysosomal and mitochondrial defects in inflammasome activation, Ca^{2+} influx and K^{+} efflux are two other common signals for NLPR3 inflammasome activation.[36-37] Ca^{2+} could promote the assembling of NLPR3 inflammasome components and the process was mediated by a G-protein-coupled receptor (GPCR) called calcium-sensing receptor (CASR).[36] The stimulated CASR could elicit an increased cytoplasmic Ca^{2+} signal via activating phospholipase C (PLC) and a reduction in cAMP levels by inhibiting adenylate cyclase. Both signals contributed to the enhanced NLPR3 inflammasome formation. In addition, Gadolinium ions (Gd^{3+}) could function as a CASR agonist to indirectly activate the NLRP3 inflammasome.[36] In terms of K^{+}, a low intracellular level of K^{+} could contribute to the activation of NALP3 inflammasome but not of the IPAF inflammasome.[37] Higher concentration of K^{+} prevented the NALP3 inflammasome assembly and hindered caspase-1 recruitment.[38]

The cytosolic surveillance mechanism of DNA could induce the production of Type-I interferon (IFN) through the STING (stimulator of IFN genes) activation.[39] STING activation relies on cyclic guanosine monophosphate-adenosine monophosphate (cGAMP) synthase (cGAS) pathway. cGAS could trigger the synthesis of cGAMP from ATP and GTP after sensing cytosolic DNA. cGAMP further induces the type I interferon response by STING adaptor, where STING could recruit the cytosolic kinases IKK and TBK1 to activate the downstream transcriptional factors NF-kB and IRF3.[40-41] cGAS belongs to the nucleotidyl transferase (NTase) superfamily, which is commonly divalent

cations dependent. This indicates certain divalent metal ions could play important roles in cGAS mediated innate immune pathways. Mg^{2+}, as an abundant ion source in cytosol, could serve as the catalytic cofactor of cGAS to catalyze the formation of cGAMP.[42] Mg^{2+} can be replaced by Mn^{2+} and elicited even higher catalytic activity. Mn^{2+} demonstrated capability of directly activating cGAS to generate secondary messenger cGAMP independent of dsDNA or low concentrations of dsDNA. Mn^{2+} can also augment STING activity by enhancing the cGAMP-STING binding affinity.[43] Different from Mg^{2+} in cytosol, physiologically, Mn^{2+} is released from the mitochondria and the Golgi apparatus upon the infections by DNA-virus. This supports that Mn^{2+} could be a more efficient cGAS activator than Mg^{2+}.[44] Other metal ions, such as Zn^{2+}, could stabilize the cGAS-DNA complex by binding to the cGAS so as to increase the cGAMP generation.[45] Apart from certain structural roles metal ions play in mediating the STING pathway, some metal ions are indirectly involved in enhancing or restraining the STING activation. The intracellular ER stress that incorporates Ca^{2+} mobilization could support the STING activation.[46] To reduce the sustained STING activation, K^{+} efflux could restrain cGAS-induced type I IFNs responses driven by producing the pore-forming protein Gasdermin D.[47]

1.1.2 Adaptive immunity

One of the key aspects of adaptive immunity development for generating long-lived and antigen-specific immune responses relies on activation of T cell receptor-CD3 complex (TCR) through the recognition of antigens presented by major histocompatibility complex (MHC).[48] Metal ions have indicated critical roles either as structural supports for complex formation induced by TCR signaling or as regulatory

factors for kinases/phosphatases or transcriptional proteins so as to affect the associated effector programs of T cell activation. The TCR stimulation is followed by the recruitment of leukocyte-specific protein tyrosine kinase (Lck) for phosphorylation and various other kinases.[49] Consequently, the phosphorylated scaffolds further activate inducible T cell kinase (ITK) and PLCγ to triggers Ca^{2+} release from intracellular stores and Ca^{2+}-release-activated Ca^{2+} channel (CRAC).[49-50] Ca^{2+} influx represents a comprehensive signaling network in the TCR activation pathway. From one aspect, Ca^{2+} influx led to a higher local Ca^{2+} concentration in proximity to TCR than the cytosolic compartment, which neutralizes the negative charge of the phospholipids, promote dissociation of cytoplasmic domain of CD3, and expose the tyrosine groups for phosphorylation.[51] Therefore, the Ca^{2+} mediation could sustain and amplify the T cell activation. From another aspect, Ca^{2+} could bind with calmodulin and subsequently activates phosphatase calcineurin to dephosphorylate transcriptional factors nuclear factor of activated T cells (NFAT). Dephosphorylated NFAT can then translocate into nucleus and induce the NFAT-dependent gene expression.[52] Defects in store-operated calcium entry (SOCE) also caused the inability to activate NFAT and thus was associated with impaired immune responses.[53] Apart from indispensable Ca^{2+} functions, other metal ions have displayed significant roles in this signaling network. For instance, TCR stimulation also induced a robust Mg^{2+} influx through magnesium transporter 1 (MAGT1), which is critical for subsequent PLCg activation and Ca^{2+} signaling.[54] In addition, Mg^{2+} deficiency due to the MAGT1 defects could lead to the abnormal expression of natural killer activating receptor (NKG2D) in cytotoxic $CD8^+$ cells and NK cells, which undermined the cytolytic responses of cytotoxic T cells and impair the

defending response towards virus infections by NK cells.[55] Decreased Mg^{2+} levels also negatively affected TCR signaling by inhibiting ITK since its unique binding ability to the catalytic pocket of ITK. Other alternative divalent ions, such as Ca^{2+} and Mn^{2+}, did not exhibit similar effects on ITK.[56] Zn^{2+} displayed double-sided roles in mediating adaptive immunity, where it has inhibitory effects on the activity of phosphatase calcineurin, which hindered nucleus translocation of NFAT[57] while displaying stimulatory effect in promoting the complex formation between cytoplasmic tails of CD4/CD8a and Lck so as to induce efficient antigen-specific T cell activation via TCR complexes.[58] Other mechanisms for metal ions mediations in adaptive immunity have also been reported. For instance, the increase in K^+ level serves as an ionic checkpoint to suppress T cell effector function by impairing TCR-dependent Akt-mTOR phosphorylation. Mechanistically, K^+-mediated Akt-mTOR phosphorylation impairment relies on the enhanced serine/threonine phosphatase PP2A activity; and inhibition of PP2A activity could rescue the hypophosphorylation of Akt and reduced effector functions caused by the elevated K^+ level.[59] It was later reported that K^+ elevation also hindered the nutrients uptake of T cells leading to a metabolic reprogramming towards autophagy and mitochondria-dominant cellular metabolism. This reduced the availability of nucleocytosolic acetyl–coenzyme A (AcCoA) and thus limited the histone acetylation on genes that are responsible for effector functions and exhaustion, which leads to T cells' effector program dysfunction while preserving their stemness.[60] Serum/glucocorticoid-regulated kinase 1 (SGK1) was identified to be another salt-sensible regulator for multiple ion channels regulations, including Na^+.[61] Increasing Na^+ concentrations could induce overexpression of SGK1 and lead to the deactivation of FOXO1. This mediated

the induction of pathogenic TH17 cells by promoting IL-23R expression;[61] and later showed to impair the suppressive function of Foxp3$^+$ regulatory T cells (Treg) by altering the stability of Foxp3 and promoting IFNg secretion.[62]

1.1.3 Host-microbe interface

The microbial cells colonizing the human body represented at least comparable abundance with the host cells,[63] among which microbial communities residing in gut are largest and their roles in human health and diseases are gradually uncovering.[64 65] The gut microbiota play crucial functions in mediating and training the host immunity, where they achieve the symbiotic relationship with the host to maintain the homeostasis.[66 67] Collective communities of these bacteria provide a unique and powerful enzymatic capability to regulate host physiology. The crosstalk mechanisms between the immune system and microbiota identified are commonly through various metabolites.[68 69 70] Metal ions, including Fe^{2+}, Zn^{2+}, Mn^{2+}, are frequently required by bacteria in their metalloenzymes and provide structural support or promote catalytic tasks.[71] It is therefore speculated that metal ions could be secondary messengers at the interface of host-gut microbiota as measures to regulate the composition of microbiota or control the growth of invading pathogens. Several mechanisms have been identified in utilizing metal ions as mediative strategies between the host and microbiota. Levels of metal ions are carefully regulated intracellularly to both fulfill their essential functions as well as limit toxicity. The host develops mechanisms in either restricting their availability against unwanted pathogenic bacteria or directing the toxicity of these metal ions to defend against microbial invaders.[71] For instance, to reduce the access of intracellular bacteria to access these metal ions, natural resistance-associated macrophage protein

1 (NRAMP1) could move to the phagosomal membrane and pump Fe^{2+} and Mn^{2+} out of the phagosomal compartments.[72] On the contrary, bacteria are also capable of circumventing the host immunity-mediated metal ions withholding. They could either evolve to find the alternative metal ions to support their living, in the case of B. burgdorferi substituting Fe^{2+} by Mn^{2+},[73] or they can compete for the metal ions through other manners. One of the strategies used by bacteria is secreting small molecule siderophores as Fe chelators and siderophores-Fe^{3+} complexes could be subsequently transported within the bacteria.[74] As a countermeasure in innate immune response, the activation of TLRs induces the generation of neutrophil gelatinase-associated lipocalin (NGAL) to bind and sequester certain siderophores.[75] In addition, bacteria have surface receptors for haem or haemoproteins which are capable of transmitting Fe^{2+} into cytoplasm.[76] Other metal ions, including Mn^{2+} and Zn^{2+}, also play indispensable functions at the host-microbe interfaces and are regulated via similar mechanisms.[77] For instance, calprotectin, which takes up nearly half of the protein compositions of the neutrophil cytoplasm, is a strong chelator of Mn^{2+} and Zn^{2+} in restricting their access to bacteria.[78] Abnormal levels of metal ions could also cause toxicity so as to kill the bacteria, where macrophage could release Zn^{2+} into phagosome and survival of bacteria within the phagosome relies on the expressions of Zn^{2+} efflux system.[79] Established crosstalk mechanisms among metal ions, microbiota, and the host immune system are majorly the defending strategies of the host towards invading pathogens.

1.2. Metalloimmunotherapy

Given the important function of metal ions in immune processes as discussed above, targeted modulation of the metal ions in these processes is possible to realize

therapeutic manipulation of immune responses and opens up chance for metalloimmunotherapy of diseases. In this part, we will categorize metalloimmunotherapy into five major classes: 1) therapeutic metal supplement for immune modulation; 2) metal ion-mediated immune cell re-programming for cell therapy; 3) metal-based vaccine adjuvants; 4) synergistic metal ion-drug combination for immunotherapy; 5) metallodrug-induced immunogenic cell death for cancer immunotherapy. For each type of metalloimmunotherapy, we will discuss the principles, the latest progress, and future directions. The purpose is to inspire related scientists and provide a route map for metalloimmunotherapy development.

1.2.1. Metal-based vaccine adjuvant

Insoluble metal salts have been proven effective antigen adjuvants to increase efficacy of vaccines, which is mediated by providing effective innate immune stimulation and prolonging antigen availability to B cells and antigen-presenting cells (APCs). For example, Aluminium salts-based adjuvants, like alum hydroxide and alum phosphate, are the most extensively used vaccine adjuvants globally. Their adjuvant application could be dated back to the 1920s. The mechanism has long been thought attributed to the “depot effect” and cell death-associated innate immune stimulation[80]. In 2008, Stephanie C. Eisenbarth et al.[81] found that alum-induced immune stimulation was mediated by activating NLRP3 inflammasome and thus induce production of pro-inflammatory cytokines, such as interleukin-1β and interleukin-18. Nalp3, ASC or caspase-1-deficiency could compromise the antibody response of alum-adjuvanted vaccine while the same effect was not observed in vaccine with Freund’s adjuvant. In addition, other metal salts could also be used as vaccine adjuvants. For example, CaP

is a WHO-approved human vaccine adjuvant and has been used as a vaccine adjuvant for diphtheria–pertussis–tetanus vaccine and the smallpox-yellow fever-measles-BCG-tetanus pentavalent vaccine in France[82]. Iron oxide, Zn oxide and Mg phosphate nanoparticle have also been studied as vaccine adjuvants[83-84]. Compared to the organic vaccine adjuvants, these inorganic metal salt vaccine adjuvants usually present as particle forms. The insoluble particle character may have several advantages, such as facilitating antigen delivery and uptake by immune cells, presenting antigen in appropriate biophysical properties and controlling antigen release.

Recently, a colloid form of Mn salt was reported to be an effective adjuvant. Based on the cGAS-STING activation property of Mn2+, Rui Zhang et al. developed colloid manganese salt as adjuvant[85]. They have found Mn salt is a highly effective universal adjuvant to induce strong humoral immune responses and cellular immune responses. In the mechanism study, they found that the great adjuvant properties of Mn salt were attributed to both cGAS-STING pathway activation and NLRP3 inflammasome activation. In particular, the author systemically studied the performance of MnJ as an adjuvant for different kinds of antigens, such as inactivated viruses, recombinant proteins, and peptides. For all the antigens evaluated, MnJ demonstrated outstanding adjuvant activity and was superior to alum adjuvants. Especially, MnJ could induce effective Th1 response in addition to Th2 response. This simple yet effective adjuvant is

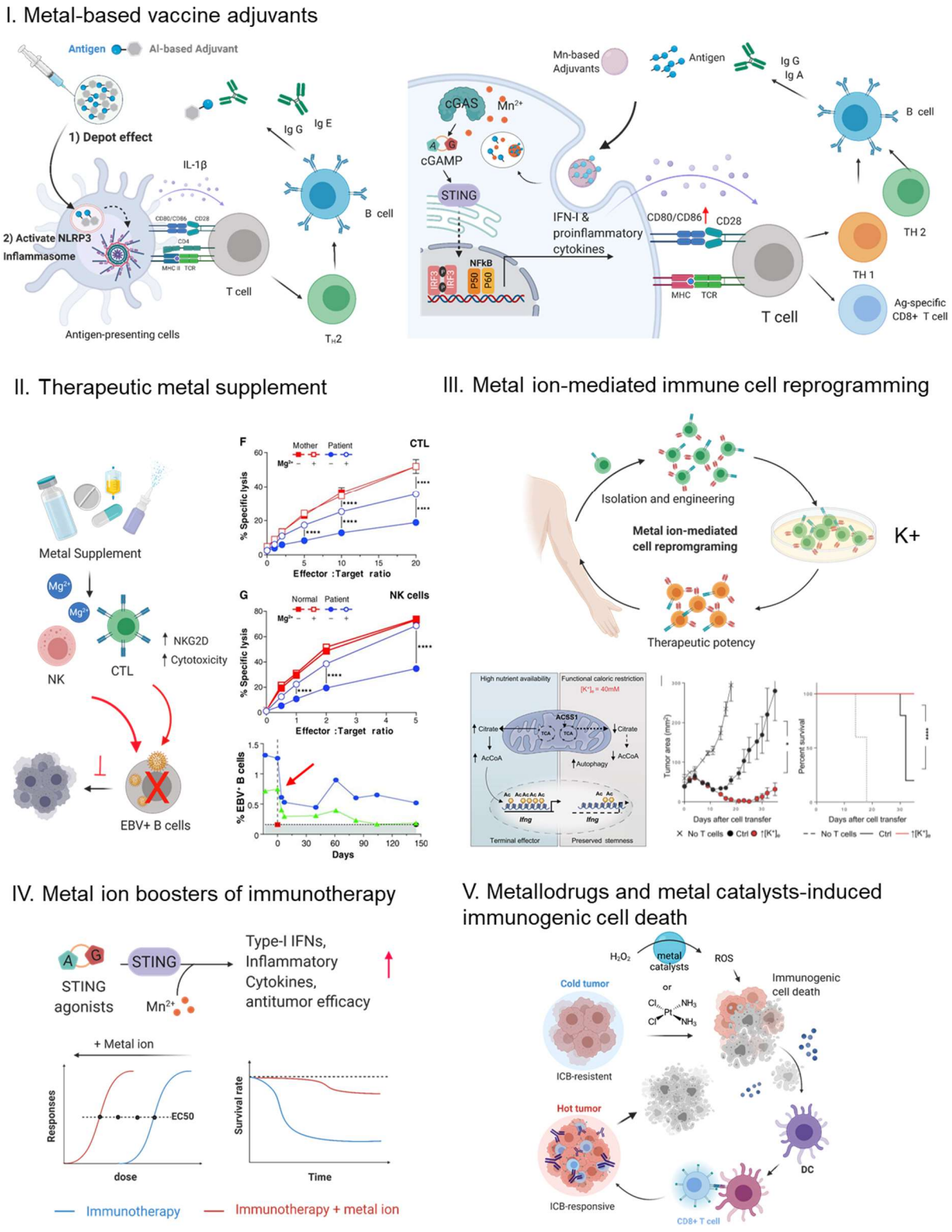

Figure 1-2. Metalloimmunotherapy. I) Metal-based vaccine adjuvants. Some metal ion-based materials, such as Al and Mn salts, can be effective antigen adjuvants to increase

efficacy of vaccines. II) Therapeutic metal supplement for immune modulation. Some metal ion supplements, such as Mg^{2+}, can treat diseases by triggering specific immunological modulation. Right panel is adapted from ref [87]. III) Metal ion-mediated immune cell re-programming for cellular therapy. Metal ions, such as K+, could reprogram immune cells ex vivo to play the desired immune functions after re-infusing back into the human body. Bottom panel is adapted from ref [8]. IV) Metal ions as boosters of immunotherapy for synergistic combination therapy. Some metal ions, such as Mn^{2+}, could amplify the drug responses and modulate their activity. V) Metallodrugs or metal catalysts-induced immunogenic cell death for cancer immunotherapy. Some metal drugs or metal-based catalysts are good immunogenic cell death (ICD) inducers.

a very exciting breakthrough in the field of vaccine adjuvants. Compared to other adjuvants under development that based on new molecular discovery, Mn salt is simple, cheap, easy-to-get and shares the physical properties of Al adjuvant. This also underscores that studying the immunology of various metal ions and formulating them into appropriate forms may provide new chances to develop new effective adjuvants and therapeutics.

1.2.2 Therapeutic metal supplement for immune modulation

Therapeutic metal ion supplements can treat diseases directly by triggering specific immunological modulation or metabolism change of the immune cell in the body. For example, Mg supplement has been used to treat EBV infections by enforcing the cytotoxicity of T-cells and NK cells against EBV[86-87]. People with Magnesium transporter 1 (MAGT1) gene deficiency was found related to X-linked immunodeficiency with Mg2+ defect, Epstein-Barr virus (EBV) infection, and neoplasia (XMEN) disease. These MAGT1-deficient patients have impaired T cell receptor (TCR)–stimulated Mg2+ influx and T cell activation, more likely suffering from severe chronic virus infections and lymphopenia. At the same time, MAGT1-deficient patients would have a lower intracellular concentration of free Mg2+ than normal, which would reduce the

expression of NKG20 in NK cells and CD8+ T-cells and further attenuate their cytotoxicity. Based on this, when these patients were treated with Mg2+ supplement, the intracellular level of free Mg2+ was restored and NKG2D expression was increased dose-dependently, which further leads to the recovery of NK cell and CD8+ T-lymphocyte cytotoxicity and a decrease of EBV-infected cells in patients. In addition, Zn2+ has been widely used for cold remedies caused by viruses and tested in multiple clinical trials. Even though the results vary depending on the study conditions, Zn2+ may be effective to shorten disease duration when administered within 24 h after the onset of symptoms and may have a prophylactic effect in children[88]. The mechanism is unclear, which could be inhibiting virus replication, viral binding of ICAM-1, or enhance host immunity, such as cytokine production and T cell function. Besides application for cold remedies, Zn2+ supplements have also been tested in [89-90]. Even though inconsistent result was shown, Zn2+ may increase in the number of TH cells and reduced the frequency of opportunistic infections with Pneumocystis jiroveci (formerly P. carinii) and Candida. Recently, Mn2+ was found to be able to increase the sensitivity of cGAS-STING pathway to dsDNA. In mice model, intranasal administration of Mn2+ could prevent multiple viral infections, such as Vaccinia virus (VACV), Herpes simplex virus-1 (HSV-1), vesicular stomatitis virus (VSV)[15]. With more and more new discoveries about the relationship between metal ions and immune system, more targeted therapeutic metal ions supplements could be developed. So far, it largely remains unknown how metal ions are involved in immune responses mechanically at molecular level. For example, even though Zn2+ may have beneficial effects in cold treatment, but it lacks statistical confirmation of effectiveness and the plethora of possible

mechanisms, which illustrate the need for in-depth research, allowing develop higher efficient therapeutic metal supplements.

1.2.3. Metal ion-mediated immune cell reprogramming for cellular therapy

The immune effects of metal ions could be used to reprogram immune cells ex vivo to play the desired immune functions for disease treatment after re-infusing back into the human body. For example, the extracellular high concentration of potassium ion (K+) could trigger the reduced T cell's nutrition uptake[8]. T cells would undergo autophagy and mitochondrially dominant metabolism in response to the cell starvation. This leads to decreased nucleocytosolic AcCoA for histone modification and epigenetic remodeling: decreased expression of Ifng, Pdcd1, Cd244, Havcr2, Klrg1(restrict T cell terminal effector differentiation and exhaustion) and preserved expression of TCF7, CD62L, and CD27 (retain T cell stemness). These epigenetic changes enhance the stemness of T cells, such as enhanced self-renewal, differentiation potential and persistence. Particularly, K+ treatment ex vivo could reprogram T cells to remarkably improve the efficacy of adoptive T cell immunotherapy. As proof of concept, the author activated pmel T cell in presence of a high concentration of K+ ex vivo and adoptively transferred into mice with established B16 melanoma. The K+-treated T cells demonstrated significantly enhanced persistence in secondary lymphoid system and tumor microenvironment, and were maintained in more multipotent and less differentiated state. The mice with K+-reprogrammed T cell transfer could significantly better inhibit tumor growth and significantly prolong the survival than the conventional T cell transfer. And secondary transfer of the tumor-infiltrating lymphocytes (TILs) isolated from the mice received K+ reprogramed T cell transfer showed increase immune

memory response to tumor antigen. This is a remarkablely thorough study covering from mechanism study of K+ metalloimmunology to preclinical proof of K+-reprogrammed T cell therapy. Further study could focus on reprogramming other types of immune cells and exploring other types of metal ions for programming. For example, Mn2+, AL, Fe2+/3+, Ni2+ could be used for reprogramming of dendritic cell-based cell therapy given their activity on stimulating APCs. This kind of study provided a great way to strengthen the immune cells through reprogramming by metal ions to achieve the aim of immunotherapy.

Different from the traditional drug or therapy based on metal ions, the metal ion reprogrammed-cell therapies don't need to be injected directly into human body and could thus avoid the off-target side effect and toxicity. Besides, even though metal ions have extensive immune activities as discussed above, delivering metal ions to specific sites and specific cells with sufficient bioavailability in vivo is very challenging. As an alternative way, ex-vivo programming immune cell with a precise amount of metal ion could directly reprogram the target immune cells in a more adjustable and predictable way, which represent an example of precision metalloimmunotherapy. Furthermore, despite that cell therapies have proven to be promising for cancer treatment, their in-vivo performances are unsatisfactory and need to be improved. For example, CAR-T cell therapies are still inefficient for solid tumor treatment. Even though a lot of efforts have been dedicated to resolve this problem, such as genetically engineering CAR-T cells with "amors" to prevent their exhaustion in tumor microenvironment[91], these genetically engineering processes are usually technically complex, time-consuming and suffering from safety concerns. Instead, metal ions-mediated cell reprogramming could

serve as “metal amors” that could increase the persistence of CAR-T cell therapy in a very simple but effective way, as shown in the example of K+-mediated T cell stemness preservation and reprogramming. The “metal amors” of cell therapy is possible to be further expanded to other immune cell therapy, such as DC-based, NK-based and Macrophage-based cell therapy after further fundamental research, given that these cells are able to be activated with various metal ions.

1.2.4. Metal ion boosters of immunotherapy

Metal ions could amplify the drug responses and modulate their activity. This could be done in different ways: 1) metal ions could directly modulate the drug-target interaction or the drug response, 2) metal ions could act on some specific immune process and synergize with immunotherapy. For example, we have recently screened different nutritional metal ion’s effects on STING agonist activity and found Mn^{2+} and Co^{2+} could greatly potentiate STING agonist and increases the type-I IFN production. Wherein, Mn could potentiate cGAMP in different human STING haplotypes by 12-77 folds. Combination of STING agonist and Mn2+ could increase tumor antigen-specific T cell response and tumor inhibition effect in vivo. Mechanism study revealed that Mn^{2+} could augment downstream molecular events, STING-independent p65 phosphorylation, STING-independent TBK1 phosphorylation, and STING-dependent IRF3 phosphorylation. The highly activated p65 and IRF3 could form a transcriptional IFN-beta enhanceosome for further potentiation. Formulation of cyclic dinucleotide (CDN) STING agonist and Mn into a nanoparticle formulation, CDN-Mn particle (CMP), could remarkably increase the therapeutic efficacy of STING agonist after both intratumoral and intravenous injections. Complete tumor regression of established

tumor and anti-cancer immune memory effect were observed. Lastly, in a benchmark study, CMP also performed a superior therapeutic effect than the leading STING agonists in clinical trials. This work indicates “metalloimmunotherapy” could be highly efficient after appropriate pharmaceutical design and optimization. This work also provides a paradigm of developing “metalloimmunotherapy”, from bioactive metal ions screening, mechanism study, pharmaceutical formulation to in-vivo/invitro therapy efficacy validation. In addition to directly potentiating STING agonist activity, Mn2+ was also shown to synergize with immune checkpoint blockade therapy. For example, it is reported that intranasal administration of Mn2+ could synergize with anti-PD1 therapy in murine tumor model by promoting dendritic cell maturation, antigen presentation, and activation of T cell and NK cell[92]. In a phase I clinical trial, they test the combination of intranasal or inhaled Mn2+ and anti-PD-1 antibody. Type I IFN induction and promising preliminary therapeutic effect were demonstrated. Interestingly, partial response (PR) (3/5) and stable disease (SD) (2/5) were observed in five patients with advanced solid tumor who experienced previously failed anti-PD-1 antibody combination therapy with chemotherapy or radiotherapy. Also, the safety is manageable, and no toxicity associated with manganese overdose was observed. This is a very encouraging study for clinical translation of manganese-based metalloimmunotherapy. From the example above, we could see leveraging the metal ions to boost immunotherapy represent a simple but efficient strategy for translational metalloimmunotherapy development. Even though Mn combination with immunotherapy has been increasingly recognized, the combination of other immune-active metal ions and appropriate synergistic drugs has not been widely explored. As shown in Figure 3, we screened the synergistic effect of

various metal ions and different innate immune activators. Interestingly, a wide-spreading synergistic effect was observed. For example, Co3+ could increase poly (I:C) activity in dose-dependent form; synergy was also observed between CpG and Mn2+, MPLA and Fe3+, MPLA and Ni2+, poly(dA:dT) and K+, R848 and Fe3+, R848 and Ni2+, CpG and Fe3+, CpG and Ni2+. This indicates numerous new combinations and discoveries of metal boosters of immunotherapies are awaited to be uncovered.

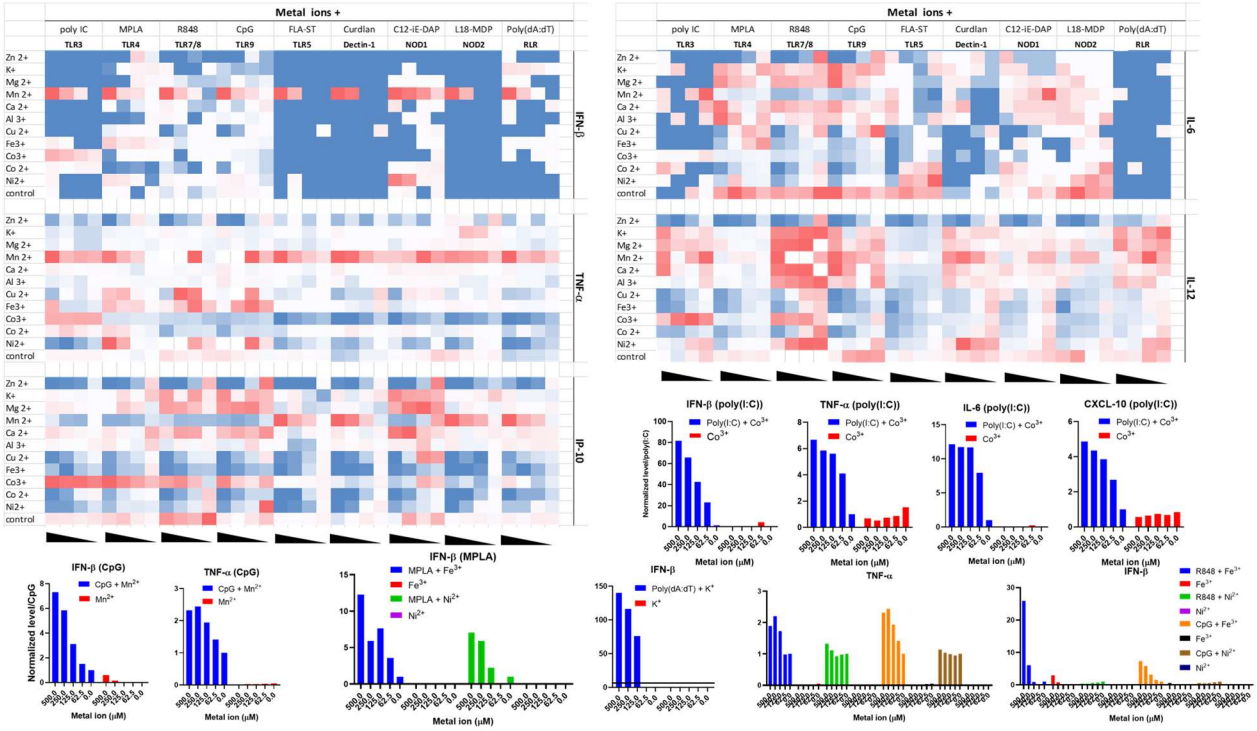

Figure 1-3. Synergy between different metal ions and innate immune activators. To screen synergy between metal ions and innate immune agonists, BMDCs were incubated with various concentrations of metal ions (0-500 μM) ± innate immune activators, and after 24 h, cytokines production were quantified by ELISA.

1.2.5. Metal drug-induced immunogenic cell death

Immunogenic cell death (ICD) is a type of cell death inducing immune activation by releasing damage-associated molecular patterns (DAMPs), such as High Mobility group B1 (HMGB1), heat-shock proteins (HSP70/HSP90), calreticulin (CRT), and

adenosine triphosphate (ATP)[93]. These DAMP could further activate APCs in tumor microenvironment, such as DCs, and prime cancer antigen-specific T cell immune response for cancer immunotherapy[94]. Some metal drugs are found to be good immunogenic cell death (ICD) inducers[94]. For example, Oxaliplatin is a typical ICD inducer, which causes DNA damage and induces collateral ER stress. Various research demonstrated that oxaliplatin could induce the entire panel of ICD hallmarks including release of different types of DAMPs and vaccinate immunocompetent mice using dead tumor cells treated with oxaliplatin. While other Pt-based drugs, such as cisplatin, have weak vaccination potential. It might be explained by that although they could release similar levels of ATP and HMGB1 compared with Oxaliplatin, they leak sufficient evidence to prove the CRT exposure and subsequently sufficient ER stress induction, especially in the murine model. Except for Pt-based metallodrug, several other metal complexes targeting ER were reported to induce type II ICD, such as Iridium (Ir) complex, ruthenium complex, copper complex etc. An Ir (III) complex is designed to induce ICD in Non-Small-Cell Lung Cancer in vitro and the Ir-treated LLC vaccine could provoke adaptive immune responses in vivo[95]. It is found that the clinically investigated ruthenium drug KP1339 could induce ICD in colorectal spheroid models in vitro[96]. An Endoplasmic Reticulum-Targeting Copper (II) complex is reported to display immunogenic effects in breast CSCs by caspase-dependent apoptosis in vitro[97]. CSCs are strongly linked to cancer relapse and metastasis, and they could hardly eliminate by chemotherapy or radiotherapy because they divide slowly. Thus, developing drugs that kill CSCs could be revolutionize for cancer treatment.

As tumors are generally regarded as apoptosis-resistant, cancer treatment may also be benefited from some new forms of ICD, such as Ferroptosis, Necroptosis and Pyroptosis[98]. Ferroptosis is characterized as an iron-dependent cell death associated with iron accumulation, lipid peroxidation and membrane damage. For example, a p53 plasmid-encapsulated Metal–Organic Network (MON-p53) has been shown to induce Ferroptosis via Fenton reaction of Fe (III)-based MON to produce ROS and p53 expression to enhance oxidase stress[99]. A glucose oxidase and doxorubicin loaded biomimetic metal-organic frameworks have been reported to trigger antitumor immunity based on ROS-ferroptosis-glycolysis regulation[100]. Transferrin modified MgO2 nanosheets could deliver ROS to kill tumor cells[101]. Necroptosis is characterized as activating the receptor-interacting protein kinase 1 (RIPK1)-RIPK3-mixed lineage kinase domain-like protein (MLKL) pathway. For example, a ruthenium (II) complex is reported to inhibit topoisomerase I and II, leading to DNA damage and resulting in necroptosis[102]. It also showed antitumor activity in vivo and has great potential for circumventing anticancer drug resistance in clinic. Pyroptosis is characterized as the formation of plasma membrane pores by members of the gasdernim protein family, such as gasdermin D (GSDMD) and gasdermin E (GSDME)[103]. It has been demonstrated that combining iron with carbonyl cyanide m-chlorophenyl hydrazone (a ROS-inducing drug) can activate ROS and induce pyroptosis via a Tom20-Bax-caspase-GSDME pathway in melanoma cells, which showed a promising antitumor effect in vivo[104].

Based on the cytotoxicity properties or/and the catalytic properties, metallodrugs in different forms are ideal for design of ICD-inducing agents[105]. With the development of material science, nanotechnology and catalytic science, we believe many metal-

based ICD inducers would emerge to be new effective cancer immunotherapy, especially after combination with immune checkpoint blockades and other cancer immunotherapy.

1.3. COVID-19 and metalloimmunotherapy for COVID-19 vaccine development

As discussed in Chapter 1.2.1, metal-based vaccine adjuvants have unique immunological and physiochemical character for better immune stimulation and immunization. COVID-19 has emerged into severe worldwide pandemic since end of 2019 and has aroused tremendous attention for developing effective vaccine to prevent the spreading. Metalloimmunotherapy, especially nanotechnology-based metalloimmunotherapy, is potent to aid in developing better COVID-19 vaccine by acting as effective vaccine adjuvants or acting as effective vaccine delivery system to facilitate antigen delivery to lymph nodes, increase uptake by immune cells, present antigen in appropriate biophysical properties and control the antigen release.

1.3.1. CVOID-19 and the vaccine development

A novel coronavirus, termed severe acute respiratory syndrome coronavirus 2 (SARS-CoV-2), emerged in December 2019. SARS-CoV-2 has spread globally, leading the World Health Organization to declare coronavirus disease 2019 (COVID-19) as a pandemic in March 2020[106]. As of October 2020, SARS-CoV-2 has caused more than 35 million cases and 1 million deaths around the globe. The United States alone has reported more than 7.5 million cases and suffered >210,000 lives lost since the first reported case in March 2020.

There are worldwide efforts to develop therapies and prophylactic vaccines against SARS-CoV-2. Therapeutics aim to shorten the hospitalization period and increase survival of infected patients, while prophylactic vaccines aim to generate protective immunity against SARS-CoV-2. Given the urgent pandemic setting with its associated consequences, such as limited ventilators and hospital capacity, it is critical to develop successful prophylactic vaccines against SARS-CoV-2. SARS-CoV-2 is a single stranded RNA virus that has a structure of betacorona viruses composed of spike (S) protein, envelope protein, membrane protein, nucleocapsid protein, and accessory proteins. SARS-CoV-2 shares high sequence similarity with SARS-CoV and takes a similar entry route to infect human cells [107]. That is, the receptor binding domain (RBD) of S1 subunit of S protein interacts with human angiotensin-converting enzyme 2 (ACE2), followed by membrane fusion mediated by S2 subunit [108]. Thus, S protein is a critical component of SARS-CoV-2 for cellular infection. In addition, functional neutralizing antibodies (NAbs) generated in COVID-19 patients were found to mostly target epitopes within S protein, suggesting S protein as a promising target for vaccination against SARS-CoV-2.

The process of developing a vaccine consists of two key steps: 1) identifying an antigen and 2) developing a delivery approach for said antigen to achieve robust cellular and humoral immunity. In the case of SARS-CoV-2, previous experiences with SARS-CoV and MERS-CoV have enabled rapid development of vaccine candidates. As of October 2020, more than 170 vaccines against SARS-CoV-2 are under development as tracked by the World Health Organization, and of those, 11 are undergoing Phase III

human clinical trials. These vaccine candidates can be categorized into four vaccine platforms: viral vector-, RNA-, DNA-, and protein-based vaccines [109] (**Fig. 1-4**).

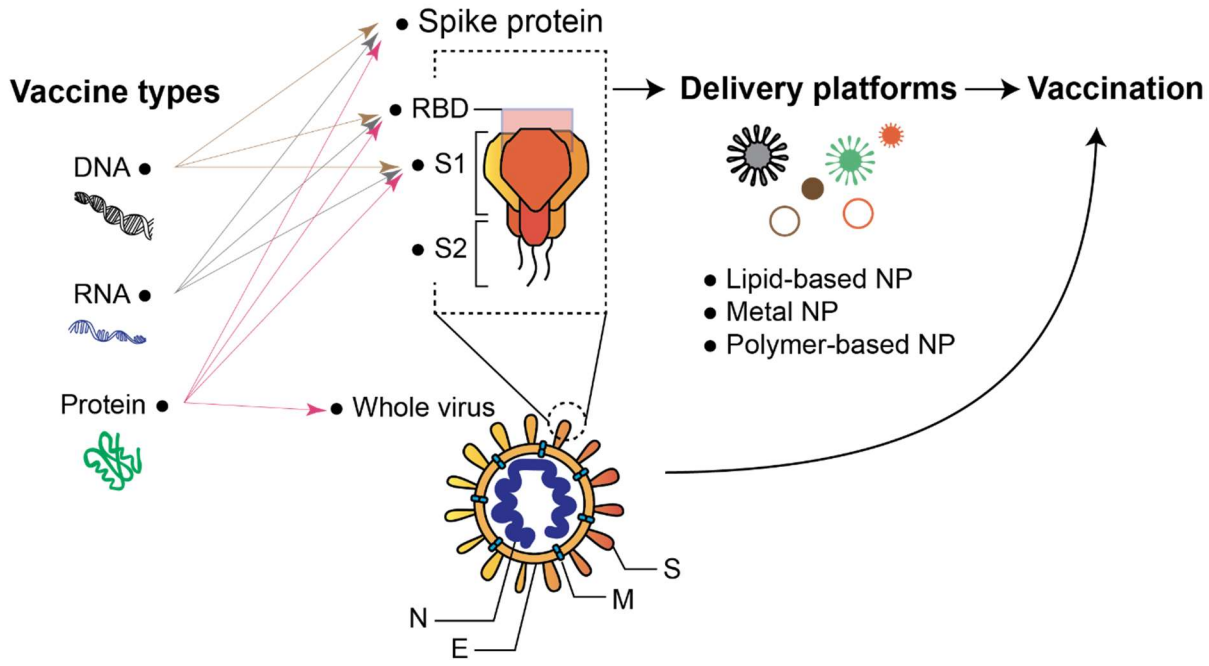

Figure 1-4. Various vaccine platforms for vaccination against SARS-CoV-2. [110]

Several non-viral vaccine platforms, enabled by advances in nanomedicine and vaccine delivery technologies, are approved or in different stages of clinical trials. They include mRNA and DNA encoding protein antigens of SARS-CoV-2 as well as protein antigen-based vaccines. The membrane-bound glycoproteins on corona viruses, called spike proteins that are responsible for viral entry into host cells, are great targets when developing a vaccine [111-112]. mRNA-, DNA- and protein-based vaccines often make use of this protein using different strategies. mRNA and DNA vaccines focus on the ways to deliver genetic materials encoding the antigen into the host cells, which often involve the use of delivery vehicles or electroporation devices. On the other hand, protein-based vaccines require the antigen proteins synthesized prior to administration, using

mammalian cells. Since these proteins are not in their native forms but are synthesized and secreted into culture medium in soluble forms, it is often challenging to maintain their stability. Therefore, recombination techniques are often involved when designing genetic vectors to endow stability to the antigen proteins before the vectors are transfected to the mammalian cells. Since the antigens used by mRNA-, DNA- and protein-based vaccines are usually a subset of an entire virus, they elicit relatively weaker immune responses, thus often require coadministration with adjuvants. Adjuvants are immunological agents that are added to vaccines to enhance the immune response. They are usually in the forms of ligands that interact with pattern recognition receptors on antigen presenting cells (APCs). Once engaged, downstream signaling within the APCs triggers various immune pathways that lead to stronger immune activation. There are many adjuvants that are used in the clinics and many more under development, which is one of the active areas of research in COVID-19 vaccine development.

1.3.2. Protein vaccines and adjuvants

Compared with DNA and RNA-based vaccines, protein vaccines require adjuvants to achieve strong immune responses. Novavax is one of the leading vaccine companies in a race against SARS-CoV-2. Novavax's vaccine employs a full-length S protein (NVX-CoV2373) genetically modified for greater structural stability compared with the wild-type (WT) S protein. The S protein variant used in the study had a smaller hydrodynamic size of 27.2 nm as well as a more uniform size, mass, and shape distribution (polydispersity index of 0.25-0.29) compared to the WT size of 69.53 nm and PDI of 0.46, despite the two having the same molecular weight [113-114]. Additionally,

mutations generated in the genetic sequence are thought to be crucial for reliable production of a stable pre-fusion S protein structure and ability to withstand stress from pH and temperature post *in vivo* administration, all contributing to a more effective immune response. NVX- CoV2373 is formulated with Novavax's proprietary Matrix M, an adjuvant composed of lipid molecules and saponin [115]. Preclinical studies performed with NVX- CoV2373 in mice and baboons as well as a Clinical trial showed elevated anti-S protein IgG (anti-S IgG) titers with potent neutralizing activity [113, 116]. In addition to Novavax, Clover Biopharmaceuticals focuses on the trimeric structure of native S proteins on SARS-CoV-2 in combination with either AS03 or CpG 1018 plus Alum as adjuvants.

Adjuvants trigger pattern-recognition receptors (PRR) on adaptive immune cells, and depending on which type of PRR an adjuvant aims to activate, different routes of immune responses are elicited. Therefore, the use of a potent and well-matched adjuvant can greatly enhance the vaccine efficacy. Currently, many COVID-19 vaccine developers employ adjuvants in their vaccines, including AS03 (GSK's α-tocopherol and squalene in an oil-in-water emulsion), CpG 1018 (Dynavax's DNA-based TLR-9 agonist), and MF59 (Novartis's squalene in an oil-in-water emulsion), which have shown to greatly improve the vaccine efficacy in preclinical and clinical studies [117-119]. In addition, there are many adjuvants under development with a great potential to improve protein-based vaccines. A synthetic TLR-7/8 agonist, 3M-052, has been used as an adjuvant together with HIV-1 clade C 1086.C–derived gp140 envelope protein (Env) for vaccination against HIV-1 [120]. Once vaccinated to rhesus macaques, Env plus 3M-052 induced higher levels of antibody response and long-lived plasma cells in bone marrow,

compared with vaccination with conventional adjuvants, such as alum, R848 (a TLR-7/8 agonist), MPL, and GLA (a TLR-4 agonists). In fact, many studies are currently examining ways to deliver TLR7/8 agonists, based on their potential to boost immune responses from immunologically vulnerable populations, including children and elderly [121].

1.3.3. Nanotechnology for vaccines and adjuvants

While administering soluble proteins in combination with adjuvant(s) has shown efficacy *in vivo,* further improvements can be made through the use of nanotechnology. Nanotechnology can increase stability of soluble proteins, while achieving targeted delivery to LNs for improved immunogenicity. In a pandemic setting, improving targeted delivery can translate to reducing the amount of antigen in a dose, which is advantageous when trying to maximize vaccine distribution. Similar to soluble proteins, co-delivery with adjuvants further improves nanoparticle-based vaccine efficacy. For example, a multi-layered lipid-based nanoparticle system was used to co-deliver protein antigen and an adjuvant monophosphoryl lipid A (MPLA), a Toll-like receptor-4 agonist used in other FDA-approved vaccines [122]. Compared with the soluble formulation, the nanoparticle vaccine elicited significantly more potent humoral and cellular immune responses upon subcutaneous injection in preclinical studies. Along the same vein, calcium phosphate (CaP)-based nanoparticles were used to deliver CpG and a viral antigen derived from the influenza A virus hemagglutinin, which prevented viral infection in mice [123]. When the vaccine was administered via intraperitoneal or intranasal routes, the nanoparticles were efficiently taken up by DCs, subsequently leading to T cell-mediated immune responses. Another study used the CaP nanoparticles as a tumor

antigen/CpG carrier to treat colorectal cancer in a murine model [124]. The vaccine induced a type-I interferon mediated immune response that increased the frequency of model tumor antigen-specific CD8+ T cells and exerted greater tumor control, compared with the soluble formulation. These examples indicate the versatility of nanoparticle systems as vaccine delivery platforms and show their potential for vaccination against other emerging pathogens.

Lymph nodes (LNs) are critical target tissues for vaccine delivery. For cellular immune response, T cells are primed by DCs and activated in LNs. For humoral immune response, germinal centers in the LNs are crucial for antibody affinity maturation and isotype switching. Therefore, targeting LNs may greatly improve immune responses. To this end, vaccines could be delivered by nanoparticles of an appropriate size, surface properties, and charge for effective LN draining. For different sizes of PLGA-PEG, 30 nm PLGA-PEG was found to be more efficient for LN draining, retention, and APC uptake [125]. Interestingly, for liposomal vaccines, smaller than 150 nm in diameter could drain to LN and trigger immune responses [126], suggesting that the ideal size for LN targeted delivery depends on the vaccine platforms employed. Elicio Therapeutics has recently tested amphiphile-bound CpG admixed with SARS-CoV-2 RBD protein to vaccinate mice, which resulted in 25-fold higher antigen-specific T cell responses and Th1 favored antibody responses (IgG2bc and IgG3) [127]. In another study, hydroxy-poly(ethylene glycol)-based cylindrical-shaped nanoparticles were used to deliver a model antigen, ovalbumin, which facilitated antigen draining to LN upon SC injection in mice [128]. These studies demonstrate the benefits of using nanoparticle delivery platforms to improve both LN targeted vaccine delivery and efficacy.

Chapter 2. Modulating Response of STING Agonists by Metal Ions

2.1. Abstract

Nutritional metal ions play critical roles in many important immune processes. Hence, effective modulation of metal ions may open up new forms of immunotherapy, termed as metalloimmunotherapy. Here, we screened various metal ions and discovered specific metal ions augmented STING agonist activity, wherein Mn^{2+} promoted a 12- to 77-fold potentiation effect across the prevalent human STING haplotypes. CDA + Mn^{2+} combination significantly elevated the expression levels of CD80 and CD86 on BMDCs and eradicated CT26 tumors in 80% of mice after IT injection. Mice treated with CDA + Mn^{2+} exhibited significantly elevated antigen-specific T cell response and prevent the survivors from CT26 tumor re-challenge performed on day 80. These results show that Mn^{2+} potentiates STING agonist activity *in vivo* and induces robust anti-tumor T cell response with long-term memory.

2.2. Introduction

Immunotherapy is revolutionizing cancer treatment in multiple fronts[129-131]; however, only a small subset of patients with solid tumors respond to immunotherapies[132]. The limited patient response rate has been attributed to poor anti-tumor immunity in “cold” tumors, which are characterized by a low frequency of pro-inflammatory immune cells and immunosuppressive network in the tumor

microenvironment (TME)[133]. Recent studies have shown that the stimulator of interferon genes (STING) pathway plays critical roles in the initiation of anti-tumor immune responses and conversion of “cold” tumor to “hot” tumor[134-137]. Briefly, cyclic GMP-AMP synthase (cGAS) detects damage-associated double-stranded DNA in the cytosol and catalyzes the generation of cyclic [G(2’,5’)pA(3’,5’)p] (cGAMP), which serves as the second messenger to activate STING and induce type-I interferons (IFNs)[134, 138-139]. Preclinical studies with STING agonists have shown promising anti-tumor efficacy[135-136]. Yet, because of their metabolic instability, limited cellular permeability, and poor drug-like properties, conventional CDN-based STING agonists have produced disappointing results in clinical trials[140-141].

Emerging evidence has indicated essential roles of metal ions in the regulation of many important immune processes[6-7], including T cell activation (Ca^{2+})[10-11] and stemness (K^{+})[8-9], activation of nucleotide-binding domain, leucine-rich containing protein P3 (NLRP3) inflammasome (K^{+}, Ca^{2+}, Na^{+})[12-14], pathogen-host interaction ($Fe^{2+/3+}$, Zn^{2+}, Mn^{2+}, Cu^{2+})[142-143], and cGAS-STING signaling (Zn^{2+}, Mn^{2+})[15, 144]. Immune modulatory functions of metal ions may be harnessed for disease treatment, termed as metalloimmunotherapy. For example, Mg^{2+} increases NKG2D expression and restores cytotoxicity of NK and T cell for EBV infection treatment[87]. Potassium (K^{+}) preserves T cell stemness and increases *in vivo* persistence and multi-potency of adoptively transferred T cells[8]. In particular, recent studies have shown that Mn^{2+} sensitizes the cGAS-STING pathway to double-stranded DNA during DNA virus infection[15] and synergizes with immune checkpoint inhibitors[92], chemotherapy[145], in-situ vaccine[146], and photodynamic therapy[147].

Here, we screened various metal ions for potential synergy with STING agonists and discovered that Mn^{2+} and Co^{2+} could significantly augment type-I IFN (IFN-I) activity of STING agonists. As Mn^{2+} is an essential inorganic trace element required for the immune system[15, 148] and is used in FDA-approved pharmaceuticals[149-151], we focused on the combination of Mn^{2+} and STING agonists. We report that Mn^{2+} markedly increases the type-I IFN activities of STING agonists in multiple human STING haplotypes.

2.3. Materials & Methods

2.3.1. Assessing metal ions for modulation of IFN-I response of STING agonists *in vitro*

Mouse bone marrow-derived dendritic cells (BMDCs) were isolated and cultured as reported previously[152]. Human monocyte cell line THP1 cells expressing $hSTING^{HAQ}$ were purchased from ATCC (Manassas, VA) and cultured according to ATCC's instruction. THP1 cells expressing $hSTING^{R232}$ (WT), $hSTING^{H232}$ (REF) were purchased from Invivogen and cultured according to Invivogen's instruction. To screen for metal ions for modulating IFN-I response of STING agonists, we seeded 0.1 million BMDCs or THP1 cells per well in 96-well plate, and metal ions (e.g., $ZnCl_2$, KCl, $MgCl_2$, $MnCl_2$, CaCl2, $Al_2(SO_4)_3$, $CuCl_2$, $FeCl_2$, $FeCl_3$, and $CoCl_2$) (Sigma-Aldrich) at various concentrations ranging 0-500 μM were added with or without 5 μM cGAMP (Invivogen). After 24 h incubation at 37 °C, 5% CO_2, the supernatants were collected for IFN-β ELISA assay (R&D). To evaluate the effect of $MnCl_2$ on IFN-I response of STING agonists in various human STING variants, the indicated concentrations of $MnCl_2$ and

STING agonists, including cGAMP, CDA (Invivogen), 2'3'-cGAM(PS)2 (Rp/Sp) (Invivogen), ADU-S100 (MedChemExpress) and diABZI (MedChemExpress), were added to 0.1 million THP1 reporter cells in 96-well plate. After 24 h incubation at 37 °C, 5% CO_2, the supernatants were collected and assessed for IFN-β by ELISA.

2.3.2. In vitro evaluation of BMDC activation and STING activation

BMDCs were prepared as described previously[152]. Briefly, bone marrow was harvested and plated in bacteriological Petri dishes with GM-CSF containing culture media. The cell culture media were refreshed on days 3, 6, and 8. After 8 days of differentiation, BMDC were harvested for use. To observe BMDC activation by CDNs and Mn^{2+}, 1×10^6/well BMDCs seeded in 12-well plate were incubated with 5 μM CDA and/or 250 μM Mn^{2+} for 24 h. Treated BMDCs were harvested, washed with FACS buffer (1% BSA in PBS), incubated with anti-CD16/32 at room temperature, and then stained on ice with fluorophore-labeled antibodies against CD11c, CD80, and CD86. Cells were then washed twice by FACS buffer, resuspended in 2 μg/ml DAPI solution, and analyzed by flow cytometry (Ze 5, Bio-Rad, USA).

To measure STING activation of STING agonists and/or Mn^{2+} in, 1 x 10^5/well BMDCs were seeded in 96-well plate and incubated with STING agonists and/or Mn^{2+}. After 24 h incubation at 37 °C, 5% CO_2, the supernatants were collected for ELISA assay of cytokines at the Cancer Center Immunology Core of the University of Michigan.

2.3.3. In vivo cancer immunotherapy

All animals were cared for following federal, state, and local guidelines. All work performed on animals was in accordance with and approved by the Institutional Animal Care & Use Committee (IACUC) at the University of Michigan, Ann Arbor. For CT26 murine tumor model, female BALB/c mice of age 6–8 weeks (Jackson Laboratories) were inoculated with 1.5 x 10^5 CT26 colon cancer cells subcutaneously on the right back flank. Tumor-bearing mice were randomly assigned to different treatment groups. Indicated drugs or formulations were administrated via indicated route at indicated time points. Tumor size and survival were monitored every 2-4 days. Tumor size was calculated based on equation: volume = length × $width^2$ × 0.5. Animals were euthanized when the tumor reached 1.5 cm in diameter or when animals became moribund with severe weight loss or un-healing ulceration. ELISPOT assay was performed with PBMCs from the treated mice, as described previously[153].

2.3.4. In vivo immune response analysis

For the IFN-γ ELISPOT assay, ELISPOT plate was coated with IFN-γ capture antibody for 24 h and blocked with DMEM + 10% FBS for 2 h. PBMCs obtained from treated mice were added to 96-well plate with a fixed number of alive cells/well. SPSYVYHQF peptide (20 μg/mL) was added to stimulate PBMCs. Ionomycin and PMA were employed as positive control. After 18 h, IFN-γ spots were detected with biotinylated detection antibody, followed by streptavidin-HRP and AEC substrate kit. The IFN-γ spot number and size were measured in the Cancer Center Immunology Core at the University of Michigan.

2.4. Results & Discussion

2.4.1 Screening of metal ions synergistic with STING agonists

We examined the cGAS-STING-type-I IFN pathway and screened various nutritional metal ions (e.g., Zn^{2+}, K^{+}, Mg^{2+}, Mn^{2+}, Ca^{2+}, Al^{3+}, Cu^{2+}, Fe^{3+}, Fe^{2+}, and Co^{2+}) for potentiating STING agonists as a new form of metalloimmunotherapy. To our surprise, adding either Mn^{2+} or Co^{2+} to cGAMP dramatically increased the type-I IFN production in murine bone marrow-derived dendritic cells (BMDCs) (**Fig. 2-1-1a**) as well as in human monocyte-like THP1 cells in a dose-dependent manner (**Fig. 2-1-2a, Fig. 2-1-1b**). Given the previous examples of Mn^{2+}-based pharmaceuticals[149-151], we further investigated the combination of Mn^{2+} and STING agonists. We examined the impact of Mn^{2+} on human *STING* haplotypes known to exhibit distinct response profiles to STING agonists. The addition of Mn^{2+} to various concentrations of cGAMP significantly amplified the type-I IFN responses in THP1 cells expressing $hSTING^{R232}$, $hSTING^{H232}$, or $hSTING^{HAQ}$, achieving 77-fold, 14-fold, and 12-fold dose-sparing effect, respectively (**Fig. 2-1-1c-e**). The allele frequencies of $hSTING^{R232}$, $hSTING^{H232}$, and $hSTING^{HAQ}$ in humans are 57.9%, 20.4%, and 13.7%, respectively[135]. Even the insensitive $hSTING^{H232}$, which did not respond to as high as 500 □M cGAMP, exhibited a strong IFN-□ response when Mn^{2+} was added **(Fig. 2-1-1e**), suggesting that Mn^{2+} offers a widely applicable strategy that covers > 90% allele frequency of human STING variants. In addition, Mn^{2+} in doses ranging from 500 □M down to 62.5 □M amplified the type-I IFN-inducing activities of other CDN-based STING agonists, including CDA[154], ADU-S100[135], 2'3'-cGAM(PS)2 (Rp/Sp)[155], as well as a non-CDN STING agonist, diABZI[156] (**Fig. 2-1-2b-e, 2-1-3a-e**). These results indicate that Mn^{2+}-mediated potentiation of

STING agonists is a general phenomenon independent of STING variants and STING agonist structures.

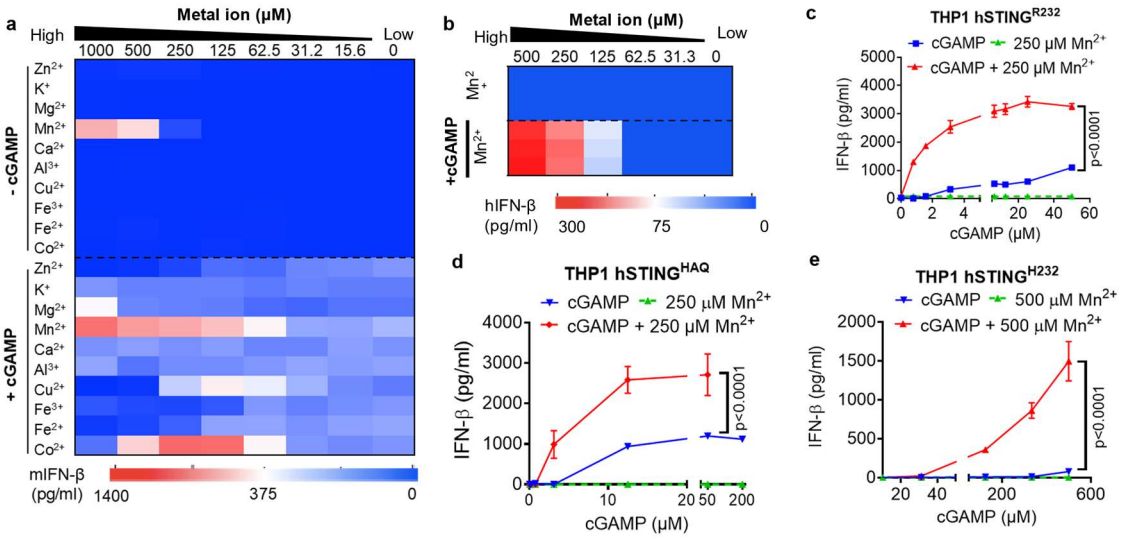

Figure 2-1-1. Mn^{2+} augments type-I IFN activity of STING agonists. a) BMDCs or b) human THP1 monocyte cells were incubated with various concentrations of metal ions (0-500 μM) ± 5 μM cGAMP, and after 24 h, IFN-β secretion was quantified by ELISA. c-e) THP1 cells expressing c) $hSTING^{R232}$, d) $hSTING^{HAQ}$, or e) $hSTING^{H232}$ were treated for 24 h with cGAMP ± Mn^{2+}, followed by quantification of IFN-β production.

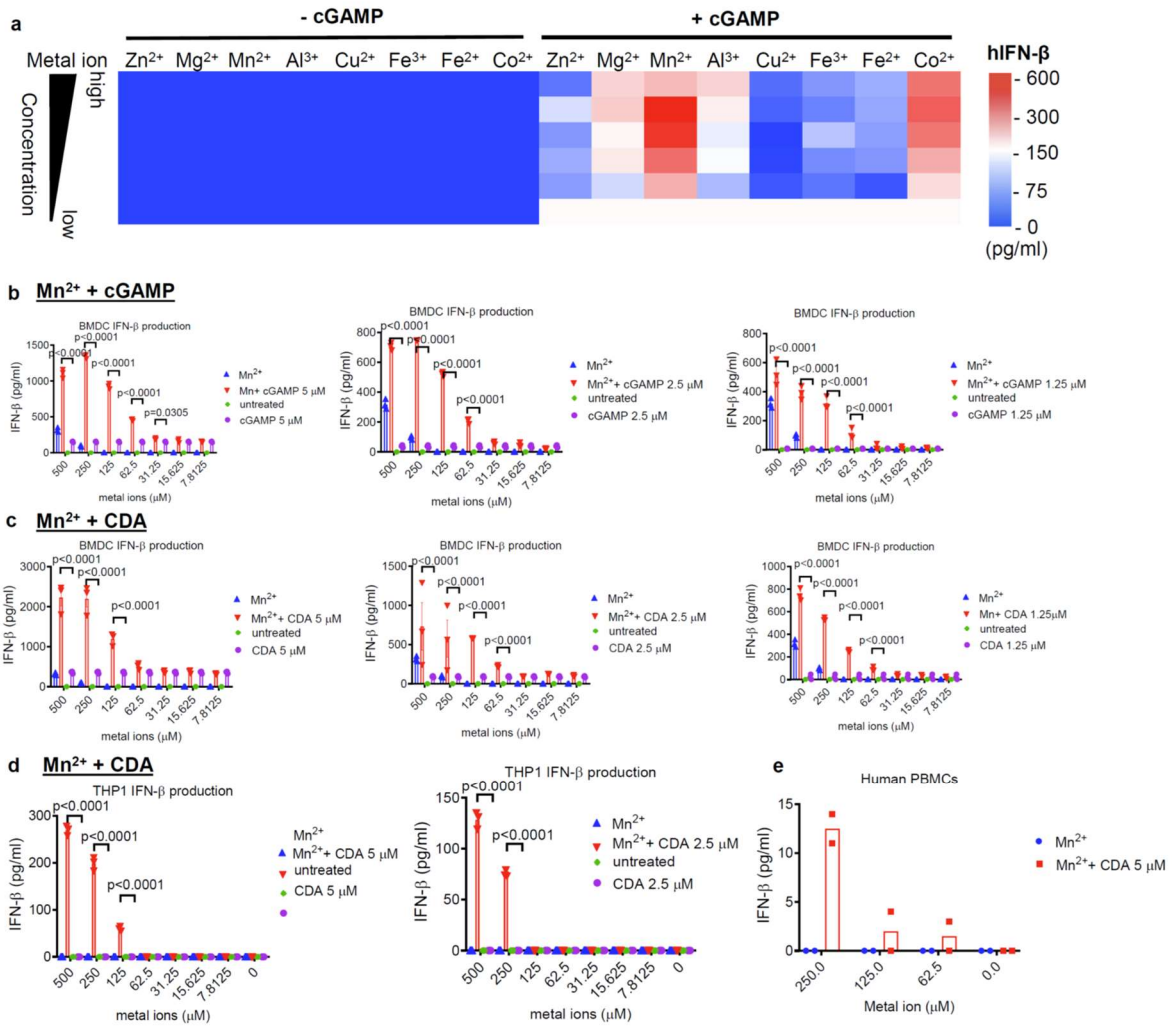

Figure 2-1-2. Mn^{2+} augments type-I IFN activity of STING agonists. a) Screening of metal ions for augmenting type-I IFN response of STING agonists in THP1 cells. THP1 monocyte cells were incubated with various concentrations of metal ions (0-500 μM) ± cGAMP, and after 24 h, human IFN-β secretion was quantified by ELISA. **b-c)** BMDCs were treated with various concentrations of Mn^{2+} with either cGAMP (b) or c-di-AMP (CDA) (c), after 24 h, mouse IFN-β secretion was quantified by ELISA. **d-e**) Human THP1 cells (d) or primary human PBMCs (e) were treated with various concentrations of Mn^{2+} ± CDA, and after 24 h, hIFN-β secretion was quantified by ELISA. Data represent mean ± SEM, from a representative experiment from 2 independent experiments with *n* = 3 (b-d) or n = 2 (e) biologically independent replicates. Data are analyzed by two-way ANOVA with Bonferroni's multiple comparisons test (b-d).

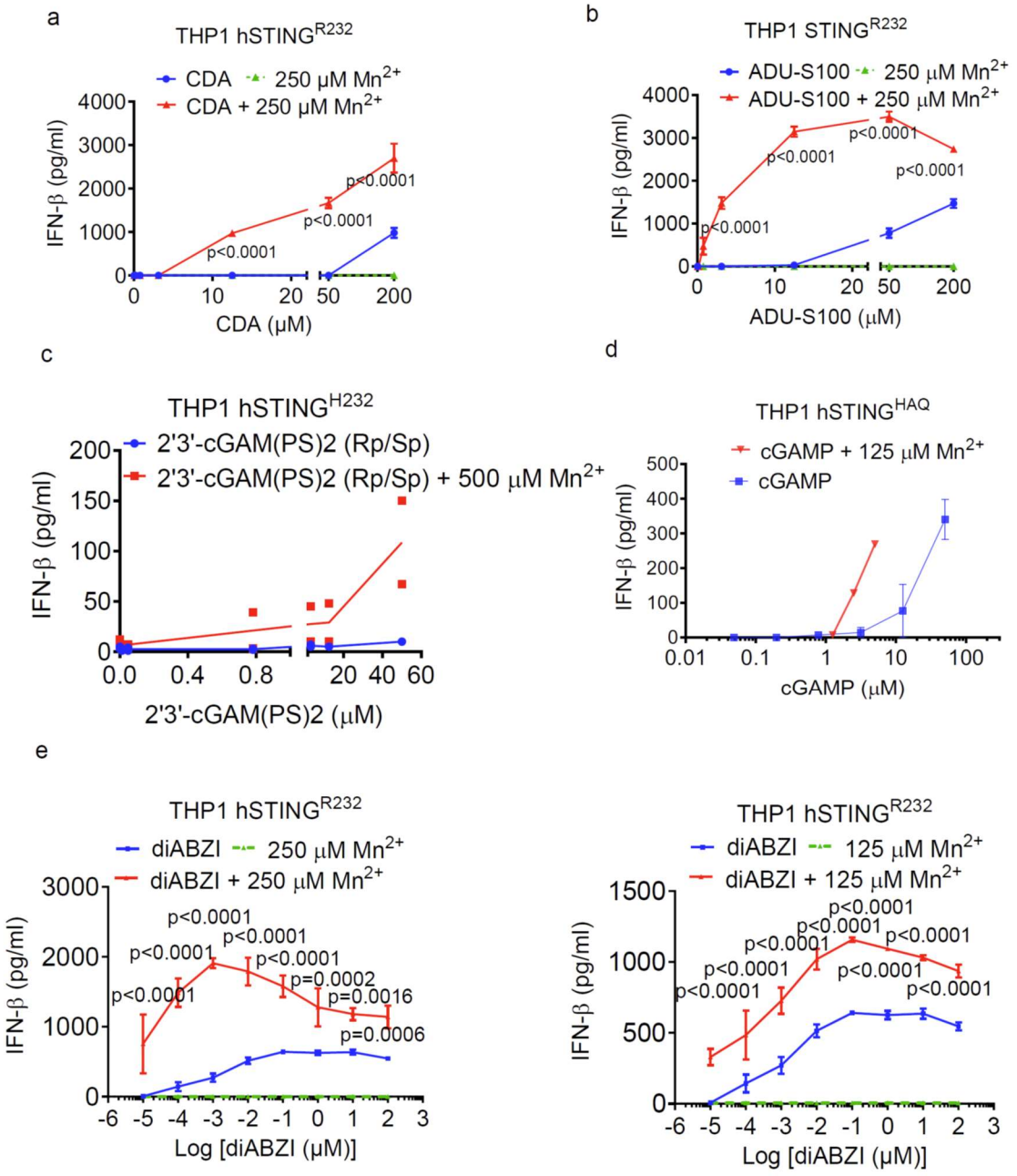

Figure 2-1-3. Mn^{2+} augments type-I IFN activity of CDN- and non-CDN-based STING agonists. a-b) THP1 cells expressing hSTING^{R232} were incubated with Mn^{2+} and various concentrations of CDA (a) or ADU-S100 (b). After 24 h, hIFN-β secretion was quantified by ELISA. **c)** THP1 cells expressing hSTING^{H232} were incubated with Mn^{2+} and various concentrations of 2'3'-cGAM(PS)2 (Rp/Sp), and after 24 h, hIFN-β secretion was quantified by ELISA. **d)** THP1 cells expressing hSTING^{HAQ} were incubated with Mn^{2+} and various concentrations of cGAMP, and after 24 h, hIFN-β secretion was quantified by

ELISA. **e)** THP1 cells expressing hSTING^{R232} were incubated with Mn^{2+} and various concentrations of diABZI, and after 24 h, hIFN-β secretion was quantified by ELISA. Data represent mean ± SEM, from a representative experiment from 2 independent experiments with *n* = 3-4 (a-b, d-e) or n =2 (c) biological independent replicates. Data are analyzed by two-way ANOVA with Bonferroni's multiple comparisons test (a-b, d-e).

2.4.2 Mechanism of potentiation effect of Mn2+ on STING agonist activity

To characterize the mechanism of Mn^{2+}-amplified STING activation, we first performed a thermal shift assay of STING (both hSTING^{R232} and hSTING^{H232}) binding to various STING agonists. However, regardless of the STING agonists and STING variants of choice, Mn^{2+} did not increase the binding affinity between STING and STING agonists (**Fig. 2-2-2**). Thus, we examined the impact of STING agonist + Mn^{2+} on downstream of the STING-IFN-I signaling pathway. Maximal transcription of IFN-I genes depends on the formation of an enhanceosome, which contains phosphorylated IRF3 and p65[157-159]. Hence, we sought to determine whether Mn^{2+} has an impact on the phosphorylation of these two transcription factors. We found that the combination of cGAMP + Mn^{2+} potently enhanced the levels of phosphorylated TBK1, IRF3, and p65 in hSTING^{R232} THP1 cells (**Fig. 2-2-1**). Interestingly, Mn^{2+} alone without cGAMP still induced phosphorylation of TBK1 and p65 (**Fig. 2-2-1**). Notably, in STING-knockout THP1 cells and STING-deficient murine STING$^{gt/gt}$ BMDCs, Mn^{2+} triggered STING-independent phosphorylation of TBK1 and p65, but not IRF3[160] (**Fig. 2-2-1, Fig. 2-2-3**). In hSTING^{R232} THP1 cells, hSTING^{H232} THP1 cells, and murine WT BMDCs, addition of JSH-23, an inhibitor of p65 nucleus translocation[161], abrogated IFN-β production promoted by cGAMP + Mn^{2+} (**Fig. 2-2-1, 2-2-3**). Overall, these results show that Mn^{2+} has STING-independent immune activating potential by inducing the phosphorylation of TBK1 and p65, which is further augmented and translated to IRF3 phosphorylation in

the presence of STING agonists, resulting in potent amplification of the STING signaling cascade and production of type-I IFNs (**Fig. 2-2-1c**).

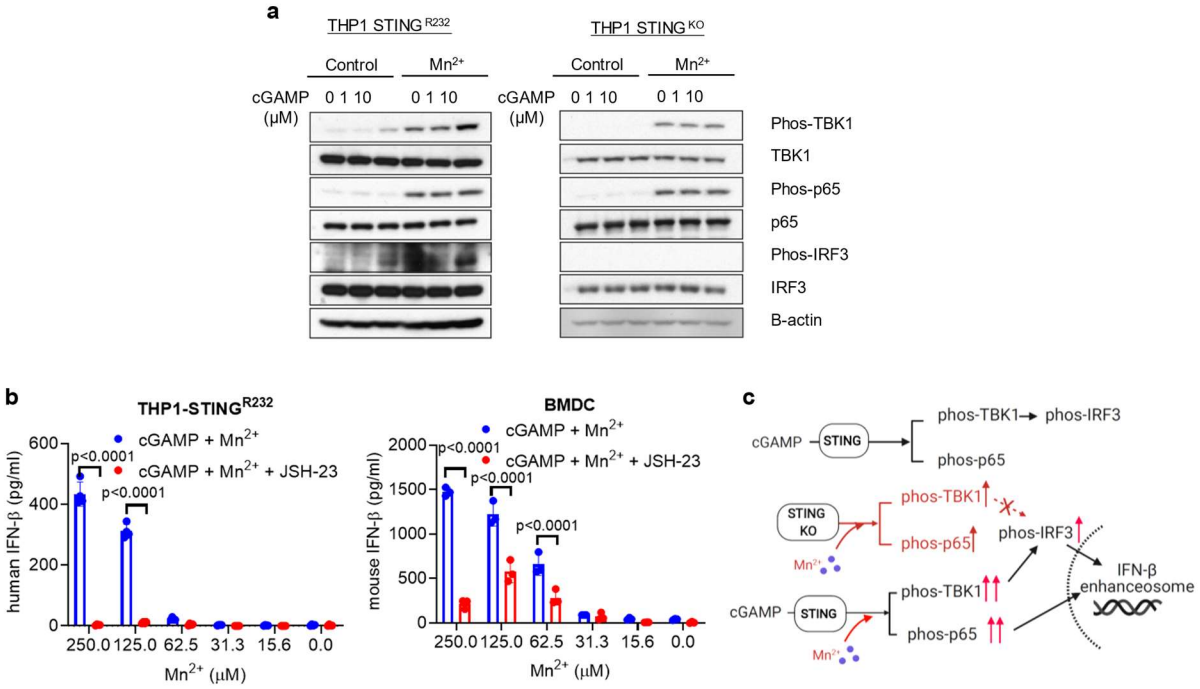

Figure 2-2-1. Mechanism study of Mn^{2+}-mediated potentiation of STING agonist. a) Combination of STING agonist and Mn^{2+} increases STING-independent phosphorylation of TBK1 and p65 and STING-dependent phosphorylation of IRF3. THP-1 $STING^{R232}$ cells were incubated with increasing concentrations of cGAMP with or without 250 μM Mn^{2+} for 6 hours, followed by Immunoblotting for marker proteins in the STING-IFN-I signaling pathway. **b)** Pharmacological inhibition of p65 nucleus translocation with JSH-23 inhibited Mn^{2+}-potentiated IFN-β production. **c**) Proposed mechanism of Mn^{2+}-mediated potentiation of STING agonist via STING-independent TBK1 and p65 phosphorylation and STING-dependent IRF3 phosphorylation. Activation of p65 and IRF3 further facilitates assembly of the IFN-β transcriptional enhanceosome.

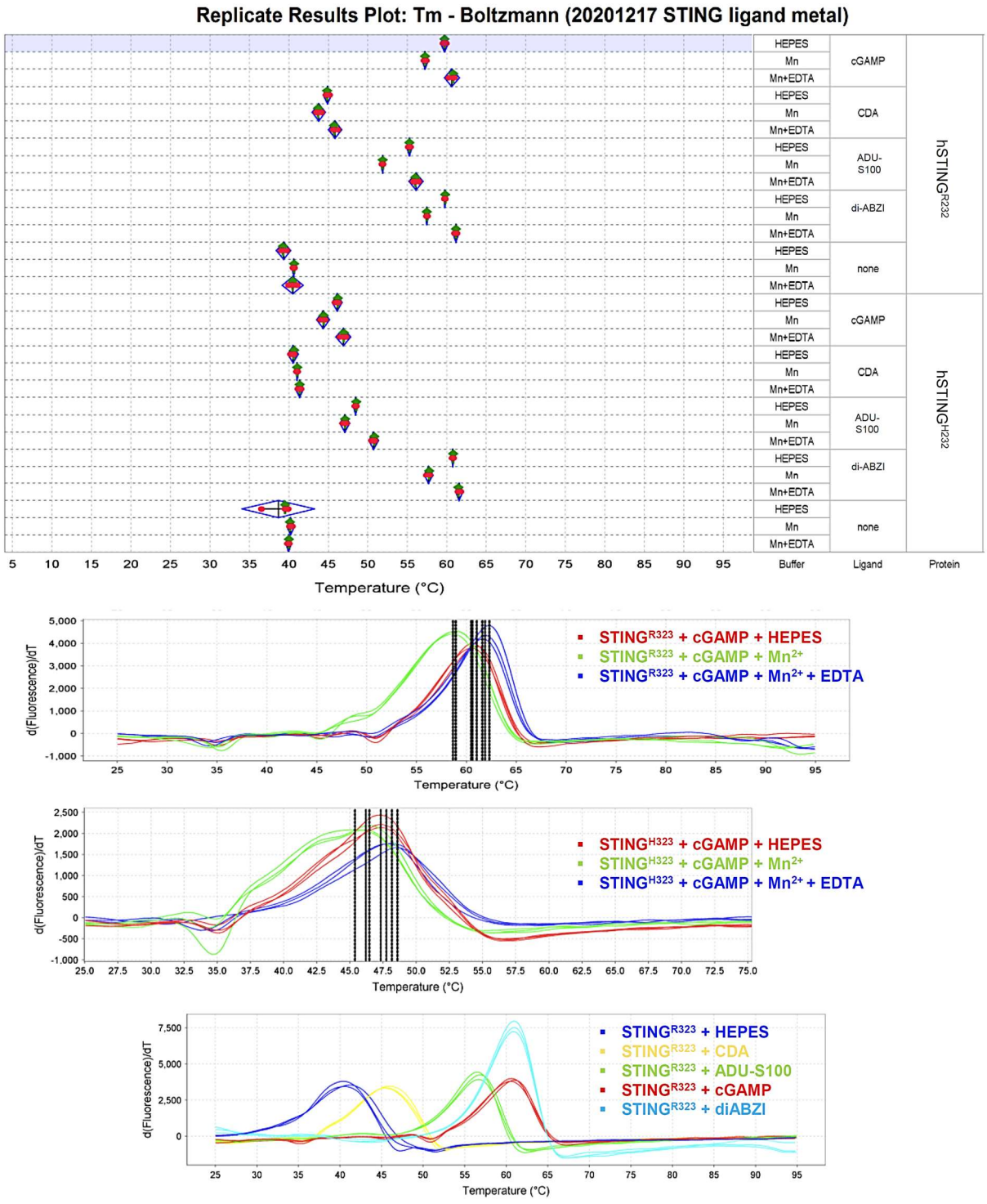

Figure 2-2-2. Thermal shift assay of STING-STING agonist complexes with Mn^{2+} or without Mn^{2+}. The thermal shift assay of STING-STING agonist complexes was conducted according as reported previously[162]. STING agonists (cGAMP, CDA, ADU-S100, di-ABZI) and human recombinant STING proteins, $hSTING^{R232}$ and $hSTING^{H232}$ (Cayman Chemical), were prepared in TSA buffer (150 mM NaCl, 50 mM HEPES, pH

7.4). STING agonists and STING proteins were mixed in three buffer conditions: 1) with 10 mM $MnCl_2$, 2) without $MnCl_2$ (HEPES), or 3) with 10 mM $MnCl_2$ + 100 mM EDTA. The final concentrations of the ligand and protein were 150 and 4 μM, respectively. The mixtures were incubated on ice for 10 min. SYPRO Orange Protein Gel Stain (Sigma–Aldrich) was subsequently added (final 5x concentration) and the mixtures were again incubated on ice for a further 10 min. The protein melting curves were measured with Roche LightCycler QPCR instrument and analyzed by the LightCycler software.

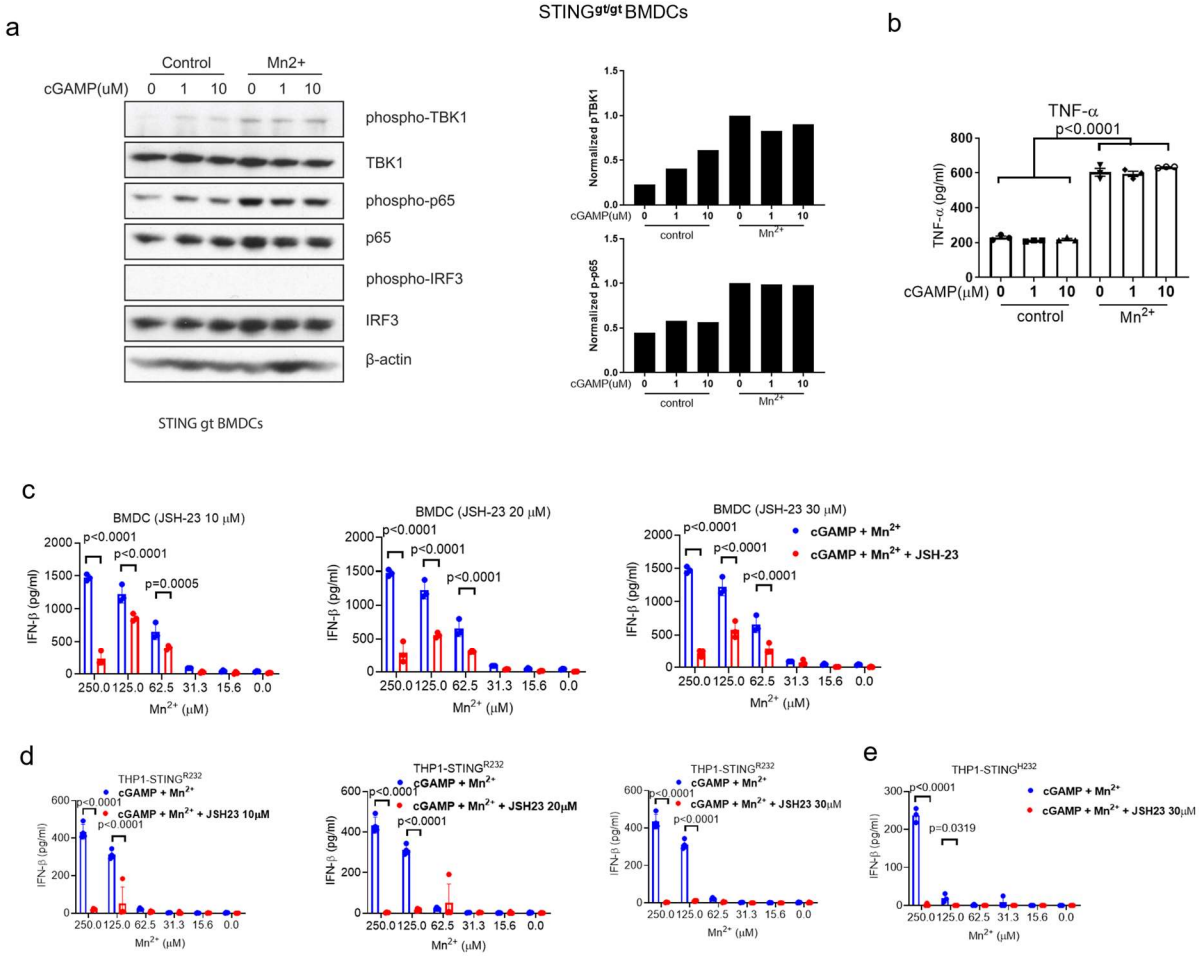

Figure 2-2-3. Impact of STING agonist + Mn^{2+} on the STING signaling cascade. a) Combination of STING agonist and Mn^{2+} increased STING-independent TBK1 and p65 phosphorylation in $STING^{gt/gt}$ BMDCs. $STING^{gt/gt}$ BMDCs were harvested from Homozygotes C57BL/6J-$Sting1^{gt/gt}$ mice and prepared according to a previously reported method[152]. $STING^{gt/gt}$ BMDCs were incubated with increasing concentrations of cGAMP with (+ Mn^{2+}) or without 250 □M Mn^{2+} (control) for 6 hours. Cells were lysed in NP40-based buffer in the presence of cocktail proteinase inhibitor and phosphatase inhibitor at 4 °C. Cell lysates were subjected to SDS-PAGE and immunoblotted against marker proteins for STING-IFN-I signaling activation. Densitometry was quantified by ImageJ. **b)** TNF-α in the cell culture media was measured by ELISA. **c-e)** Inhibition of nucleus translocation of p65 reduces Mn^{2+}-mediated potentiation of IFN-β production. **c**, BMDC cells were incubated with cGAMP and serial concentration of Mn^{2+} in presence or absence of JSH23 (10, 20, 30 μM). After 24 h incubation, IFN-β secretion was quantified by ELISA. **d,** THP-1 THP1 cells expressing $hSTING^{R232}$ were incubated with cGAMP and serial concentrations of Mn^{2+} in presence or absence of JSH23 (10, 20, 30 μM). After 24 h incubation, hIFN-β secretion was quantified by ELISA. **e**, THP1 cells expressing $hSTING^{H232}$ were incubated with cGAMP and serial concentrations of Mn^{2+} in presence or absence of JSH23 (30 μM). After 24 h incubation, hIFN-β secretion was quantified by ELISA. Data represent mean ± SEM (*n* = 3 biologically independent samples (b, c-e) and were analyzed by (b) one-way ANOVA or (c-e) two-way ANOVA with Bonferroni's multiple comparisons test.

2.4.3. Mn-CDN combination increase DC activation and cancer immunotherapy efficacy

We further evaluated the effects of STING agonist + Mn^{2+} combination on the activation of DCs. While CDA or Mn^{2+} promoted BMDC maturation as single agents, the CDA + Mn^{2+} combination significantly elevated the expression levels of CD80 and CD86 on BMDCs (**Fig. 2-3-1**). We also evaluated the therapeutic efficacy of the CDA + Mn^{2+} combination *in vivo*. BALB/c mice were inoculated with CT26 colon carcinoma cells subcutaneously (S.C.) on day 0, and 20 μg CDA, 17.5 μg Mn^{2+} (in 40 μg $MnCl_2$), or their combination was administered directly into tumors on days 9, 12, and 15 (**Fig. 2-3-2**). I.T. administration of CDA + Mn^{2+} eradicated CT26 tumors in 80% of mice (**Fig. 2-3-2 a-c**). In contrast, CDA monotherapy eliminated tumors in only 40% of mice, while $MnCl_2$ treatment exhibited no anti-tumor efficacy (**Fig. 2-3-2 a-c**). We assessed CD8+ T cell

responses against CT26 cells by performing IFN-γ ELISPOT assay with peripheral blood mononuclear cells (PBMCs) re-stimulated with AH1 epitope (H-2L^{d}–restricted SPSYVYHQF, the immunodominant MHC-I minimal epitope of CT26 gp70^{163}). Mice treated with CDA + Mn^{2+} exhibited significantly elevated antigen-specific T cell response, compared with either CDA or Mn^{2+} monotherapy (**Fig. 2-3-2 d**). In addition, 100% of survivors from the CDA+ Mn^{2+} treatment group were resistant to CT26 tumor re-challenge performed on day 80 (**Fig. 2-3-2 e**). These results show that Mn^{2+} potentiates STING agonist activity *in vivo* and induces robust anti-tumor T cell response with long-term memory.

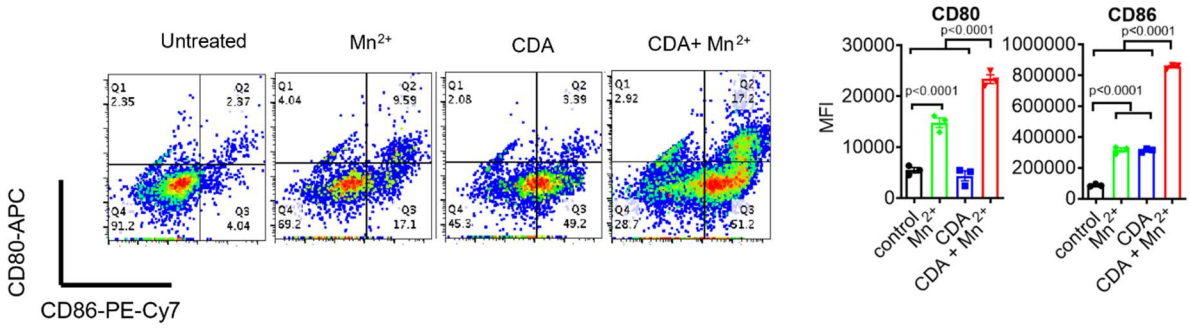

Figure 2-3-1. Impact of STING agonist + Mn^{2+} on BMDC maturation. BMDCs were treated with 5 μM CDA, 250 μM Mn^{2+}, or equivalent amount of CDA + Mn^{2+} for 24 h. CD80 and CD86 were examined by flow cytometry. Shown are the representative scatter plots and mean fluorescence intensity (MFI) of CD80 and CD86 expression.

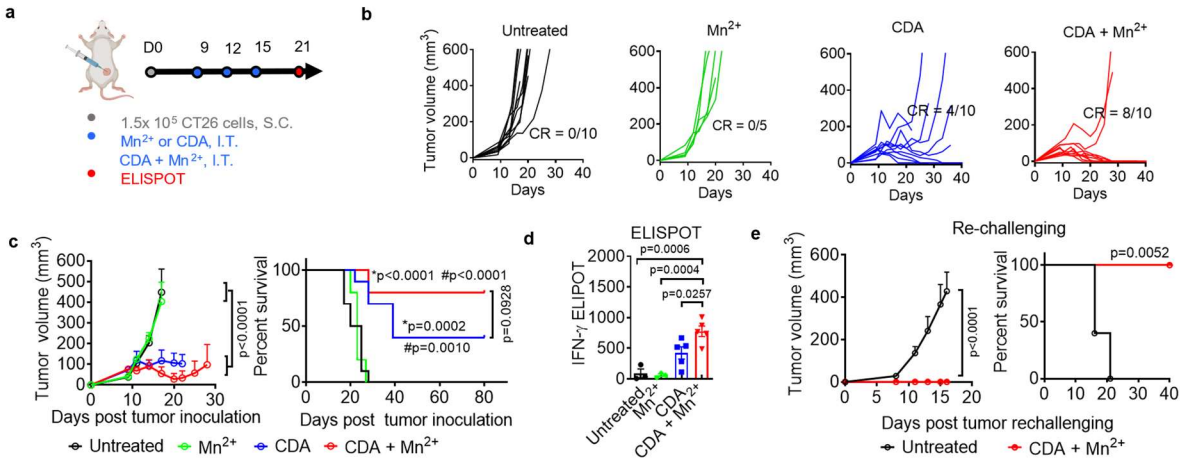

Figure 2-3-2. STING agonist + Mn^{2+} combination for in-vivo cancer immunotherapy. **a-c)** BALB/c mice were inoculated with 1.5 x 10^5 CT26 tumor cells at the S.C. flank and treated by I.T. administration of 20 μg CDA, 17.5 μg Mn^{2+}, or their combination on days 9, 12, and 15 **(a)**. Mice were monitored for tumor growth **(b, c)** and survival **(c)**. **d)** AH1-specific T cells were assessed among PBMCs by ELISPOT on day 21. **e)** Survivors from CDA + Mn^{2+} group were re-challenged with CT26 cells on day 80, followed by monitoring for tumor growth and survival. Data represent mean ± SEM, from a representative experiment from 2 independent experiments with *n* = 5-10 biologically independent samples. **P* < 0.05, ***P* < 0.01, ****P* < 0.001, *****P* < 0.0001, analyzed by (d) one-way ANOVA or (c, e) two-way ANOVA with Bonferroni's multiple comparisons test, or (c, e) log-rank (Mantel-Cox) test. * and # in (j) denote the significance relative to the Untreated and Mn^{2+} groups, respectively

Chapter 3. Amplifying STING Activation by CDN Manganese Particle (CMP) for Systemic and Local Cancer Metalloimmunotherapy

3.1. Abstract

Effective metalloimmunotherapy will provide new opportunities to cure cancer patients. Here, we demonstrate a prototype of effective cancer metalloimmunotherapy using cyclic dinucleotide (CDN) stimulator of interferon genes (STING) agonists and Mn^{2+} in an optimized pharmaceutical formulation. Notably, Mn2+ coordinated with CDN STING agonists to self-assemble into a nanoparticle (CDN-Mn2+ particle, CMP) that effectively delivered STING agonists to immune cells. CMP administered either by local intratumoral or systemic intravenous injection initiated robust anti-tumor immunity, achieving remarkable therapeutic efficacy with minute doses of STING agonists in multiple murine tumor models. Overall, CMP offers a new platform for local and systemic cancer treatments, and this work underscores the great potential of coordination nanomedicine for metalloimmunotherapy.

3.2. Introduction

Recent studies have shown that the stimulator of interferon genes (STING) pathway plays critical roles in the initiation of anti-tumor immune responses and conversion of “cold” tumor to “hot” tumor[134-137]. Briefly, cyclic GMP-AMP synthase (cGAS) detects damage-associated double-stranded DNA in the cytosol and catalyzes

the generation of cyclic [G(2',5')pA(3',5')p] (cGAMP), which serves as the second messenger to activate STING and induce type-I interferons (IFNs)[134, 138-139]. Preclinical studies with STING agonists have shown promising anti-tumor efficacy[135-136]. Yet, because of their metabolic instability, limited cellular permeability, and poor drug-like properties, conventional CDN-based STING agonists are administered intratumorally (I.T.)[140-141]. However, the I.T. route of administration is not applicable for treating metastasis, and I.T. injection of CDN-based STING agonists have produced disappointing results in clinical trials[140-141]. While new STING agonists based on non-CDN structures have been recently reported for systemic administration[156, 164-166], their toxicity profiles and efficacy are yet to be studied in clinical trials. Alternatively, nanoparticles, such as those based on polymers and liposomes, could augment the local and systemic therapeutic effects of CDN-based STING agonists[137, 167-171], thus underscoring the potential and utility of nanomedicine-based delivery of STING agonists.

As discussed in Chapter 2, we have found Mn^{2+} could greatly increase the activity of STING agonists in vitro and in vivo. Also, other groups have recently reported Mn^{2+} sensitizes the cGAS-STING pathway to double-stranded DNA during DNA virus infection[15] and synergizes with immune checkpoint inhibitors[92], chemotherapy[145], in-situ vaccine[146], and photodynamic therapy[147]. Despite their promise, it remains largely unknown how to systemically develop an effective metalloimmunotherapy and deliver them in appropriate pharmaceutical forms. In this chapter, we will demonstrate that Mn^{2+} self-assembles with CDN STING agonists to form a coordination nanoparticle (CDN-Mn^{2+} Particle, CMP) that elicits robust anti-tumor immunity after local or systemic administration

(Fig. 3-1a-b). Using c-di-AMP (CDA) as an example, we show that CMP_{CDA} administered via either intratumoral (I.T.) or intravenous (I.V.) route significantly increased STING activation *in vivo*, reversed immunosuppression in the TME, and exerted remarkable anti-tumor efficacy **(Fig. 3-1c)**. Overall, CMP, a coordination nanomedicine composed of bioactive metal ions and STING agonists, is a promising novel platform for metalloimmunotherapy.

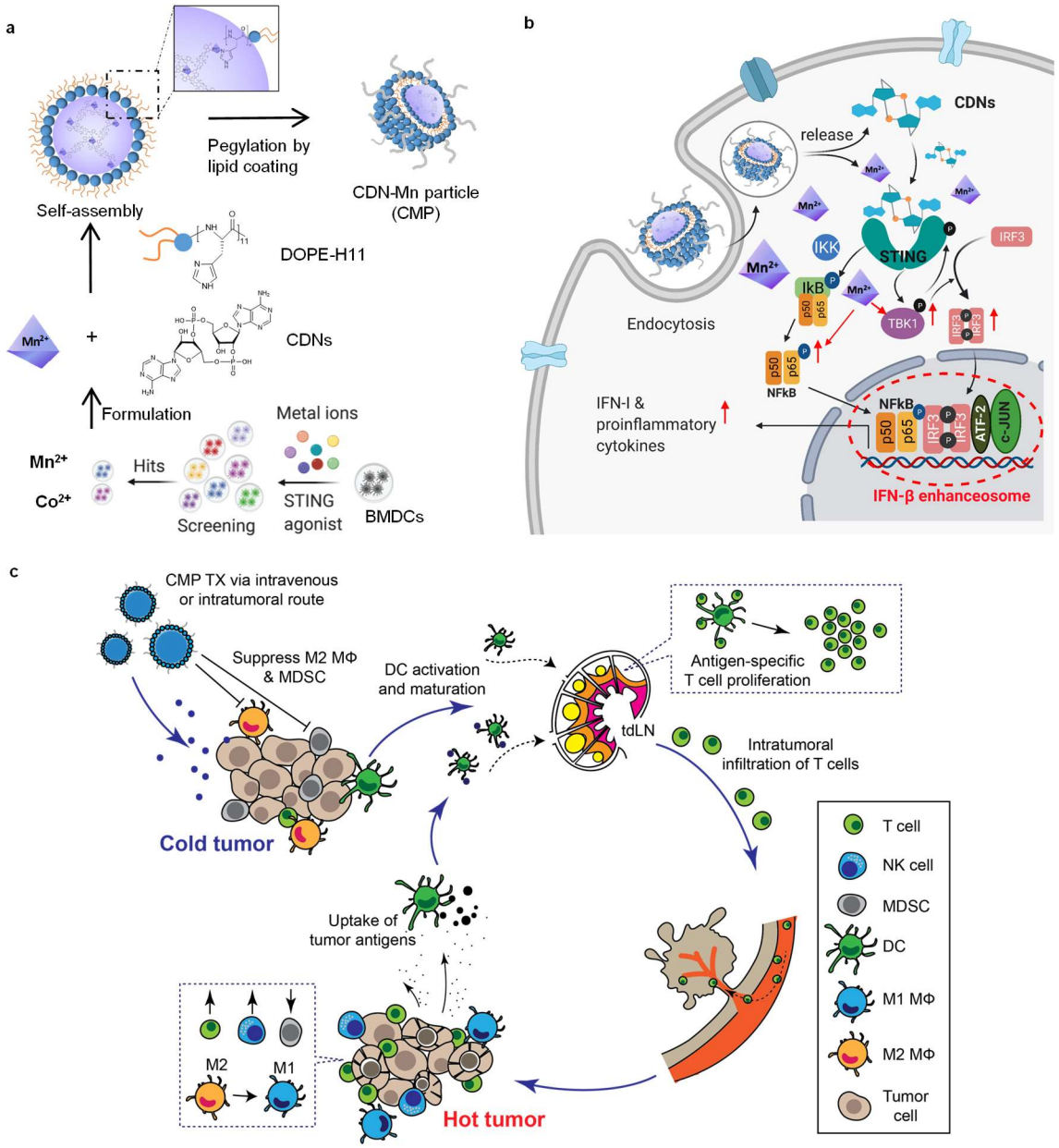

Figure 3-1. Amplifying STING activation with CDN-Manganese particles (CMP) for cancer metalloimmunotherapy. a) CMP is composed of cyclic di-nucleotides (CDNs), manganese ions (Mn^{2+}), phospholipid-histidine11 (DOPE-H11), and a PEG-lipid layer (DOPC: cholesterol: DSPE-PEG5000). Mn^{2+} potentiates type-I IFN activities of STING agonists. Mn^{2+} and CDNs self-assemble into coordination polymer. CDN-Mn^{2+} coordination polymer was coated with DOPE-H11 via Mn-histidine coordination to form CDN-Mn@DOPE, followed by PEGylation with PEG-lipid layer, resulting in the formation of CMP. **b)** CMP boosts STING activation: 1) CMP promotes cellular uptake of CDNs and Mn^{2+}; 2) Mn^{2+} augments CDN-induced STING activation via STING-independent TBK1 and p65 phosphorylation, STING-dependent IRF3 phosphorylation, and assembly of the IFN-β transcriptional enhanceosome. **c)** CMP exerts potent anti-tumor efficacy after intratumoral (I.T.) or intravenous (I.V.) administration. CMP reverses immunosuppressive tumor microenvironment, while activating T cells, natural killer (NK) cells, and dendritic cells (DCs).

3.3. Materials & Methods

3.3.1. Synthesis and characterization of CDN-Mn/Zn coordination polymer, CMP_{CDA}, CZP_{CDA}, and CDA liposomes

c-di-AMP, c-di-GMP, or cGAMP (Invivogen) were dissolved in methanol in 1 mg/ml. $MnCl_2$ or $ZnCl_2$ (Sigma-Aldrich) was dissolved in methanol to prepare 100 mM stock solution. In a typical synthesis reaction, $MnCl_2$ or $ZnCl_2$ (Sigma-Aldrich) solution was added to 1 mg/ml CDNs solution in a 10:1 (n/n) ratio under vigorous stirring. The mixture was sonicated for 1 min and stirred for another 1 h at room temperature. The resulting CDN-Mn was centrifuged at 20000 x g for 10 min to remove free CDNs and metal ions, followed by washing with methanol.

CMP was synthesized according to a method adapted from previous reports[172-174]. First, dioleoyl-*sn*-glycero-3-phosphoethanolamine-N-$[histidine]_{11}$ (DOPE-H11) was synthesized by reaction of DOPE-NHS and H11 (2 eq) in DMF, purified by dialysis using 2KD MWCO dialysis tubes, and characterized by HPLC. A mixture containing 1ml of 1 mg/ml CDA in methanol, 0.14 ml of 100 mM $MnCl_2$ in methanol and 2 ml of 2 mg/ml

DOPE-H11 in ethanol was sonicated and then vortexed overnight, followed by centrifugation at 20000 x g for 10 min. The resulting CDA-Mn@DOPE was resuspended in ethanol containing DOPC: cholesterol: DSPE-PEG5000 (4:1:1), sonicated, and added into a solution of 30% (v/v) ethanol/H_2O. Lastly, CMP was obtained by evaporating the organic solvent under reduced pressure and washing with 10% sucrose using 100KD (MWCO) centrifugal ultrafiltration. CZP was synthesized using the same method except for replacing $MnCl_2$ with $ZnCl_2$. CDA liposomes were synthesized as reported previously[167].

Loading of CDA in CMP, CZP, and CDA liposomes was quantified by UV-absorbance at 260 nm, followed by verification by HPLC. Loading of Mn^{2+} in CMP was quantified by inductively coupled plasma-mass spectrometry (The Perkin-Elmer Nexion 2000 ICP-MS) and verified by thermogravimetric analysis (Discovery TGA, TA Instrument, New Castle, DE). The size and surface charge of CMP were measured by Zetasizer (Nano ZSP, Malvern, UK). The morphology of CDN-Mn was observed by transmission electron microscopy (TEM). All images were acquired on JEM 1200EX electron microscope (JEOL USA, Peabody, MA) equipped with an AMT XR-60 digital camera (Advanced Microscopy Techniques Corp. Woburn, MA).

3.3.2. In vitro evaluation of BMDC cellular uptake and STING activation

BMDCs were prepared as described previously[152]. Briefly, bone marrow was harvested and plated in bacteriological Petri dishes with GM-CSF containing culture media. The cell culture media were refreshed on days 3, 6, and 8. After 8 days of differentiation, BMDC were harvested for use. To visualize and quantify cellular uptake

of STING agonist, fluorophore-labeled CDN, CDG-Dy547 (Biolag, Bremen, German), was admixed with CDA (1:10, n/n) to prepare CDG-Dy547@CMP_{CDA} following the same synthesis procedure as CMP_{CDA} mentioned above. Loading of CDG-Dy547 in CMP was quantified by absorbance at 550 nm. BMDCs were seeded at 1 x 10^6 cells on 35 mm Petri dishes (MatTek Corp., Ashland, MA) and incubated with CDG-Dy547 in free form or in CDG-Dy547@CMP_{CDA} for 6, 12, or 24 h. For confocal imaging, cells were washed 3 times with PBS, incubated with 50 nM LysoTracker® green DND-99 (Invitrogen) for 30 min at 37 °C to stain lysosomes, and then imaged using a confocal microscope (Nikon A1). For cellular uptake quantification, cells were harvested and washed with FACS buffer (1% BSA in PBS). The fluorescence of CDG-Dy547 was analyzed by flow cytometry (Ze 5, Bio-Rad, USA).

To measure STING activation of CDA and/or Mn^{2+} in free form or in CMP_{CDA}, 1 x 10^5/well BMDCs were seeded in 96-well plate and incubated with CDA and/or Mn^{2+} in free form or in CMP_{CDA} (containing 2.5 μM CDA or/and 15.6 μM Mn^{2+}). After 24 h incubation at 37 °C, 5% CO_2, the supernatants were collected for ELISA assay of cytokines at the Cancer Center Immunology Core of the University of Michigan.

3.3.3. In vivo cancer immunotherapy

All animals were cared for following federal, state, and local guidelines. All work performed on animals was in accordance with and approved by the Institutional Animal Care & Use Committee (IACUC) at the University of Michigan, Ann Arbor. For CT26 murine tumor model, female BALB/c mice of age 6–8 weeks (Jackson Laboratories) were inoculated with 1.5 x 10^5 CT26 colon cancer cells subcutaneously on the right back flank.

For CT26 two-tumor model, 3 x 10^5 and 1 x 10^5 CT26 tumor cells were inoculated on the right (primary) and left (distal) flank, respectively. For the B16F10 tumor model, C57BL/6 mice (Jackson Laboratory) were inoculated with indicated number of B16F10 cells subcutaneously on the right flank. Tumor-bearing mice were randomly assigned to different treatment groups. Indicated drugs or formulations were administrated via indicated route at indicated time points. Tumor size and survival were monitored every 2-4 days. Tumor size was calculated based on equation: volume = length × width^2 × 0.5. Animals were euthanized when the tumor reached 1.5 cm in diameter or when animals became moribund with severe weight loss or un-healing ulceration. At indicated time points, the cytokine levels in serum were measured by ELISA assay in the Cancer Center Immunology Core of the University of Michigan. The percentages of tumor antigen-specific CD8α+ T cells among PBMC were analyzed using the tetramer staining assay as described previously with AH1 peptide-MHC tetramer (H-2Kb-restricted AH1 (SPSYVYHQF)) (the NIH Tetramer Core Facility, Atlanta, GA). ELISPOT assay was performed with PBMCs from the treated mice, as described previously[153].

NOOC1 was maintained in the IMDM media (Gibco cat#12440053). To make 1L of growth media for NOOC1, 626 ml IMDM base was mixed with 313 ml F-12 nutrient mix (Gibco cat#11765054), 50 ml FBS (Hyclone cat#SH3039603), 10 ml Pen Strep (Thermo Fisher cat#15-140-122), 1.25ml of 4mg/ml insulin (Invitrogen cat#12585014), 200 ml of 200 mg/ml hydrocortisone (Sigma-Aldrich cat#H0888-1G), and 50 ml of 100 mg/ml EGF (EMD Millipore cat#01-107). For *in vivo* implantation, Matrigel (Thermo Fisher cat#CB-40230) was thawed overnight at 4°C. On the day of injection, NOOC1 was washed once with PBS and mixed with Matrigel to reach a density of 2×10^7 cells/ml. Each mouse was

inoculated subcutaneously with 2×10^6 cells (100 ml). Tumor size and survival were monitored every 2 or 3 days as indicated above.

3.3.4.In vivo immune response analysis

T cell phenotypic and functional assessment in PBMC were analyzed. Briefly, PBMCs were collected after removing red blood cells by ACK lysis buffer. Fc receptor of PBMCs was blocked with CD16/32 antibody for 10 min. To analyze tumor antigen-specific $CD8^+$ T cells response and T cell memory phenotype, cell pellets were first stained with PE-tagged AH1 peptide-MHC tetramer, and then further stained with APC-CD8a rat anti-mouse (Clone: 53-6.7(RUO), BD Biosciences), with FITC-CD44 rat anti-human/mouse (Clone: IM7, eBioscience) and PE-Cy7-CD62L monoclonal antibody (Clone: MEL-14, eBioscience). Stained cells were incubated with DAPI prior to flow cytometry analysis (Ze5, Bio-Rad).

For the IFN-γ ELISPOT assay, ELISPOT plate was coated with IFN-γ capture antibody for 24 h and blocked with DMEM + 10% FBS for 2 h. PBMCs obtained from treated mice were added to 96-well plate with a fixed number of alive cells/well. SPSYVYHQF peptide (20 μg/mL) was added to stimulate PBMCs. Ionomycin and PMA were employed as positive control. After 18 h, IFN-γ spots were detected with biotinylated detection antibody, followed by streptavidin-HRP and AEC substrate kit. The IFN-γ spot number and size were measured in the Cancer Center Immunology Core at the University of Michigan.

Tumor tissues were analyzed as described before[163]. Tumor tissues were excised at preset time points and cut into small pieces, which were treated additionally with

collagenase type IV (1 mg/ml) and DNase I (0.1 mg/ml) under gentle shaking. After 30 min, the cell suspension was filtered through a 70-μm strainer. The cells were washed with fluorescence-activated cell sorting (FACS) buffer and blocked with CD16/32 antibody. Cells were then stained with designated antibodies panels: APC-Cy7-Anti-mouse CD45 Antibody (Clone: 30-F11, BioLegend), Pacific Blue-Anti-mouse CD8a Antibody (Clone: 53-6.7, BioLegend), FITC Rat Anti-mouse CD49b (Clone: DX5, BioLegend), BV786-Anti-CD3 Antibody (Clone: 17A2, BD Biosciences), APC-Anti-mouse CD107a Antibody (1D4B (RUO), BD Biosciences), PE-Cy7- Anti-mouse CD11c Antibody (Clone: HL3 (RUO), BD Biosciences), FITC-Anti-MHC-II Antibody (Clone: M5/114.15.2, eBioscience), BV605-Anti-mouse CD86 Antibody (Clone: GL1, BD Bioscience); Pacific Blue-Anti-mouse CD45 Antibody (Clone: 30-F11, BioLegend), APC-Cy7-Anti-mouse CD3 Antibody (Clone: 17A2, BD Bioscience), APC-Anti-mouse CD8a Antibody (Clone: 53-6.7(RUO), BD Biosciences), FITC Rat Anti-mouse CD49b (Clone: DX5, BioLegend), BV786-Anti-CD3 Antibody (Clone: 17A2, BD Biosciences), PE-Cy7- Anti-mouse CD11c Antibody (Clone: HL3 (RUO), FITC-Anti-MHC-II Antibody (Clone: M5/114.15.2, eBioscience), BV605-Anti-mouse/human CD11b (Clone: M1/70, BioLegend), PE-Anti-mouse F4/80 (Clone: BM8, BioLegend), APC-Anti-mouse CD206 (MMR, Clone: C068C2, BioLegend), PE-Cy7-Anti-mouse CD86 Antibody (Clone: GL1, BD Bioscience), FITC-Anti-mouse Ly6C Antibody (Clone: AL-21, BD Bioscience); BV421-Anti-mouse Ly6G Antibody (Clone: RB6-8C5, BioLegend); BV605-Anti-mouse CD45 Antibody (Clone: 30-F11, BioLegend), APC-Cy7-Anti-mouse/human CD11b (Clone: M1/70, BioLegend), PE-Anti-mouse F4/80 (Clone: BM8, BioLegend), APC-Anti-mouse CD206 (MMR, Clone: C068C2, BioLegend), PE-Cy7-Anti-mouse CD86 Antibody (Clone: GL1, BD Bioscience),

BV421-Anti-mouse Ly6G Antibody (Clone: RB6-8C5, BioLegend), FITC-Anti-mouse Ly6C Antibody (Clone: AL-21, BD Bioscience). Stained cells were analyzed by cytometry (MoFlo Astrios Cell Sorter, Beckman).

3.3.5. *In vivo* drug distribution analysis

To analyze in-vivo biodistribution of STING agonist, CDG-Dy547 (Biolag, Bremen, German) or CDG-Cy7 (Biolag, Bremen, German), was admixed with CDA (1:10, n/n) to prepare CDG-Dy547@CMP_{CDA} or CDG-Cy7@CMP_{CDA} following the same synthesis procedure as CMP_{CDA} mentioned above. Loading of CDG-Dy547 and CDG-Cy7 were quantified by absorbance at 550 nm or 750 nm. To quantify drug retention at the tumor site after intratumoral injection, CDG-Cy7 in free form or in CMP_{CDA} were injected into tumors. Mice were imaged by IVIS at different time points (0 h, 4 h, 8 h, 24 h), and the fluorescence signal of CDG-Cy7 in tumors was measured accordingly. Drug retention was calculated by normalizing the remaining fluorescence signal of CDG-Cy7 in tumor on the indicated time point by that of injected CDG-Cy7 at 0 h. To quantify the biodistribution of CMP after I.V. administration, CDG-Cy7 in free form or in CMP_{CDA} was injected I.V. Mice were euthanized 24 h post-injection, and the fluorescence intensity in major organs was measured accordingly. To quantify the biodistribution of Mn, tissues were microwave digested, and the amount of Mn was measured using ICP-MS by Michigan Elemental Analysis Laboratory.

To analyze drug distribution in TME, CDG-Dy547@CMP_{CDA} was injected via I.T. or I.V. routes. On the indicated time point, cells were harvested from TME and stained, as mentioned above. The amount of phagocytosed CDG-Dy547 in different cell

populations was analyzed by FACS. Cells were then stained with designated antibodies panels: Pacific Blue-anti-mouse CD45 antibody (Clone: 30-F11, BioLegend), BV605-anti-mouse CD3 antibody (Clone: 17A2, BioLegend), APC-anti-mouse CD11c antibody (Clone: N418, BioLegend), FITC-anti-MHC-II antibody (Clone: M5/114.15.2, eBioscience), BV605-anti-mouse/human CD11b (Clone: M1/70, BioLegend), APC-anti-mouse F4/80 (Clone: BM8, BioLegend), FITC-anti-mouse Ly6C antibody (Clone: AL-21, BD Bioscience). Stained cells were analyzed by cytometry (MoFlo Astrios Cell Sorter, Beckman).

Statistical analysis. The results are expressed as means ± SEM. A one-way or two-way ANOVA, followed by Bonferroni's multiple comparisons post hoc test, was used for testing differences among groups. Data were approximately normally distributed, and variance was similar between the groups. Experiments were repeated multiple times as independent experiments as indicated in the figure captions. Shown in the figure is a complete dataset from one representative, independent experiment. No samples were excluded from analysis. Statistical significance is indicated as *P < 0.05, **P < 0.01, ***P < 0.001, and ****P < 0.0001. GraphPad Prism 8.0 (GraphPad Software, La Jolla, CA) was used for statistical analyses.

3.4. Results & Discussion

3.4.1 CMP co-delivering Mn^{2+} and STING agonist amplifies STING activation.

Despite the promising results of Mn^{2+} and STING agonist combination, the free admixture of CDNs and Mn^{2+} has a number of limitations for clinical translation due to their poor metabolic stability, cellular permeability, as well as potential safety

concerns[166]. We sought to address these issues by developing a delivery system that can promote simultaneous cellular uptake of STING agonists and Mn^{2+}, achieving dose-sparing potency with minimal side effects (**Fig. 3-1**). We discovered that Mn^{2+} mixed with various CDNs in methanol, including CDA, CDG, and cGAMP, coordinated their self-assembly into coordination polymers ranging from nanometers to micrometers in diameter (**Fig. 3-2-1a**). We also observed the formation of coordination polymers when CDA was mixed in water with either Mn^{2+} or Zn^{2+} (**Fig. 3-2-2)**. Based on our Mn^{2+}-mediated potentiation of type-I IFN response and the fact that STING agonists in clinical trials are mainly derived from CDA[175], we focused on the CDA + Mn^{2+} combination for the remainder of studies. Isothermal titration calorimetry (ITC) analysis indicated that the CDA-Mn^{2+} interaction in methanol fitted a multiple-site binding model with a Ka1 of 9.367E8 M^{-1} and Ka2 of 1.206E7 M^{-1} while the interaction of CDA-Mn^{2+} interaction in water fitted an independent binding model with a K_D of 1 mM. However, in a physiological condition, CDA-Mn^{2+} interaction was unstable, leading to a rapid dissolution in PBS. Thus, to stabilize the CDA-Mn^{2+} coordination polymer, we added dioleoyl-*sn*-glycero-3-phosphoethanolamine-N-[histidine]$_{11}$ (DOPE-H11) (**Fig. 3-2-3**) that served as an additional coordination ligand and promoted the formation of hydrophobic core termed CDA-Mn@DOPE. To allow for aqueous suspension, we coated these hydrophobic CDA-Mn@DOPE core with an outer PEG-lipid layer by resuspension in a mixture solution of DOPC: cholesterol: DSPE-PEG5000 (4:1:1 molar ratio), followed by solvent evaporation and rehydration. The resulting CDA-Mn^{2+} particles, termed CMP_{CDA}, exhibited a uniform spherical morphology with an average hydrodynamic diameter of 118 ± 41 nm, a polydispersity index of 0.107, and a neutral surface charge (**Fig. 3-2-1**

c-d). CDA and Mn^{2+} were efficiently loaded into CMP_{CDA} with the loading efficiency of 39.6% and 25.3% and the loading capacity (wt/wt) of 13.2% and 6.72% for CDA and Mn^{2+}, respectively.

We employed CDG-Dy547, a fluorophore-labeled CDN, to track cellular uptake of STING agonists by BMDCs. Soluble CDG-Dy547 was poorly internalized by BMDCs even after 24 h (**Fig. 3-2-1 e-f**). In stark contrast, CMP_{CDA} carrying CDG-Dy547 exhibited significantly increased cellular uptake, with a 6.3-fold improvement observed after 4 h incubation ($P < 0.0001$, **Fig. 3-2-1 e**). Confocal microscopic images of BMDCs showed cytosolic localization of CMP with gradually reduced overlap with Lysotracker signal over time (**Fig. 3-2-1 f**), suggesting CMP-mediated trafficking of CDN to the cytosol where STING is expressed. CMP_{CDA} increased IFN-β secretion by BMDCs by > 20-fold, compared with free CDA, Mn^2, or their admixture ($P < 0.0001$, **Fig. 3-2-1 g**). CMP-mediated co-delivery of CDA and Mn^{2+} was crucial for robust STING activation as Mn^{2+}-particles alone or Mn^{2+}-particles admixed with free CDA induced a weak IFN-β response (**Fig. 3-2-1 g**). We also observed similar responses with TNF-α secretion (**Fig. 3-2-1 h**). Taken together, CMP significantly augmented cellular uptake of CDA, STING activation, and IFN-β response *in vitro*.

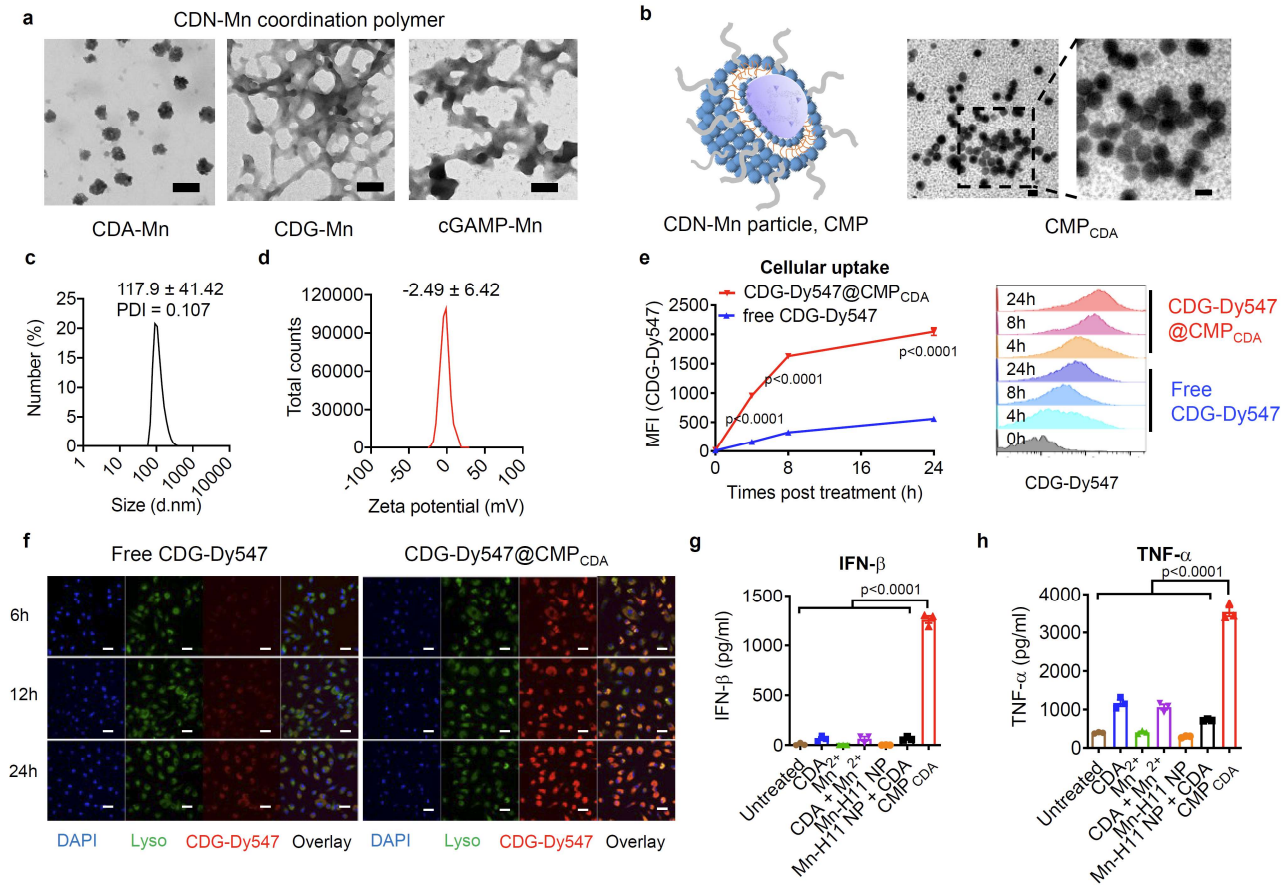

Figure 3-2-1. CMP co-delivering Mn^{2+} and STING agonist amplifies STING activation.

a) Self-assembly behavior of CDNs and Mn^{2+}. TEM images of CDN-Mn coordination polymers formed by mixing CDA, CDG, or cGAMP with Mn^{2+} (10:1, n/n) for 1h. Scale bars = 100 nm. **b)** TEM images showed homogenous CMP_{CDA} formed by coating CDA-Mn coordination polymers with a PEGylated lipid layer. Scale bar = 100 nm. **c)** Dynamic light scattering and **d)** zeta potential analyses of CMP_{CDA}. **e-f)** CMP_{CDA} increased cellular uptake of STING agonist. BMDCs were incubated with free CDG-Dy547 or CDG-Dy547@CMP_{CDA} for 6, 12, or 24 h, followed by analyses by **e)** flow cytometry and **f)** confocal microscopy. **g-h)** CMP_{CDA} increased STING activation and cytokine production**.** BMDCs were treated for 24h with 2.5 μM CDA and/or 15.6 μM Mn^{2+} in free form, blank nanoparticle without CDA (Mn-H11 NP), or CMP_{CDA}, followed by quantification of **g)** IFN-β and **h)** TNF-α secretion by ELISA. Data represent mean ± SEM, from a representative experiment from 2 independent experiments with n = 3 (e, g-h) biologically independent samples. ****P < 0.0001, analyzed by (g-h) one-way ANOVA or (e) two-way ANOVA with Bonferroni's multiple comparisons tests.

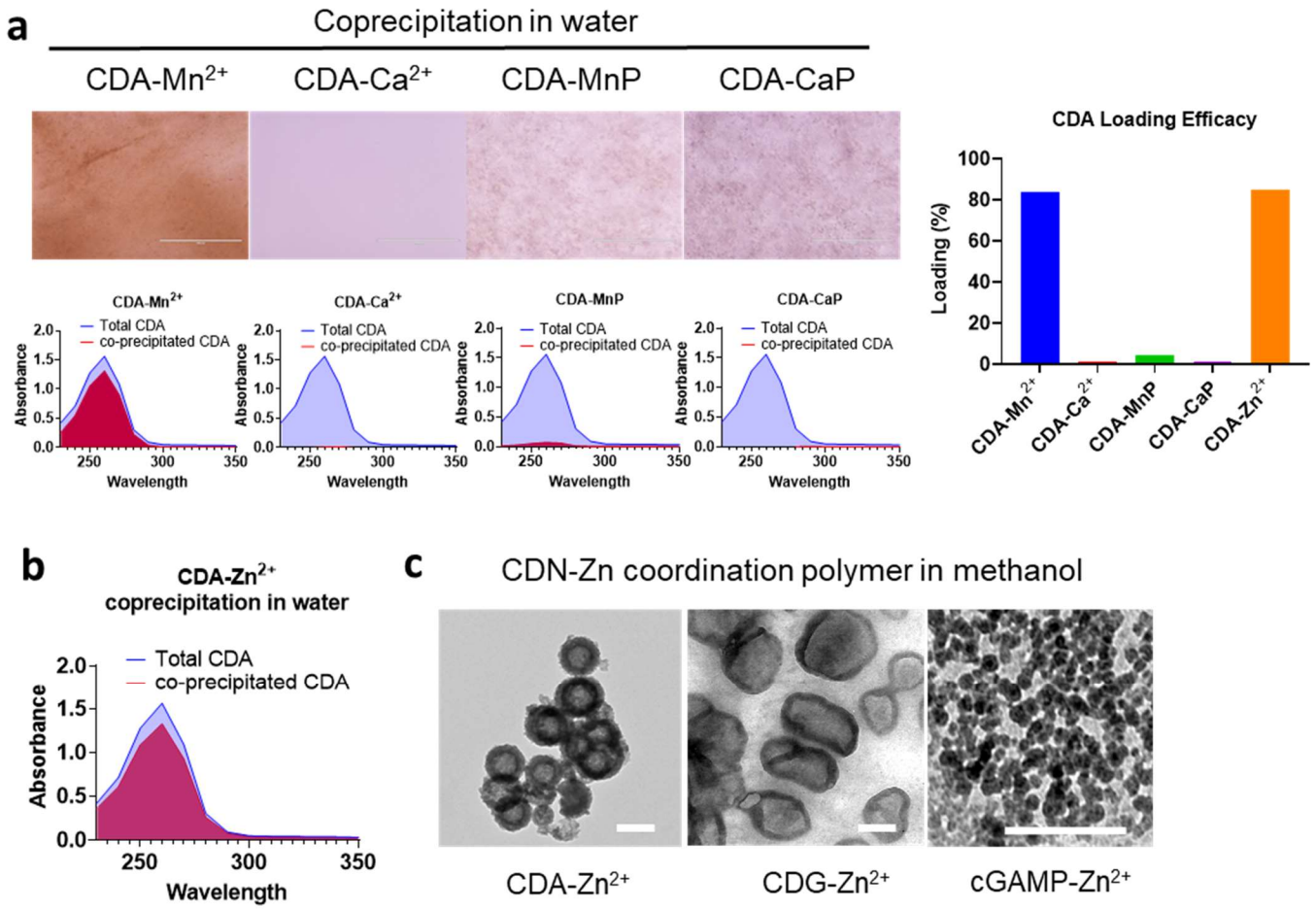

Figure 3-2-2. Effective coordination of CDNs with Mn^{2+} or Zn^{2+}, but not with Ca^{2+}, Mn-phosphate (MnP) or Ca-phosphate (CaP). a, Mn^{2+} coordinated with CDA and formed visible precipitation under microscope with high drug loading efficacy. In contrast, Ca^{2+}, Mn-Phosphate or Ca-Phosphate failed to coordinate or load CDA. 2 mg/ml CDA were mixed with Mn^{2+} (10:1, n/n) or Ca^{2+} (10:1, n/n) in water while stirring. In parallel, mixed solution of 2 mg/ml CDA and PO_4^{3+} (10:1, n/n) were mixed Mn^{2+} (10:1, n/n) or Ca^{2+} (10:1, n/n) in water while stirring. Total CDA absorbance spectra were measured by a multi-mode microplate reader (BioTek, Synergy Neo2). Shown are the CDA loading efficiencies in the resulting structures. **b,** Zn^{2+} coordinated with CDA and formed visible precipitation under microscope with high drug loading efficacy. 2 mg/ml CDA were mixed with Zn^{2+} (10:1, n/n) in water while stirring. Total CDA absorbance spectra were measured by a multi-mode microplate reader (BioTek, Synergy Neo2). **c,** TEM images of CDN-Zn

coordination polymers (CP) formed by mixing CDA, CDG, or cGAMP with Mn^{2+} (10:1, n/n) in methanol while stirring. Scale bars = 100 nm. Shown are representative data from two independent experiments with similar results (a-c).

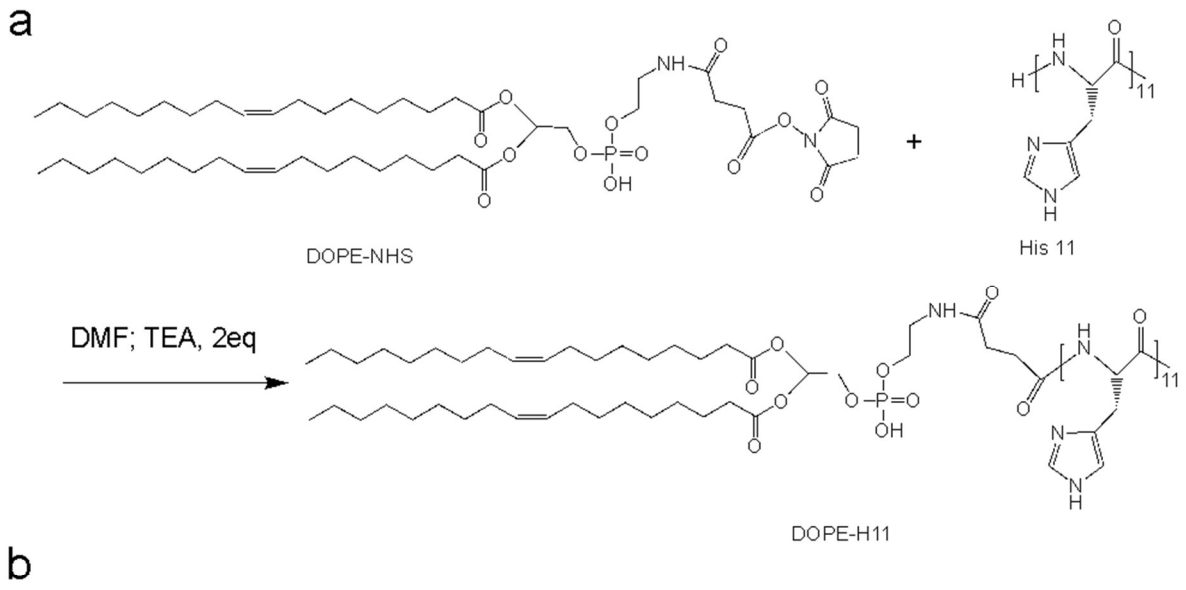

Figure 3-2-3. a) Synthesis route of DOPE-histidine11 (DOPE-H11). **b)** GPC chromatogram of DOPE-H11.

3.4.2 Local intratumoral administration of CMP_{CDA} eliminates established tumors

Next, we evaluated the therapeutic efficacy of CMP *in vivo*. CT26 tumor-bearing BALB/c mice were treated on days 9, 12, and 15 by I.T. administration of CDA and Mn^{2+} in CMP or soluble formulation (**Fig. 3-3-1a**). Whereas 20 μg CDA and 17.5 μg Mn^{2+} were used in **Fig. 2-3-2**, here we decreased their doses to 5 μg CDA and 2.5 μg Mn^{2+} to examine the dose-sparing effect of CMP_{CDA}. Intratumoral injection of CMP_{CDA} led to significantly improved immune activation, as shown by elevated levels of IFN-β, TNF-α, CXCL-10, and CCL-2, compared with free CDA + Mn^{2+} admixture (**Fig. 3-3-1b**). CMP_{CDA} treatment also induced robust AH1-specific CD8+ T cell response in the systemic circulation (**Fig. 3-3-1c, 3-3-2**). Importantly, CMP_{CDA} exerted potent anti-tumor efficacy and eradicated 78% of established tumors, compared with 30% response rate for the soluble CDA + Mn^{2+} group ($P < 0.05$, **Fig. 3-3-1d-e**). In addition, 100% of survivors from the CMP_{CDA} treatment group were resistant to the CT26 tumor re-challenge performed on day 145 (**Fig. 3-3-1f**). Remarkably, even with a minute dose of 1 μg CDA + 0.5 μg Mn^{2+}, CMP_{CDA} induced strong immune activation and eliminated established tumors in 40% of mice, compared with 0% response rate for the soluble CDA + Mn^{2+} group (**Fig. 3-3-1g**, **3-3-3**). We also tested the effect of intratumoral treatment of CMP on untreated, distal tumors in a two-tumor model (**Fig. 3-3-4**). As reported previously for free STING agonist[175], while high dose of 20 μg CMP was better at inhibiting the primary tumor growth, lower doses of CMP (either 1 μg or 5 μg CDA) exerted robust abscopal effect against distal tumors, significantly outperforming free CDA injections, without any overt change in the body weight of animals.

Next, we sought to delineate how CMP potentiates STING activation. First, we measured the retention and distribution of STING agonists delivered via CMP_{CDA} in the TME. Within 24 h of intratumoral administration, free CDG-Cy7 (fluorophore-tagged CDN) was rapidly cleared, with only 2.9 ± 2.7% of injected dose retained in the TME (**Fig. 3-3-1 h**). In contrast, CMP_{CDA} group still retained 38.2 ± 6.6% of injected dose in the TME after 24 h, representing a 13.4-fold increase, compared with free CDG-Cy7 ($P < 0.05$, **Fig. 3-3-1 h**). Flow cytometric analyses of the tumor tissues showed that CDG-Dy547@CMP_{CDA} significantly improved cellular uptake of CDG by CD11c+ DCs, F4/80+ macrophages, and Ly6C+ myeloid-derived suppressor cells (MDSCs) (**Fig. 3-3-1 i, Figure 3-3-5, 3-3-6**). On the other hand, we observed minimal uptake of CDG-Dy547 among CD45- tumor cells and CD3+ T-cells. We also analyzed changes in the activation status of immune cells after CMP_{CDA} treatment. Compared with free CDA with or without Mn^{2+}, CMP_{CDA} treatment promoted activation of intratumoral NK cells (**Fig. 3-3-1 j, 3-3-7**) and upregulation of CD86, a maturation marker, on DCs in tumor-draining lymph nodes (TDLNs) (**Fig. 3-3-1 k**). These results suggest that CMP_{CDA} efficiently modulated the TME, in part by promoting tissue retention of STING agonists and their uptake by local immune cells, leading to Mn^{2+}-mediated potentiation of STING agonists and activation of anti-tumor immune responses.

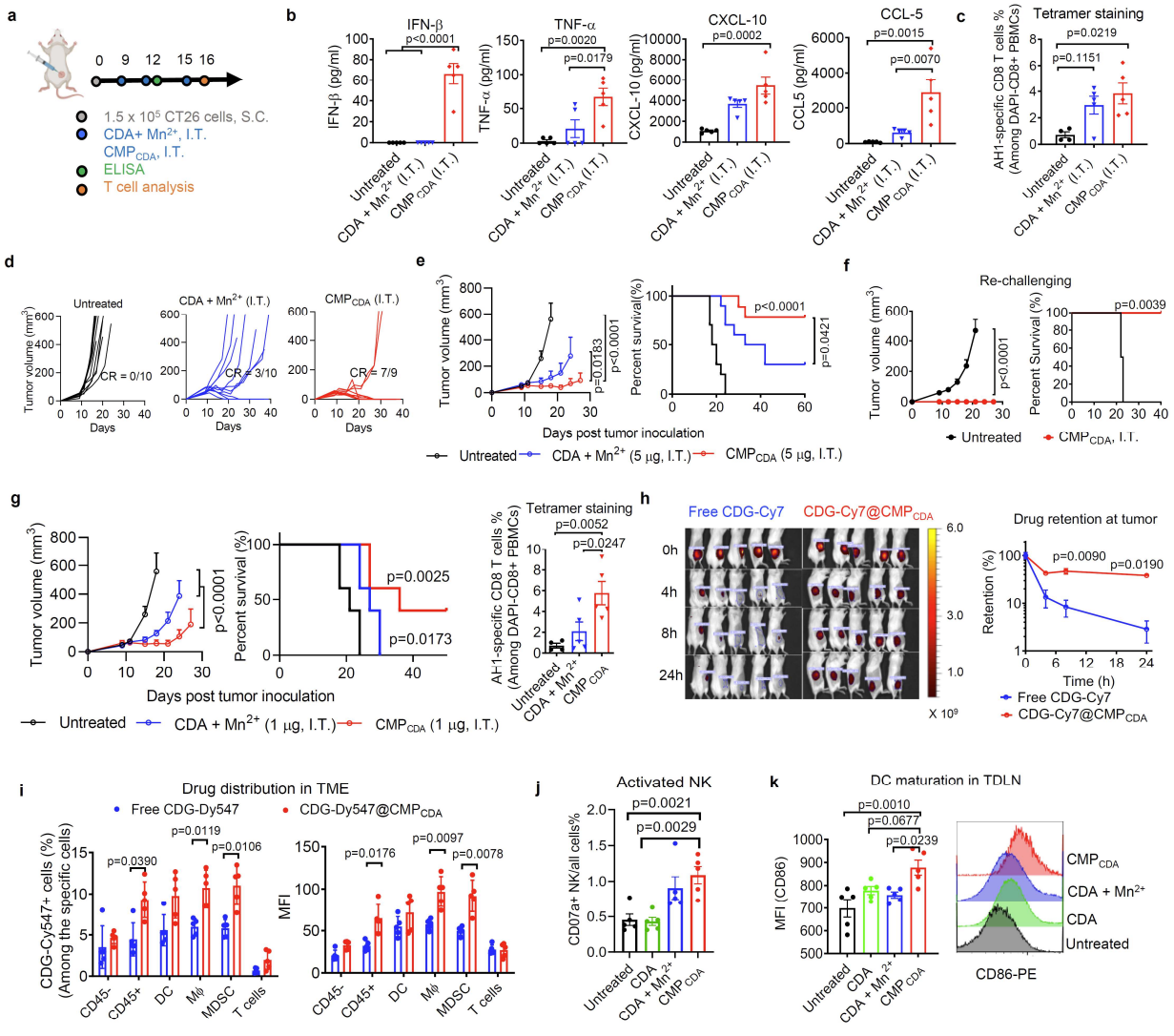

Figure 3-3-1. Local intratumoral administration of CMP_{CDA} eliminates established tumors. a-f) Therapeutic effects of CMP_{CDA} after intratumoral (IT) administration. **a)** BALB/c mice were inoculated at S.C. flank with 1.5 x 10^5 CT26 tumor cells. CDA+ Mn^{2+} or CMP_{CDA} containing 5 μg CDA and 2.5 μg Mn^{2+} were injected I.T. on days 9, 12, and 15. **b)** Serum cytokines were measured by ELISA at 6 h post the second dose. **c)** Antigen-specific T cell response in PBMCs was analyzed by AH1 tetramer staining on day 16. **d-e)** Tumor growth and animal survival were monitored over time. **f)** Survivors were re-challenged with CT26 tumor cells on day 145. **g)** BALB/c mice were inoculated with 1.5 x 10^5 CT26 tumor cells at the S.C. flank and treated by I.T. administration of CDA+ Mn^{2+} or CMP_{CDA} containing 1 μg CDA and 0.5 μg Mn^{2+} on day 9, 12, and 15. Tumor growth and animal survival were monitored, and antigen-specific T cell response was analyzed on

day 16. **h)** CDG-Cy7 either in free or CMP_{CDA} form was administrated I.T., and retention of STING agonist retention within the TME was quantified by *in vivo* imaging. **i)** CDG-Dy547 either in free or CMP_{CDA} form was administrated I.T., and after 6 h, CDG-Dy547 signal among immune cells within the TME was analyzed by flow cytometry. **j-k)** CT26 tumor-bearing mice were treated as in **g)** and analyzed on day 16 by flow cytometry for the frequency of CD107a+ NK cells within tumors **(j)** and CD86 expression on DCs in tumor-draining lymph nodes (TDLNs) **(k)**. Data represent mean ± SEM, from a representative experiment from 2 independent experiments with n = 4-5 (b-c, f-k), and n = 9-10 (d-e). $^{*}P < 0.05$, $^{**}P < 0.01$, $^{***}P < 0.001$, $^{****}P < 0.0001$, analyzed by (b-c, g, j-k) one-way ANOVA or (e-h) two-way ANOVA with Bonferroni's multiple comparisons test, or (i) multiple t-test with Bonferroni correction, or (e-g) log-rank (Mantel-Cox) test. * and # in (e) denote the significance relative to Untreated and CDA+ Mn^{2+} groups, respectively.

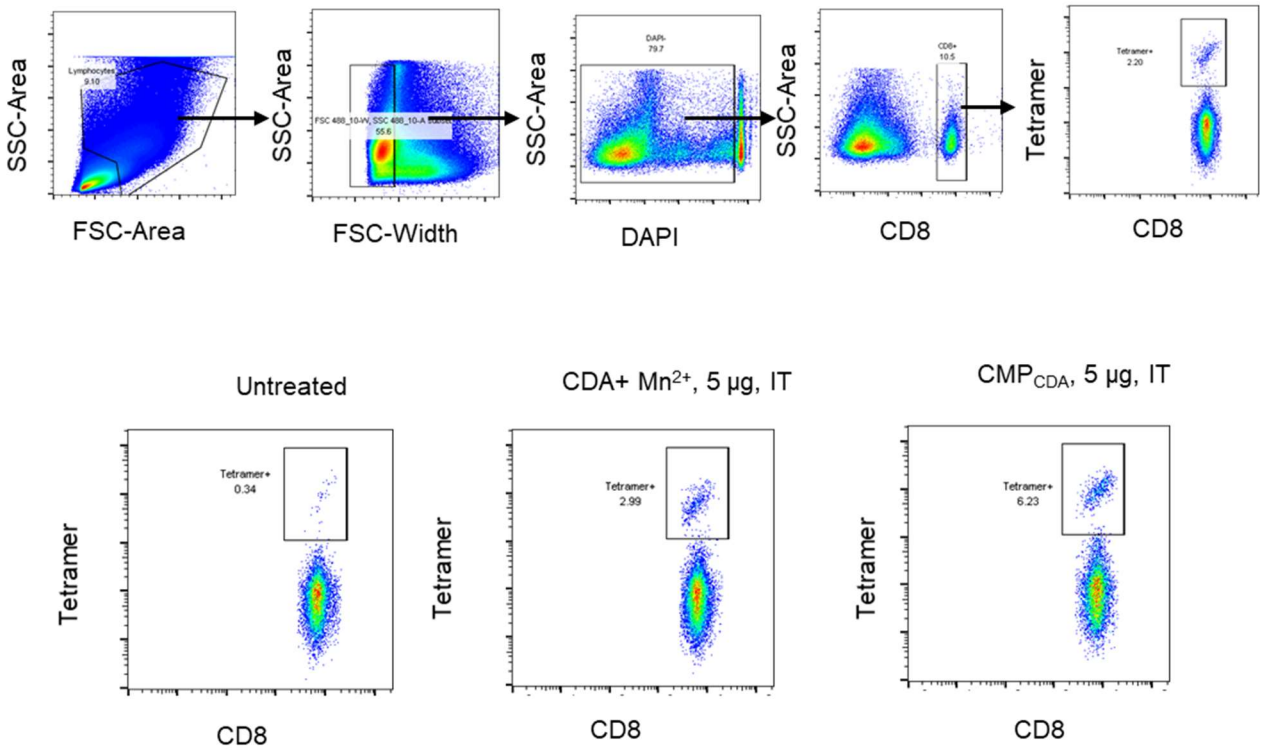

Figure 3-3-2. Gating strategy for tetramer+ CD8 T-cells and representative scatter plots related to Fig. 3-3-1c.

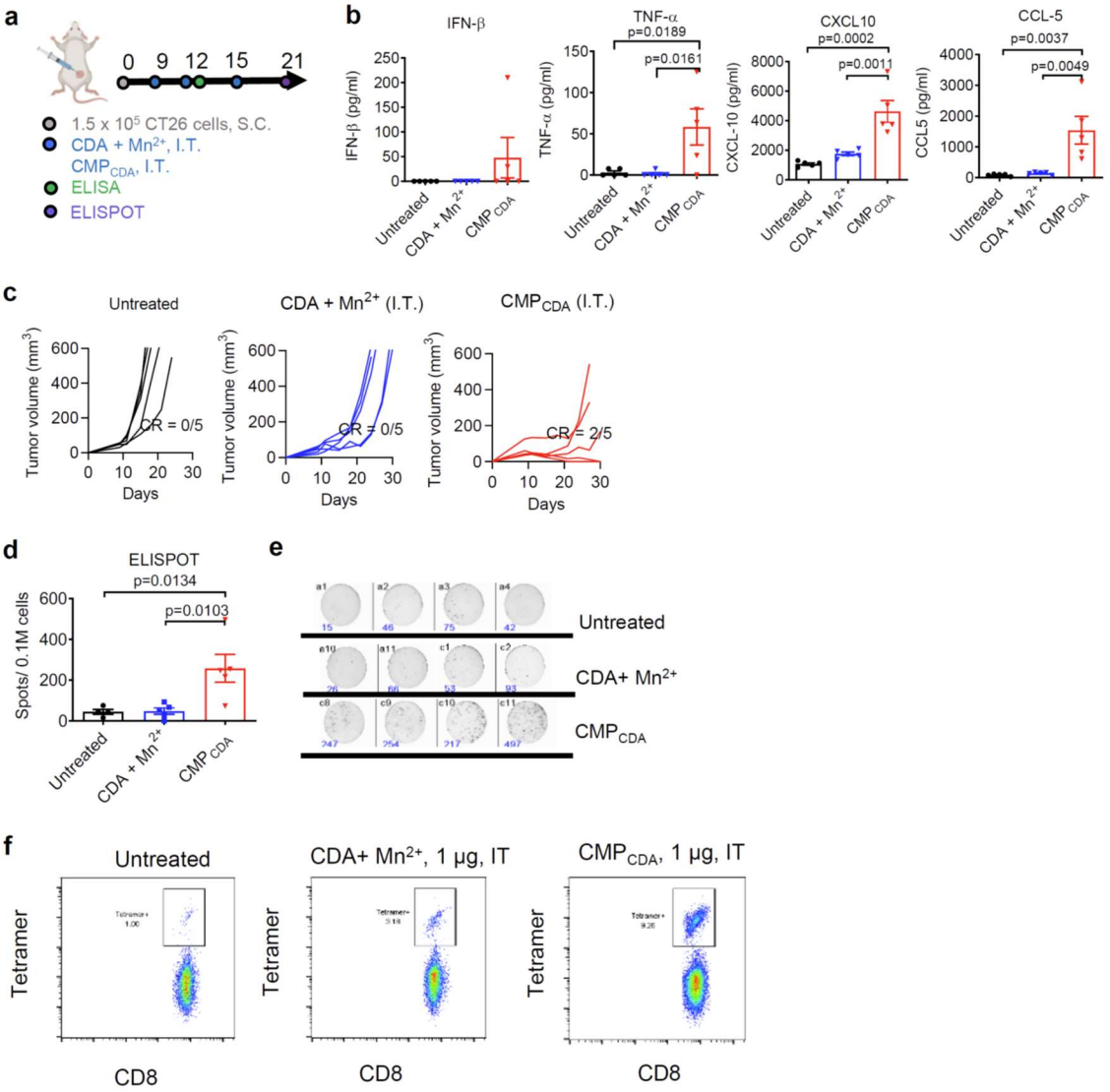

Figure 3-3-3. Local intratumoral administration of low-dose CMP_{CDA} eliminates established tumors. a) BALB/c mice were inoculated at s.c. flank with 1.5 x 10^5 CT26 tumor cells. CDA+ Mn^{2+} or CMP_{CDA} containing 1 µg CDA and 0.5 µg Mn^{2+} were injected I.T. on days 9, 12, and 15. **b)** Serum cytokines were measured by ELISA at 6 h post the second dose. **c)** Tumor growth was monitored over time. **d-e)** Antigen-specific T cell response in PBMCs was analyzed by AH1-specific IFN-γ ELISPOT assay on day 21. **f)** Representative scatter plots for tetramer+ CD8 T-cells related to **Fig. 3-3-1**. Data represent mean ± SEM, from a representative experiment from 2 independent experiments with *n* = 5 (b-d). Data were analyzed by one-way ANOVA with Bonferroni's multiple comparisons test.

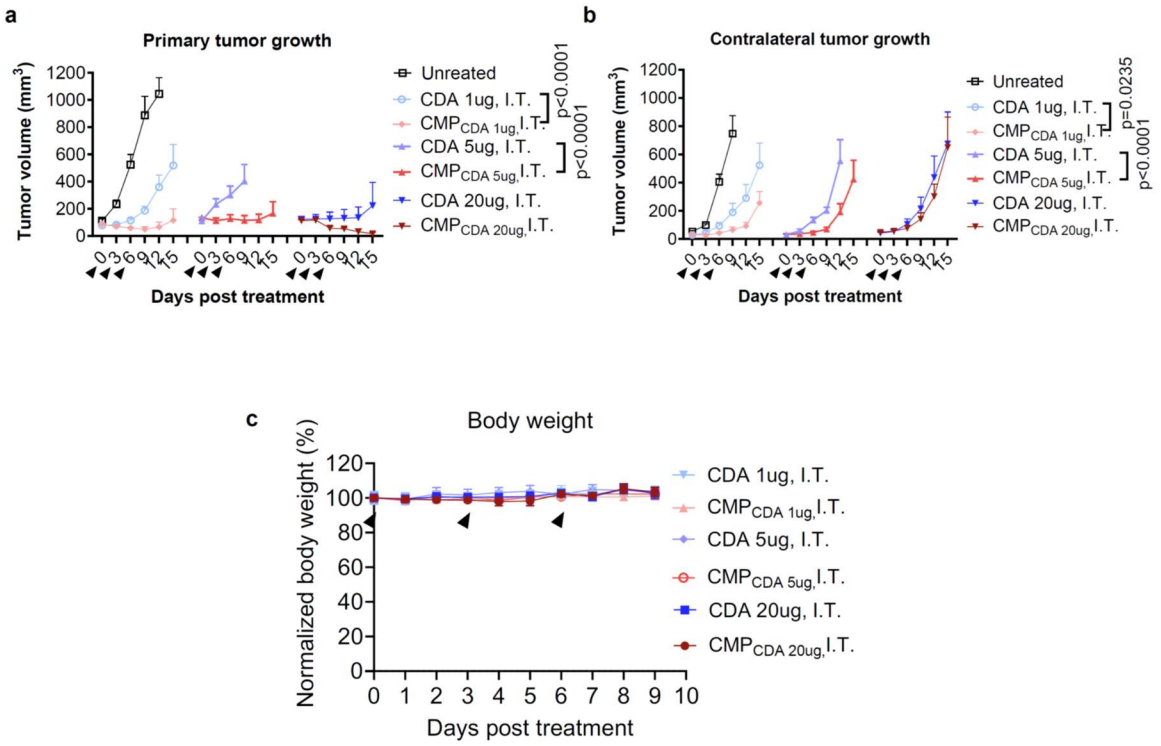

Figure 3-3-4. Therapeutic effect of CMP in CT26 two-tumor model. a-c, Balb/c mice were inoculated subcutaneously with 3 x 10^5 CT26 tumor cells on the right flank and 1 x 10^5 CT26 tumor cells on the left flank. 3 doses of CDA or CMP_{CDA} containing 1, 5, 20 μg CDA were injected I.T. on the right flank in 3-day intervals when the right tumor size achieve ~100 mm^3. Tumor growth curve of the primary right tumor **(a)** and left distal tumor **(b)** were measured every three days. Body weight change **(c)** is monitored daily. The data show mean ± SEM, with *n* = 5 (a-c). Data were analyzed by two-way ANOVA (a, b) with Bonferroni multiple comparisons post-test.

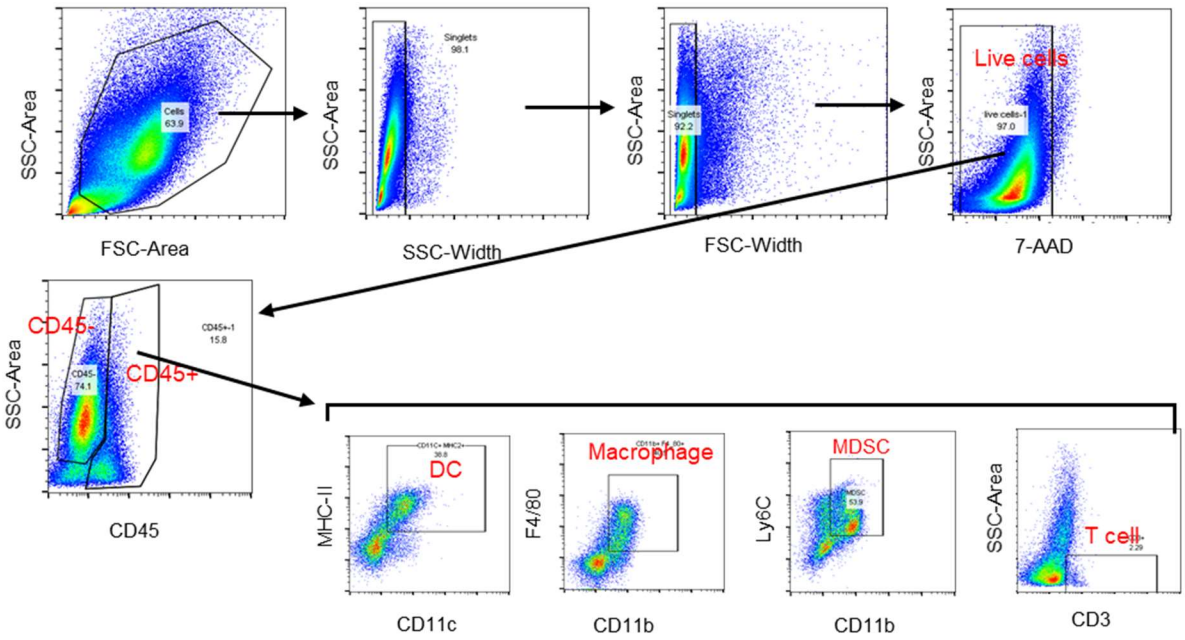

Figure 3-3-5. Gating strategy for analyzing cellular uptake of CDN in TME related to Fig 3-3-1 i, 3-4-1 h.

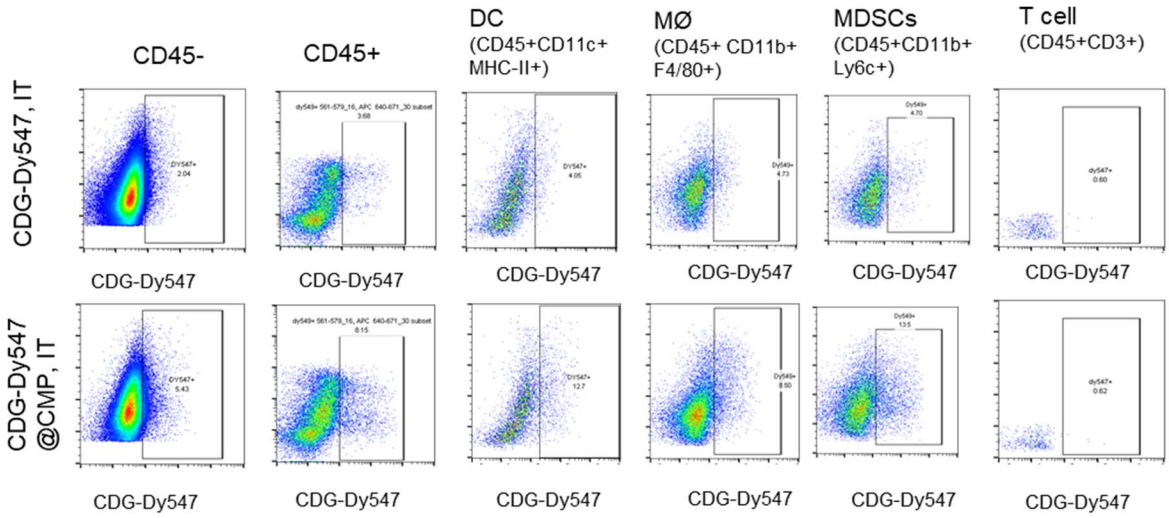

Figure 3-3-6. Representative scatter plots of CDN distribution in TME after IT injections related to Fig 3-3-1 i.

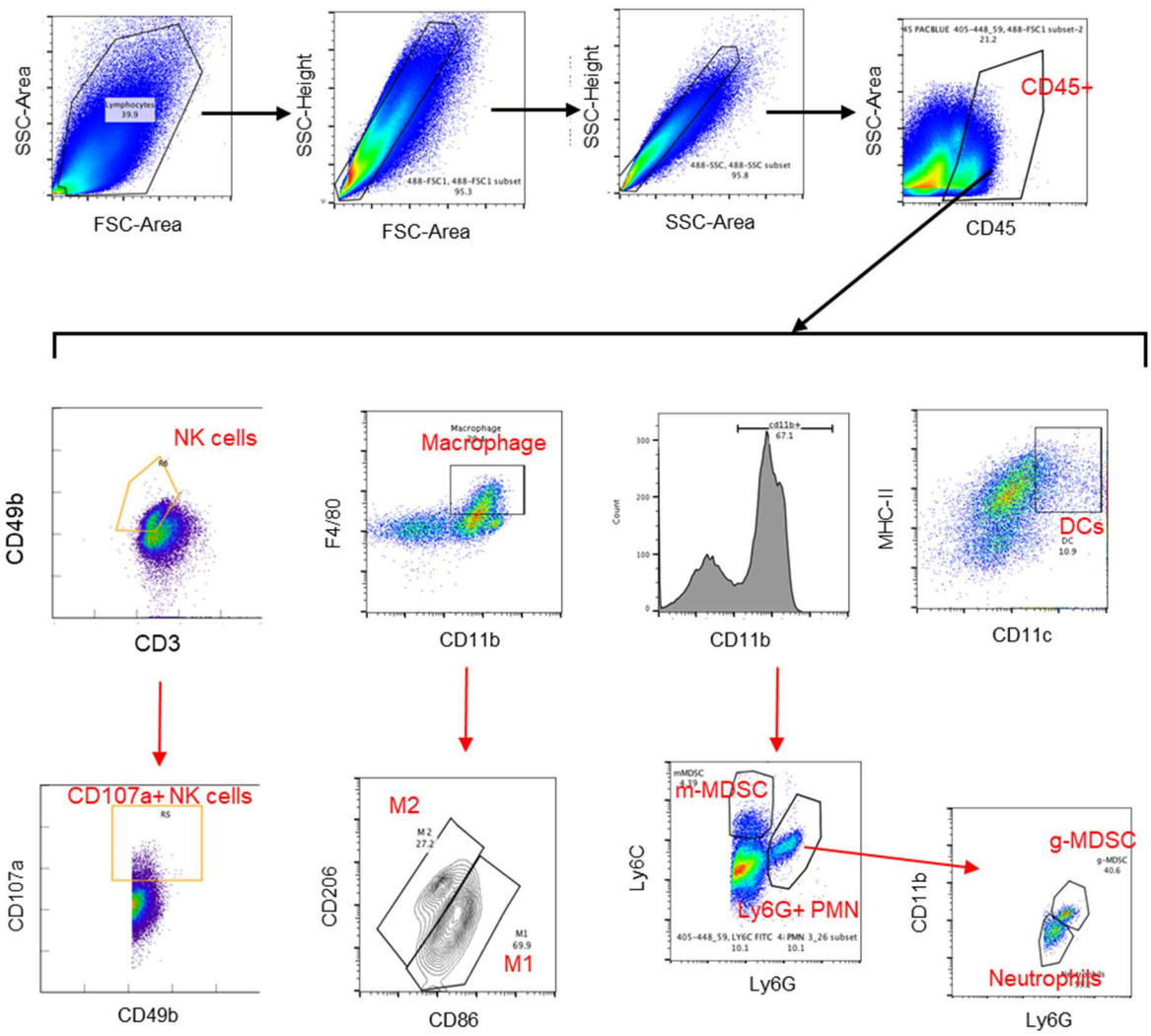

Figure 3-3-7. Flow cytometry gating strategy for analysis of NK cells, M1-like and M2-like macrophages, DCs, and MDSCs.

3.4.3 Systemic I.V. administration of CMP_{CDA} eliminates established tumors

Due to rapid enzymatic degradation and poor drug-like properties, most STING agonists in clinical trials are administered directly into tumors; however, I.T. route of administration is not applicable for metastatic tumors, thus underscoring a major unmet need. Here, we sought to evaluate the therapeutic effect of CMP after I.V. administration. CT26 tumor-bearing BABL/c mice were treated with I.V. administration of 20 μg CDA and 10 μg Mn^{2+} either in CMP_{CDA} or soluble form on days 9, 12, and 15. Compared with the soluble control group, CMP_{CDA} promoted accumulation of Mn^{2+} and CDN in tumor tissues and significantly increased the serum levels of IFN-β, TNF-α, CXCL-9, and CXCL-10 (**Fig. 3-4-1b**), demonstrating robust immune activation. As shown by IFN-y ELISPOT assay performed on PBMCs, I.V. treatment with CMP_{CDA} significantly enhanced AH1-specific CD8+ T cell response, compared with the CDA + Mn^{2+} admixture control group (**Fig. 3-4-1c**). Importantly, CMP_{CDA} administered I.V. significantly decreased CT26 tumor growth and eliminated established tumors in 50% of mice ($P < 0.0001$, **Fig. 3-4-1 d-f**), whereas soluble CDA + Mn^{2+} treatment had 0% response rate. Notably, even increasing the dose of free CDA I.V. therapy to 100 μg could not control the growth of CT26 tumors, whereas 20 μg CMP_{CDA} I.V. therapy effectively regressed established tumors ($P < 0.0001$, **Fig. 3-4-2**). Flow cytometric analysis performed on day 23 showed that CMP_{CDA} I.V. therapy significantly expanded $CD8^+$ T cell subsets with CD44+CD62L+ central memory and CD44+CD62L- effector memory phenotypes (**Fig. 3-4-3**). When the survivors from the CMP_{CDA} treatment group were subjected to CT26 tumor re-challenge on day 105, 80% of mice were resistant to CT26 tumor growth (**Fig. 3-4-1g**). We also measured drug distribution in the TME and major organs. CMP_{CDA} I.V. therapy significantly increased the

drug uptake by intratumoral $CD45^+$ immune cells, especially F4/80+ macrophages and Ly6C+ MDSCs (**Fig. 3-4-1h, Fig. 3-4-4**). TME analysis revealed that CMP_{CDA} I.V. therapy significantly reduced intratumoral MDSCs and promoted M2-to-M1 re-polarization of intratumoral macrophages (**Fig. 3-4-1 i-j**). CMP_{CDA} I.V. therapy also induced robust DC maturation in TDLNs (**Fig. 3-4-1 k**). Lastly, we also validated the therapeutic effects of CMP_{CDA} I.V. therapy using a second tumor model. C57BL/6 mice bearing B16F10 melanoma were treated I.V. with CMP_{CDA} or CDA + Mn^{2+} mixture. CMP_{CDA} I.V. therapy efficiently inhibited B16F10 tumor growth with significantly enhanced therapeutic efficacy, compared with CDA + Mn^{2+} mixture ($P < 0.001$, **Fig. 3-4-1 l-n, 3-4-5**). Altogether, these results suggest that CMP_{CDA} induced conversion of “cold” tumor to “hot” tumor.

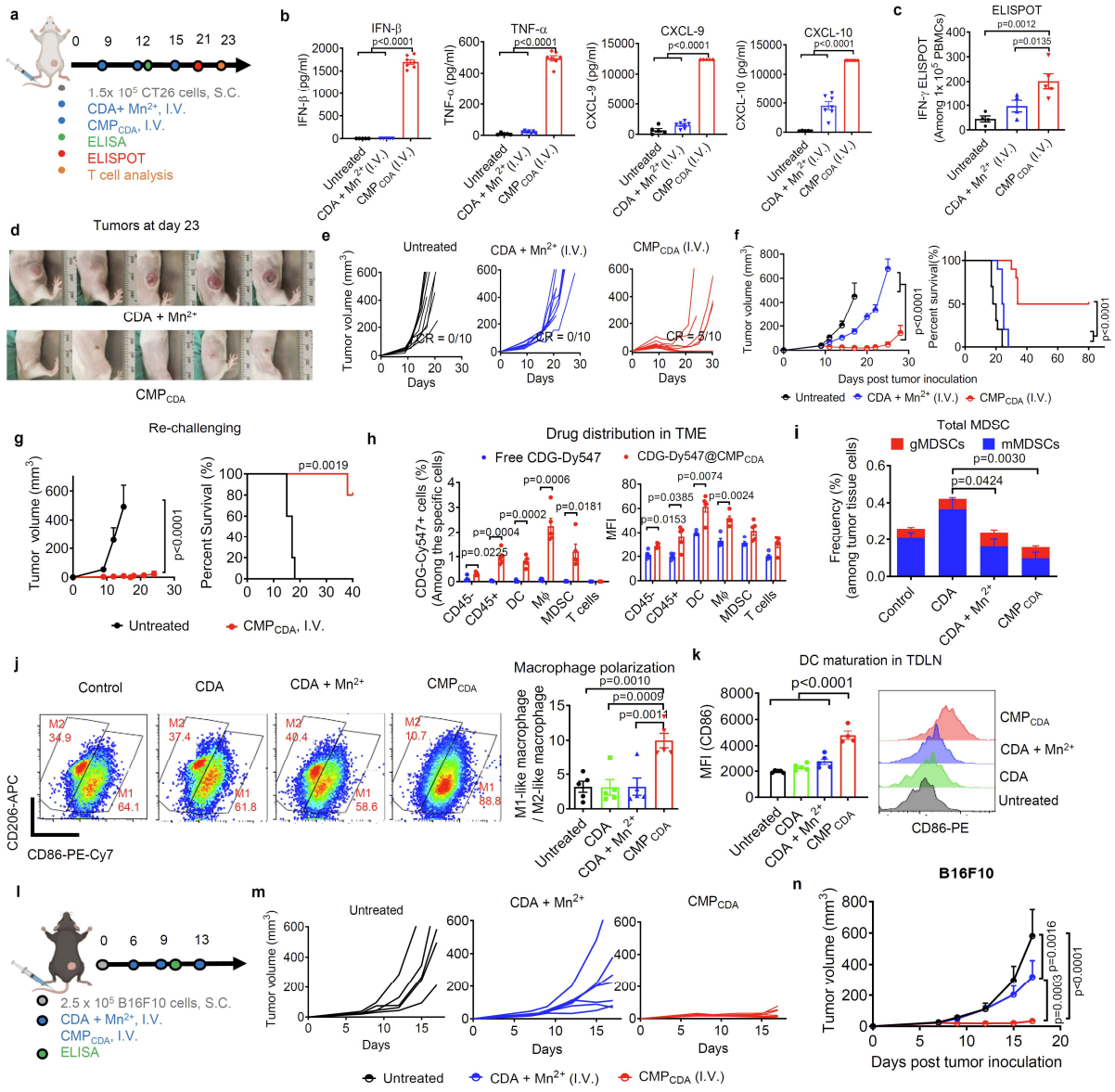

Figure 3-4-1. Systemic I.V. administration of CMP_{CDA} eliminates established tumors. **a-i)** Therapeutic effects of CMP_{CDA} on CT26 tumors after I.V. administration. **a)** BALB/c mice were inoculated at S.C. flank with 1.5 x 10^5 CT26 tumor cells. CDA+ Mn^{2+} or CMP_{CDA} containing 20 μg CDA and 10 μg Mn^{2+} were injected I.V. on days 9, 12, and 15. **b)** Serum cytokines were measured by ELISA at 6 h post the second dose. **c)** Antigen-specific T cell response was analyzed on day 21 by re-stimulating PBMCs with AH1 peptide, followed by IFN-γ ELISPOT assay. **d-f)** Tumor growth **(d-e)** and animal survival **(f)** were monitored over time. **g)** Survivors re-challenged with CT26 tumor cells on day 145 were monitored for tumor growth. **h)** CDG-Dy547 either in free or CMP_{CDA} form was administrated I.V., and after 24 h, CDG-Dy547 signal among immune cells within the TME was analyzed by flow cytometry. **i-k)** CT26 tumor-bearing mice were treated as in **a)** and analyzed on day 17 by flow cytometry for the frequency of granulocytic and monocytic

MDSCs **(i),** M1-like and M2-like macrophages **(j)** within the TME and CD86 expression on DCs in TDLNs **(k)**. **l-n)** Therapeutic effects of CMP_{CDA} administered I.V. on B16F10 tumors. C57BL/6 mice were inoculated at S.C. flank with 2.5 x 10^5 B16F10 tumor cells. CDA+ Mn^{2+} or CMP_{CDA} containing 20 μg CDA and 10 μg Mn^{2+} were injected I.V. on days 6, 9, and 13 **(l)**, and tumor growth was monitored over time **(o-p)**. Data represent mean ± SEM, from a representative experiment from 2 independent experiments with *n* = 5 (b-c, g-k), *n* = 5-7 (m-n), and *n* = 10 (e-f). **P* < 0.05, ***P* < 0.01, ****P* < 0.001, *****P* < 0.0001, analyzed by (b, c, j, k) one-way ANOVA or (f, g, i, n) two-way ANOVA with Bonferroni's multiple comparisons test, or (h) multiple t-test with Bonferroni correction, or (f, g) log-rank (Mantel-Cox) test.

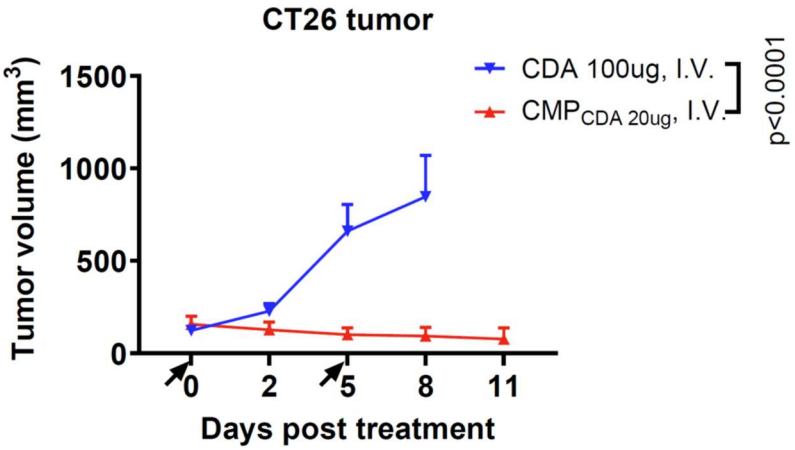

Figure 3-4-2. Therapeutic efficacy of CMP_{CDA} 20 μg versus 100 μg CDA. BALB/c mice were inoculated subcutaneously with 1 x 10^5 CT26 tumor cells on the right flank. When the tumor size achieved ~100 mm^3, 100 μg CDA or $CMP_{CDA\ 20\mu g}$ were injected I.V. on day 0 and 5 post the initial treatment. The data show mean ± SEM, with n=4. Data were analyzed by two-way ANOVA with Bonferroni multiple comparisons post-test.

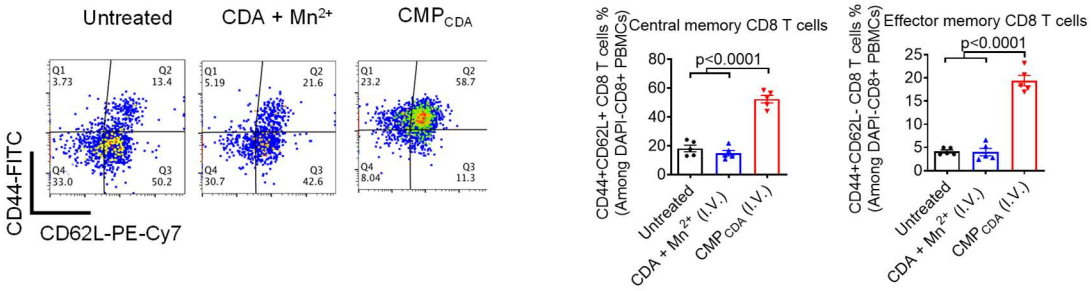

Figure 3-4-3. Expansion of memory CD8 T cells among PBMCs after I.V. treatment of CMP. BALB/c mice were inoculated at s.c. flank with 1.5 x 10^5 CT26 tumor cells. CDA+ Mn^{2+} or CMP_{CDA} containing 20 μg CDA and 10 μg Mn^{2+} were injected I.V. on days 9, 12,

and 15. CD8+ T cells among PBMCs were analyzed by flow cytometry for memory phenotype on day 23. The data show mean ± SEM, with n=5 biologically independent samples. Data were analyzed by one-way ANOVA with Bonferroni multiple comparisons post-test.

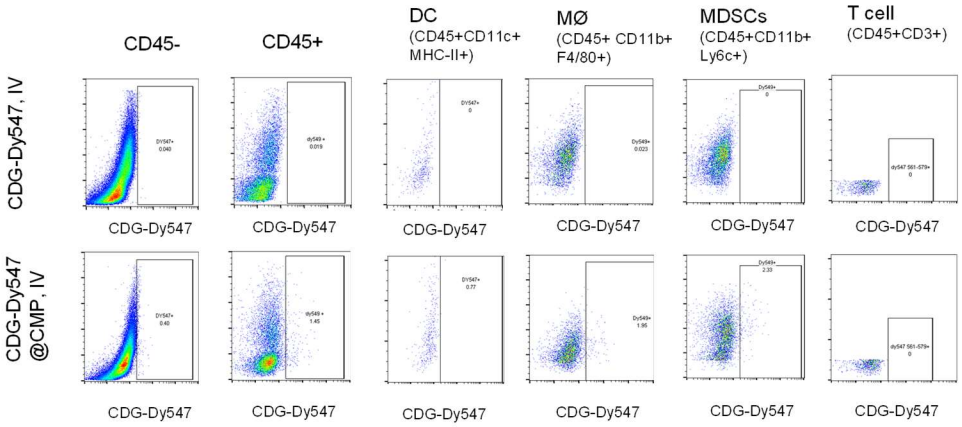

Figure 3-4-4. Representative scatter plots of CDN distribution in TME after IV injections related to Fig. 3-4-1h.

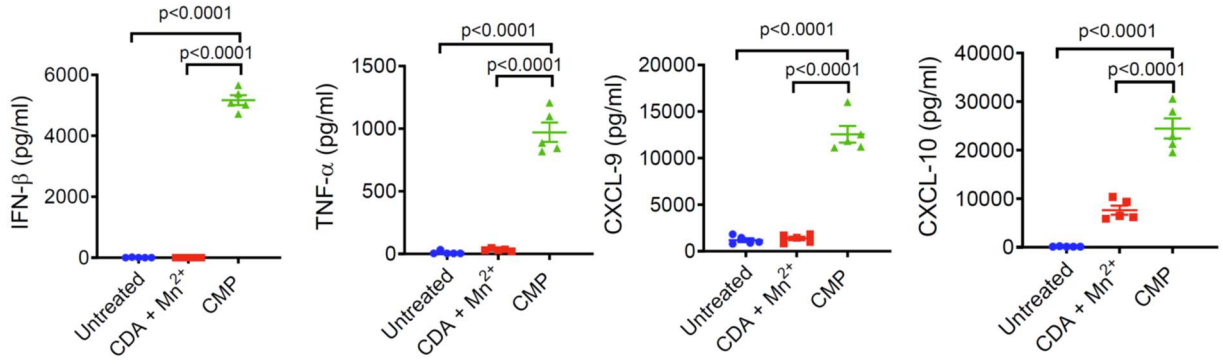

Figure 3-4-5. B16F10 tumor-bearing mice were treated as in **Fig. 3-4-1 n**, and serum cytokines were measured by ELISA at 6 h post the second dose. The data show mean ± SEM, with n=5 biological independent samples. Data were analyzed by one-way ANOVA with Bonferroni multiple comparisons post-test.

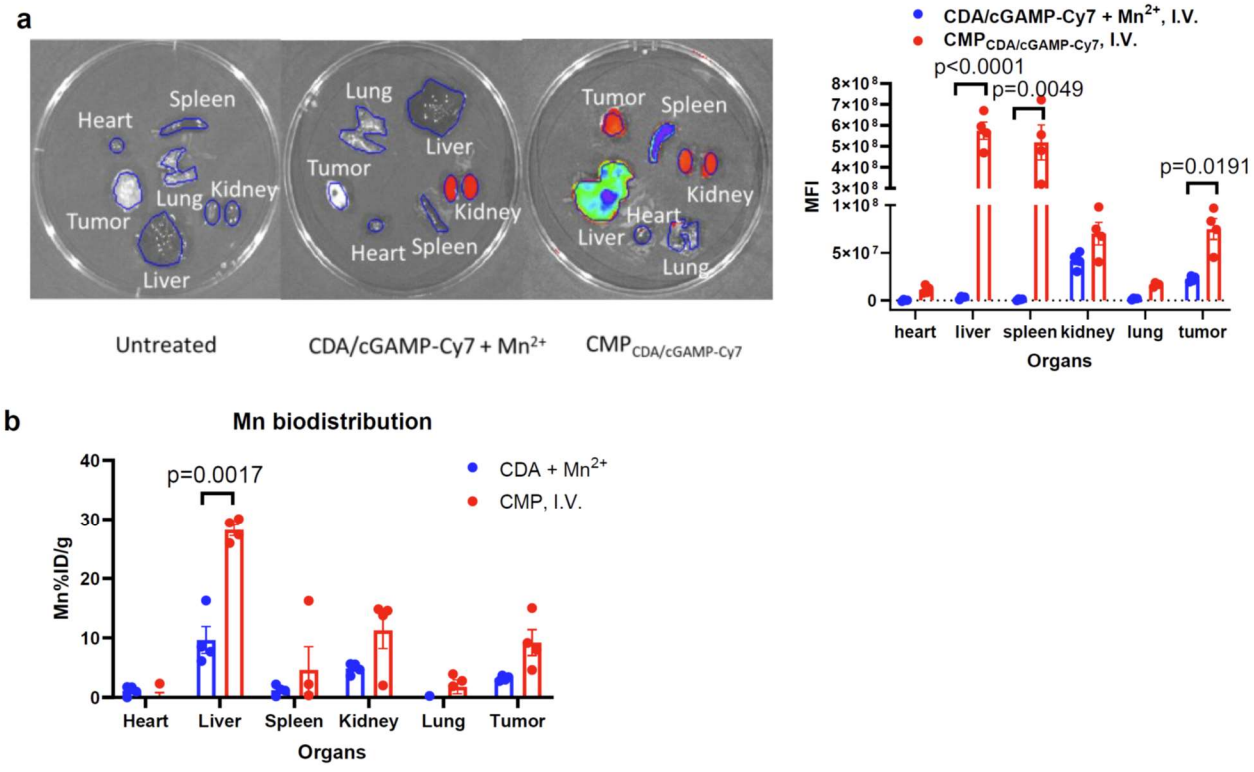

Figure 3-4-6. Biodistribution of CMP versus CDN + Mn^{2+} after 24 hr of I.V. administration. a, CT26 tumor-bearing mice were injected with $CMP_{CDA/cGAMP-Cy7}$ or free CDA/cGAMP-Cy7 (10:1, n/n) + Mn^{2+}. After 24 hours, mice were euthanized and subjected ex-vivo imaging of major organs using IVIS. Mean fluorescence intensity of each organ was plotted. **b,** Biodistribution of Mn in major organs at 24 h after I.V. injection of free CDA + Mn^{2+} or CMP as measured by ICP-MS. Data represent mean ± SEM (*n* = 4 biologically independent samples) and were analyzed by two-tailed multiple t-test with Bonferroni correction (a-b).

3.4.4 Robust therapeutic effect of CMP_{CDA} in multiple tumor models

To further evaluate the potency of CMP, we examined CMP_{CDA} in tumor models that are refractory to conventional immunotherapies. In the first study conducted with the B16F10 melanoma model, C57BL/6 mice were inoculated at S.C. flank with $3x10^5$ B16F10 tumors cells, and we administered three doses of CMP_{CDA} on three-days intervals via either I.T. route when the average tumor volume reached 153 ± 17 mm^3 (**Fig**. **3-5-1 a-e**) or via I.V. route when the average tumor volume reached 63 ± 7 mm^3. (**Fig. 3-5-1f-j**). We compared CMP_{CDA} with the equivalent dose of four other STING-activating therapeutics, which included CDA-loaded liposomes[167]; CZP particle system formed by replacing Mn^{2+} with Zn^{2+} in CMP; ADU-S100, a leading CDN STING agonist tested in clinical trials[135]; and diABZI, a leading non-CDN STING agonist (used as an I.V. formulation, currently in clinical trials[156]). After I.T. therapy, CMP_{CDA} significantly delayed the tumor growth, eliminated tumors in 30% animals, and prolonged animal survival, whereas other control groups (except for diABZI) showed significantly reduced anti-tumor effects (**Fig. 3-5-1a-e**). Importantly, in the setting of I.V. therapy, CMP_{CDA} also exerted remarkable anti-tumor efficacy, slowing the tumor growth and prolonging animal survival with 20% complete response rate (**Fig. 3-5-1f-j**). In stark contrast, all other control groups (including diABZI) had only minor anti-tumor effects in this difficult-to-treat tumor model. Interestingly, even though CMP and diABZI generated comparable anti-tumor responses after I.T. therapy, CMP significantly outperformed diABZI after I.V. injection (**Fig. 3-5-1f-j**). Moreover, our data showing superiority of CMP to both CZP and CDA-liposomes demonstrates the indispensable role of Mn^{2+}-mediated

potentiation of STING agonists as well as the advantages of our coordination-based STING agonist delivery system.

In the next study, we examined the therapeutic efficacy of CMP in a novel tobacco carcinogen-associated syngeneic squamous cell carcinoma model that is completely refractory to high doses of immune checkpoint blockades (**Fig. 3-5-1k-p**, **3-5-2**). Epithelial malignancies, such as the squamous cell carcinomas of the head and neck, only show a modest response to immunotherapy, typically < 15% in the clinics[176]. To model a cold epithelial malignancy, C57BL/6J mice were given 4NQO-containing (50 μg/mL) drinking water for 16 weeks, and visible oral squamous cell carcinoma lesions were isolated to produce single cell clones, which were then screened *in vitro* and *in vivo*. We identified a cell clone (4-NQO-induced Oral Cancer 1, NOOC1) that stably produced tumors when implanted in syngeneic C57BL/6J hosts (**Fig. 3-5-1k)**. Then, we performed whole exome sequencing to characterize its mutational landscape and found that the mutational signatures of NOOC1 bore 90.7% similarity to the COSMIC signature #4, which is driven by smoking-associated mutations in human cancers (**Fig. 3-5-1l**). We also compared the mutational profiles of NOOC1 tumors to the recently reported 4MOSC cell lines induced by 4-NQO and found the mutation profile of NOOC1 was highly similar to that of 4MOSCs, which validated its tobacco-association (**Fig. 3-5-1l-m**). Notably, NOOC1 was refractory to high doses (200 μg x 6 doses) of immune checkpoint blockade (ICB) therapy, including anti-PD-L1 and anti-CTLA4 **(Fig. 3-5-1)**, which is one of the features of cold-tumors. To evaluate CMP in this ICB-resistant epithelial malignancy model, mice were inoculated with 2 x 10^6 NOOC1 tumor cells, and when the average tumor volume reached > 100 mm^3, animals were treated on days 9, 12, 16, and 20 with CMP_{CDA} or free CDA. We

employed the equivalent CDA dose of 5 μg for I.T. therapy and 20 μg for I.V. therapy. NOOC1 was also refractory to free CDA treatments, regardless of the administration routes. In stark contrast, both CMP I.T. and I.V. therapy led to markedly enhanced anti-tumor efficacy, leading to the regression of established NOOC1 tumors in the majority of animals ($P < 0.0001$) and extended animal survival ($P < 0.001$) (**Fig. 3-5-1n-p**).

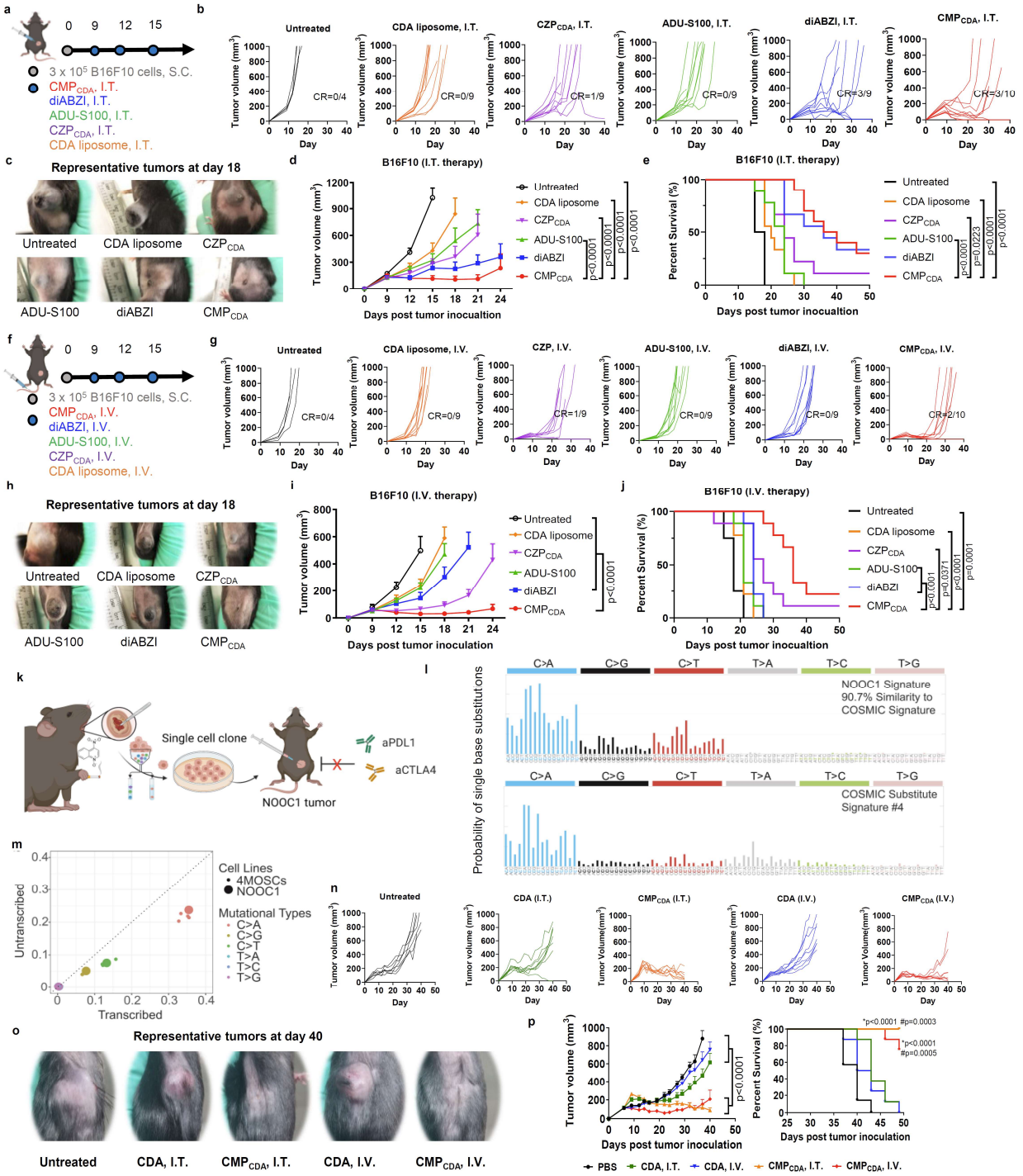

Figure 3-5-1. Robust therapeutic effect of CMP_{CDA} in multiple tumor models. a-j, Therapeutic effect of The therapeutic efficacy of CMP_{CDA} was compared with other CDA formulations and other STING agonists in an established B16F10 tumor model after I.T. injection (**a-e**) or I.V. injection (**f-j**). **a-e)** C57BL/6 mice were inoculated subcutaneously with 3 x 10^5 B16F10 tumor cells. STING agonist formulations (CMP_{CDA}, CDA-Zn particle

(CZP_{CDA}), CDA liposome), ADU-S100, or diABZI (all 5 μg doses of STING agonists) were injected I.T. on days 9, 12, and 15 post tumor inoculation **(a)**. Shown are **b)** the individual tumor growth, **c)** representative photos of tumors, **d)** average tumor growth and **e)** survival. **f-j)** C57BL/6 mice were inoculated subcutaneously with 3 x 10^5 B16F10 tumor cells. CDA-containing formulations (CMP_{CDA}, CDA-Zn particle (CZP_{CDA}), CDA liposome), ADU-S100, or diABZI (all 20 μg doses) were injected I.V. on days 9, 12, and 15 post tumor inoculation **(f)**. Shown are **g)** the individual tumor growth, **h)** representative photos of tumors, **i)** average tumor growth, and **j)** survival. **k-p)** Therapeutic effect of CMP_{CDA} in an immune checkpoint blocker (ICB)-resistant tobacco-associated tumor model (NOOC1). **k**) C57BL/6J mice were given 4NQO-containing (50 μg/mL) drinking water for 16 weeks. Visible oral squamous cell carcinoma lesions were isolated, and a single-cell clone (NOOC1) was confirmed to stably produce tumors when implanted in syngeneic C57BL/6J hosts. **l**) Mutational signatures indicate NOOC1 tumors with high fidelity to human cancers. **m**) Mutational profile of NOOC1 in comparison to other 4NQO-induced murine squamous cell carcinoma cell lines (4MOSCs). **n-p**) C57BL/6 mice were inoculated subcutaneously with 2 x 10^6 NOOC1 tumor cells. On days 9, 12, 16, and 20 post tumor inoculation, mice were treated with CDA in CMP_{CDA} or free form either via I.T. (5 μg dose) or I.V. route (20 μg dose) of administration. Shown are **n)** the individual tumor growth, **o)** representative photos of tumors, **p)** average tumor growth, and survival. Data show mean ± SEM from combined data sets from 2 independent experiments with similar results. * $p < 0.05$, ** $p < 0.01$, *** $p < 0.001$, and **** $p < 0.0001$, analyzed by two-way ANOVA (**d, i, p**) with Bonferroni multiple comparisons post-test. Survival of **(e, j, p)** was analyzed by Kaplan–Meier survival analysis with log-rank (Mantel-Cox) test. *** and ### in (**p**) denote the significance relative to the PBS and CDA groups, respectively.

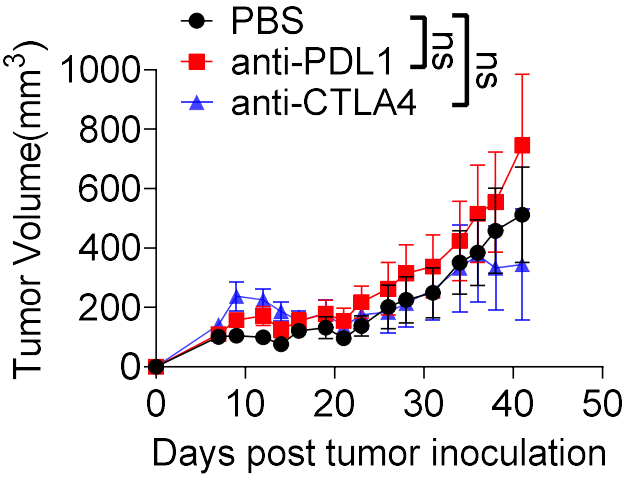

Figure 3-5-2. Characterization of NOOC1 tumor model. NOOC1 was confirmed to stably produce tumors when implanted in syngeneic C57BL/6J hosts and non-responsive

to anti-PDL-1 and anti-CTLA-4 ICB therapy. C57BL mice were inoculated subcutaneously with 2 x 10^6 NOOC1 tumor cells. On day 7, 9, 14, 16, 21, 23 post tumor inoculation, 6 doses of 200 μg anti-PDL1 or anti-CTLA4 in PBS were injected intraperitoneal. Tumor growth was monitored for 40 days **(p)**.

Notably, each injection dose of Mn^{2+} in CMP_{CDA} employed in our I.T. (**Fig. 3-3-1**) and I.V. (**Fig. 3-4-1**) treatment studies was 2.5 μg and 10 μg (0.13 mg/kg and 0.5 mg/kg), respectively. For comparison, the LD_{50} of $MnCl_2$ in mice is 1715 mg/kg[177], and average adults on typical Western diets consume up to 10 mg manganese per day[178]. CMP_{CDA} I.V. therapy transiently increased the serum levels of IFN-□, TNF-□, and IL-6 peaking at 6 hours while inducing a 13.5% maximum body weight loss; however, animals quickly recovered within 3 days, and multiple treatments of CMP_{CDA} or CDA + Mn^{2+} mixture were generally well-tolerated, as indicated by the serum chemistry and neurotoxicity marker (**Fig. 3-5-3, 3-5-4, 3-5-5**). In addition, histological analysis of major organs by a pathologist in a blinded manner showed no abnormal histological conditions among the different treatment groups (**Fig. 3-5-6**).

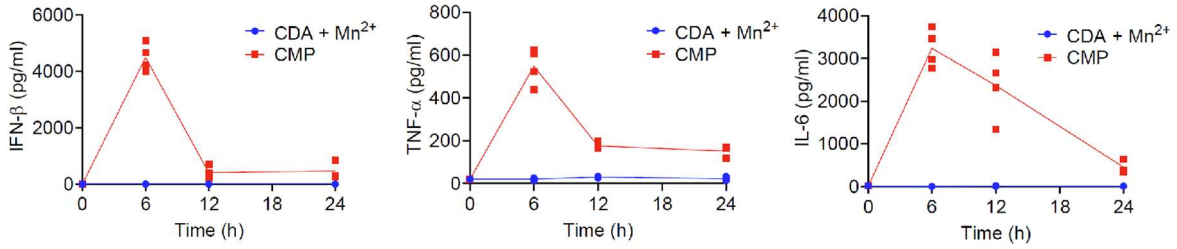

Figure 3-5-3. Serum cytokine profiles after I.V. therapy with CMP. Serum levels of IFN-b, TNF-a, and IL-6 were measured over 24 hrs after I.V. injection of CMP. The data show means and individual replicates, with n=4 biological independent samples.

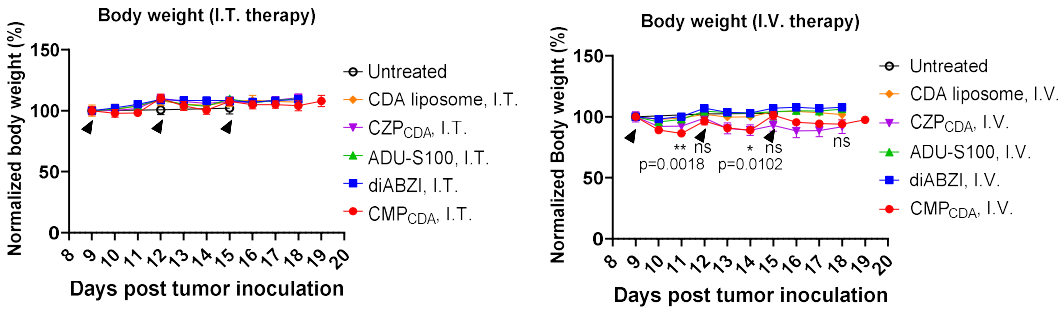

Figure 3-5-4. Body weight changes over the course of CMP treatment related to Fig. 3-5-1 a-g. The data show mean ± SEM, n=4-5. Date were analyzed by two-way ANOVA with Bonferroni multiple comparisons post-test. *p and ns were denoted to statistical significance of CMP, I.V., related to CDA liposome and untreated respectively.

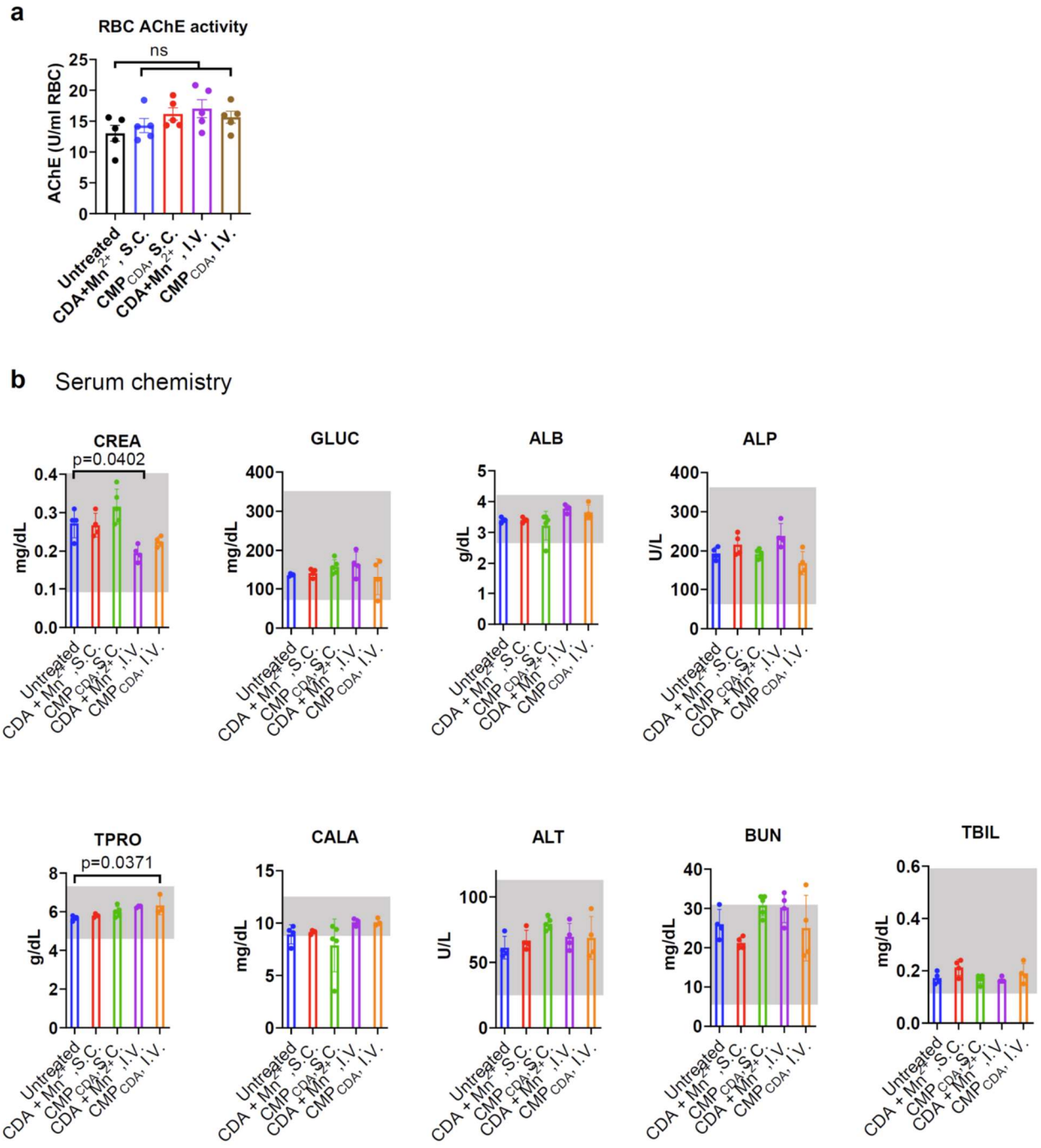

Figure 3-5-5. Safety assessment of CMP_{CDA} after local or systemic injections. a-b) BALB/c mice were injected with CDA + Mn^{2+} or CMP_{CDA} on days 0, 3, and 6 via S.C., I.T., or I.V. routes. Each injection contained 5 μg CDA and 2.5 μg Mn^{2+} for S.C. or I.T. administration. Each injection contained 20 μg CDA and 10 μg Mn^{2+} for I.V. administration. **a)** Activity of acetylcholine esterase (AChE) in RBC was assessed at 2 h after the last injection. **b)** Serum biochemistry was assayed at 96 h after the last injection. The data show mean ± SEM (n=4 biologically independent samples) and were analyzed by one-way ANOVA (**a-b**) with Bonferroni multiple comparisons post-test.

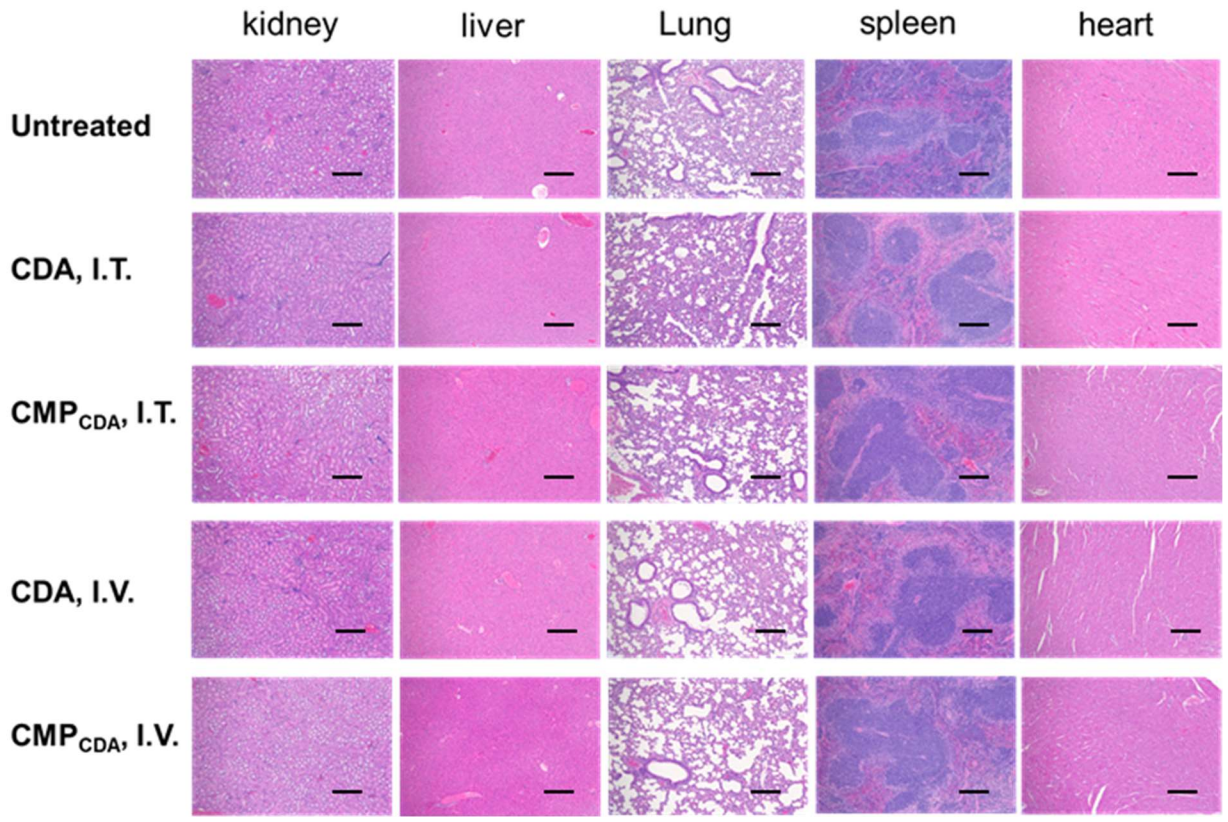

Figure 3-5-6. Histological analysis of major organs after local or systemic injections of CMP$_{CDA}$. BALB/c mice were injected with 3 doses of CDA+ Mn^{2+} or CMP$_{CDA}$ either via I.T. (5 μg CDA and 2.5 μg Mn^{2+}) or I.V. (20 μg CDA and 10 μg Mn^{2+}) route of administration with a 3-day interval. One week after the last injection, major organs were harvested for H&E staining and histological analysis. The tissue sections have been examined by a licensed pathologist in a blinded manner. No abnormal histological conditions (inflammation, necrosis, or structure changes) were reported and no differences between groups were observed. Scale bars = 200 μm. Shown are representative images from 4 biologically independent replicates with similar results.

Overall, CMP represents a major technological advancement to amplify the potency and efficacy of STING agonists. This coordination-based delivery system significantly augmented STING agonist-based cancer immunotherapy in the following aspects. First, CMP effectively delivered STING agonists to immune cells and amplified

the type-I IFN responses of STING agonists **(Fig. 3-2, 3-3, 3-4, 3-5)**. Second, CMP administered I.T. greatly improved the intratumoral bioavailability and exerted robust therapeutic efficacy, achieving significant dose-sparing of STING agonists and Mn^{2+} with minimal side effects **(Fig. 3-3, 3-5)**. Third, CMP exhibited remarkable therapeutic efficacy after I.V. injection in multiple tumor models (**Fig. 3-4, 3-5**). These results suggest that systemically administrated STING agonist in an appropriate delivery system is highly efficacious and should be examined further.

Chapter 4. One-Pot Formulation of CDN STING Agonist for Cancer Therapy and COVID-19 Vaccine

4.1. Abstract

The clinical translation of CDN STING agonists is greatly delayed due to the metabolic instability and poor drug-like properties. Developing appropriate drug delivery system and formulation for STING agonist is also challenging because CDNs are very hydrophilic, and their negative charge is weak. Therefore, the available formulation technologies relying on encapsulation and charge absorption are inefficient and/or instable. Here we try to introduce coordination interaction as a new mechanism for CDN formulation. We have screened different metal ions and found specific metal ions are more efficient to coordinate with CDN. Especially, Zn-CDA formed interesting crystal structure. To design an efficient nanoparticle formulation, we also introduced Mn2+ and H33-PEG in the coordination system given that Mn2+ has some potentiation effect on STING activation and H33-PEG are biocompatible and ionizable for endosome escape. By simple one-pot synthesis, we got homogeneous nanoparticle formulation of STING agonist, CDA-Zn/Mn@H33-PEG (CZMP). In animal studies, CZMP could not only induce higher immune activation for cancer immunotherapy after systemic injection but also function as effective vaccine adjuvant for COVID-19 vaccine. Overall, CZMP represents an effective versatile platform for STING agonist delivery for disease treatment and prevention.

4.2. Introduction

Developing new polymorphs has been widely used to improve the performance of drugs and many pharmaceutical companies are patenting new polymorphs to lengthen the Drug Patent Life Cycle and keep generic competition off the market longer. Crystalline forms of a drug, called polymorphs, may provide benefits such as better efficacy, solubility, shelf life, or ease of manufacture, which can translate into increased adoption of the drug and higher sales.

STING agonist is a potent powerful cancer immunotherapy that is gaining significant research interest. The vast majority of STING agonists under clinical development are cyclic dinucleotides (CDN) and their derivatives, including those from Aduro/Novartis, Bristol-Myers Squibb/IFM Therapeutics and Merck. Importantly, conventional nucleotide-based STING agonists have several major limitations: 1) STING agonists in clinical trials now are administrated via intratumoral injection due to their poor pharmaceutical properties, including low bioavailability and off-target toxicity. For example, the half-life of MIW815 in serum is only ~16 min, and over 98% of MIW815 entered the systemic circulation 1 hour after intratumoral injection in a phase 1 clinical trial. This precludes their applicability for the treatment of metastatic cancer. 2) Nucleotide-based STING agonists generally do not cross the cell membrane, thus limiting activation of intracellular STING. Therefore, there is an urgent need to find a simple and translational formulation for delivery of CDN STING agonists.

We have made a surprising discovery that specific metal ions could coordinate with CDNs and form new coordination structures or polymorphs. Such coordination structures or polymorphs may be used to improve the pharmaceutical properties and

therapeutic effect of CDN STING agonist. These coordination structures or polymorphs are generally formed by self-assembly in water by simple admixing, thus expediting the manufacturing process and clinical translation. Especially, after adding H33-PEG to the coordination process, we could get a stable nanoparticle formulation of CDN STING agonist using one-pot assembly. In animal studies, CZMP could not only induce higher immune activation for cancer immunotherapy after systemic injection but also function as effective vaccine adjuvant for COVID-19 vaccine. Overall, CZMP represents an effective versatile platform for STING agonist delivery for disease treatment and prevention.

4.3. Materials & Methods

4.3.1. Synthesis of CDN STING agonist-metal coordination structure/polymorphs

c-di-AMP (CDA) were obtained from Invivogen and dissolved in water to obtain 2 mg/ml solution. $ZnCl_2$, $MgCl_2$, $MnCl_2$, CaCl2, $Al_2(SO_4)_3$, $CuCl_2$, $FeCl_2$, $FeCl_3$, $NiCl_2$ and $CoCl_2$ (Sigma-Aldrich) was each dissolved in water to prepare 100 mM solution. To screen for metal ions that could coordinated with CDA, 5 or 10 equivalents (n/n) of metal ions were added to 2 mg/ml CDA solution. The mixture solution was incubated for 2 hours at room temperature. The resulting CDN-metal coordination structure could be observed under microscope. The degree of precipitation of CDN-metal solution could be measured by measuring absorbance at OD450 nm, OD500 nm, and OD 600nm after subtracting the background absorbance. Loading efficacy of CDN in the coordination structure were measured by quantifying the CDN in the supernatant and pellets after centrifugation 10000 xg, 15 min.

4.3.2. Synthesis of CDA-Zn@H33-PEG and CDA-Zn/Mn@H33-PEG (CZMP).

CDA-Zn@H33-PEG and CDA-Zn/Mn@H33-PEG (CZMP) were prepared by adding Zn2+ or Zn^{2+}/Mn^{2+} to pre-mixed CDA and H33-PEG_{20k} with stirring. Briefly, polyhistidine-PEG was added dropwise to CDA solution with continuous stirring. Then, 10-80 eq Zn^{2+}/Mn^{2+} were added to CDA/H33-PEG_{20k} mixture under stirring and reacted for 12 hours. CDA-Zn@H33-PEG or CZMP were isolated by centrifuge or centrifugal ultrafiltration (100kD). The final products were further characterized by dynamic light scattering (DLS), transmission electron microscopy (TEM), and absorbance measurement.

4.3.3. In vitro release analysis

The release profiles of formulations were studied by a Slide-A-Lyzer™ MINI Dialysis Device, 20 KD MWCO (Thermo Scientific). Briefly, 0.5 ml formulation solution was filled in the cup with regenerated cellulose membrane and 14 ml release buffer (PBS) was put in the tube. After dialysis cup was inserted into the conical tube and capped, the device was incubated at 37 ^{o}C under continuous shaking (200 rpm). At the indicated time points, 300 ul of release media were collected and equal amount of fresh PBS was refilled. The concentration of CDN in the release medium was analyzed by HPLC (GPC) and concentration of Mn^{2+} in the release medium was analyzed by ICP-MS. Finally, the release amount over time was calculated based on the CDN concentration in the release buffer, volume of buffer, and the total CDN loading amount.

4.3.4. In-vivo cancer immunotherapy

All animals were cared for following federal, state, and local guidelines. All work performed on animals was in accordance with and approved by the University Committee on Use and Care of Animals (UCUCA) at University of Michigan, Ann Arbor. For CT26 murine tumor model, female BALB/c mice of age 6–8 weeks (Jackson Laboratories) were inoculated with 1.5 x 10^5 CT26 colon cancer cells subcutaneously on the right back flank. For the B16F10 tumor model, C57BL/6 mice (Jackson Laboratory) were inoculated with indicated number of B16F10 cells subcutaneously on the right flank. Tumor-bearing mice were randomly assigned to different treatment groups. Indicated drugs or formulations were administrated via indicated route at indicated time points. Tumor size and survival were monitored every 2-4 days. Tumor size was calculated based on equation: volume = length × width^2 × 0.5. Animals were euthanized when the tumor reached 1.5 cm in diameter or when animals became moribund with severe weight loss or un-healing ulceration. At indicated time points, the cytokine levels in serum were measured by ELISA assay in the Cancer Center Immunology Core of the University of Michigan.

4.3.5. In-vivo immunization with COVID-19 vaccine

Mice (Balb/c) were vaccinated three times at tail base with 2 weeks intervals. 2 weeks after each vaccination and 4 and 8 weeks after the last vaccination, sera were collected for antibody titer measurement by ELISA. In a separate study, spleens were harvested 1 week after the last vaccination for ELISPOT assay. For ELISA assay, 96-well plates were pretreated overnight with 0.1 μg of RBD (dissolved in carbonate-bicarbonate buffer, pH9.6) per well. After removing RBD, wells were washed three times

with wash solution and further incubated with blocking solution (1% BSA in PBS) for 2 hours in RT, then washed three times with wash solution (0.05% Tween 20 in PBS). Next, sera samples were put into the plates. Sera samples were serially diluted by 1:4 or 1:5 six times with a starting dilution of 1:100. After incubating the samples for 1 hour in RT, samples were removed, followed by three times of washing. Next, 1:1000-diluted HRP-conjugated anti-mouse IgG antibodies (ab6728; Abcam) were added and incubated for 1 hour in RT. After the incubation, antibodies are removed and the wells are washed 4 times with wash solution, then substrate solution (Ultra TMB-ELISA; Thermo Scientific) is added and incubated for 10 min or until the reacting solution colors are well developed in RT. The reaction is stopped by adding 1 M H_2SO4, then the plates are read at a wavelength of 450 nm.

4.3.6. ELISPOT assay

A day before spleen harvest, a 96-well ELISPOT plate is coated with capture antibody (anti-IFN-γ antibody). After overnight incubation in 4C, wells are washed with blocking solution, followed by incubation with blocking solution for 2 hours. Next the blocking solution is removed and RBM peptides are added to the wells in 10 μg/ml concentration. Spleens were harvested 1 week after the last vaccination. Each spleen was placed on top of a 40 μm strainer then mashed with a plunger. The strainer was washed with PBS to let splenocytes pass through into a collection tube. After centrifugation at 300 g for 5 min, each cell pallet was resuspended with ACK lysis buffer and incubated for 5 min in RT. Next, the cells were centrifuged and washed with PBS twice. Resulting cells were counted and $2x10^5$ cells were seeded in each well of the 96-well ELISPOT plate containing the RBM peptide and incubated in 37C for overnight.

Next, cell suspensions are aspirated out and the wells are washed twice with deionized water followed by three times of washing with wash solution. Detection antibody is added and incubated for 2 hours in RT. After incubation, antibodies are removed, wells are washed three times with wash buffer, then HRP-conjugated streptavidin is added and incubated for 1 hour in RT. Following incubation, well are washed four times with wash buffer and two times with PBS. Substrate solution is added and incubated until spots are developed in the wells. Wash the wells with water to stop the development. Air-dry overnight in RT then the plates are imaged with an ELISPOT reader.

4.3.7. SARS-CoV-2 pseudovirus neutralization study

To assess the correct dilution of SARS-CoV-2 Spike pseudoparticles for luciferase detection, a series of experiments were performed using HEK293T cells expressing human ACE2 (293T-hACE2). Pseudoparticles were first produced by transient transfection of HEK293T cells in 10 cm cell culture dishes. 3,000,000 cells per were seeded in 10 mL of cell culture media (Gibco DMEM with 10% FBS and 1% Penicillin-Streptomycin) and incubated at 37˚C and 5% CO_2 for 24 hours. Transfections were performed by mixing 250 ng SARS-CoV-2 Spike plasmid:2500 ng psPAX2:2500 ng CMV-eGF1 (a combined luciferase and eGFP reporter) in a microcentrifuge tube and adding OptiMEM to a final volume of 262.5 uL. 15.75 uL FugeneHD was then added and the mixture was mixed thoroughly. This mixture was incubated for 15 min at RT and then added to culture media and mixed by gentle agitation. Media and transfection mixture was aspirated after 24 hours and replaced with DMEM and cells were observed for GFP under a fluorescent scope. Pseudoparticles were harvested both on day 3 and day 4 post-transfection, mixed, aliquoted, and stored at -80˚C. 10,000 293T-hACE2

cells/well were seeded into 96-well plates and incubated at 37˚C and 5% CO_2 for 24 hours. Cells were then transduced with VSV-G pseudoparticles in dilutions of 1:5, 1:10, and 1:20 in DMEM supplemented with 10% FBS and 1% Pen-Strep and 1:1000 polybrene to 8 ug/mL, then incubated for 72 hours at 37˚C. To assess transduction had occurred, media was aspirated, then cells were lysed in well and assessed for luciferase activity. 1:5 dilutions were determined to show >100-fold rluc signal over the background signal. From these initial optimization results, neutralization of SARS-CoV-2 pseudoparticles by candidate antibodies was assessed. Opaque, 96-well, half area plates were seeded with HEK293T-hACE2 cells at a density of 5000 cells/well and incubated for 24 h at 37˚C and 5% CO_2. Prior to infection, serial 1:3 dilutions of antibodies were performed in 10% FBS DMEM + 1:1000 polybrene to an 8 ug/mL final concentration in a separate 96-well plate. SARS-CoV-2 pseudoparticles were then mixed with these dilutions to a final concentration of 1:5. Media was aspirated from culture plates, then 50 uL of each mixture was pipetted into culture plates. These infections were incubated for 72h at 37˚C and 5% CO_2. After incubation, infection mixtures were aspirated from plates and assessed for luciferase activity.

4.4. Results & Discussion

4.4.1 Coordination behaviors of metal ions and STING agonists and one-pot synthesis of CDA-Zn/Mn@H33-PEG (CZMP)

As shown in **Fig. 4-4-1**, after addition of metal ions into CDA solution, significant precipitation were observed for Mn^{2+}, Al^{3+}, Fe^{3+},Cu^{2+}, Zn^{2+}, Ca^{2+}, but not for Mg^{2+}, Fe^{2+}, Co^{2+}, Ni^{2+}. The loading efficacy of CDA in the coordination structure is over 80% for Mn^{2+}, Al^{3+}, Fe^{3+}, Cu^{2+}, Zn^{2+}. In the microscopy images, various coordination

structures/polymorphs could be observed for Mn^{2+}, Al^{3+}, Fe^{3+},Cu^{2+}, Zn^{2+}, and Ca^{2+}. Insterestingly, Mn^{2+} formed the most significant coordination precipitation while Zn^{2+} formed defined crystal structures. Interestingly, when Zn^{2+} was added to CDA solution, needle-like crystals/ polymorphs were observed when Zn/CDA was greater than 0.1:1. On ther other hand, 0.5 eq Zn^{2+} formed larger but less needle-like crystals, while 4 and 8 eq Zn^{2+} formed needle-like clusters. When Zn/CDA achieve 10:1, we observed the formation of homogeneous cuboidal crystals/polymorphs. In order to design a nanoparticle delivery system of STING agonist, we also introduced Mn and H33-PEG in the coordination system given that Mn has some potentiation effect on STING agonist and H33-PEG are biocompatible and ionizable for endosome escape. By simple one-pot synthesis, we got a homogeneous nanoparticle formulation of STING agonist, CDA-Zn/Mn@H33-PEG (CZMP), as shown in **Fig. 4-4-2**. We also synthesized some CZMP analogs (**Fig. 4-4-3**). Zn-CDA@H33-PEG demonstrated well-defined nanostructure due to the more organized coordination between Zn-CDA and Zn-H33. For the stability in PBS, CZMP > Zn-CDA@H33-PEG > Mn-CDA@H33-PEG. It is probably because Zn and Mn have different coordination site and CZMP stability is enhanced by both Mn-mediated and Zn-meditated coordination.

We further tested the bioactivity of CAMP in vitro (**Fig. 4-4-4)**. Compared with CDA, CDA + Mn and/or Zn2+, Zn-CDA@H33-PEG, Mn-CDA@H33-PEG BMDC, CZMP could significantly elevate the expression levels of CD80 and CD86 on BMDCs, which indicates higher STING activation (**Fig. 4-4-4a**). In THP1-STINGR[232], we also found CZMP could induce higher IFN-I production and other related cytokines in a much low concentration of STING agonist (**Fig. 4-4-4b**). The high STING activation could be

explained by the increased cellular uptake of STING agonists by BMDCs after CZMP treatment (**Fig. 4-4-4c**) and efficient endosome escape (**Fig. 4-4-4d**).

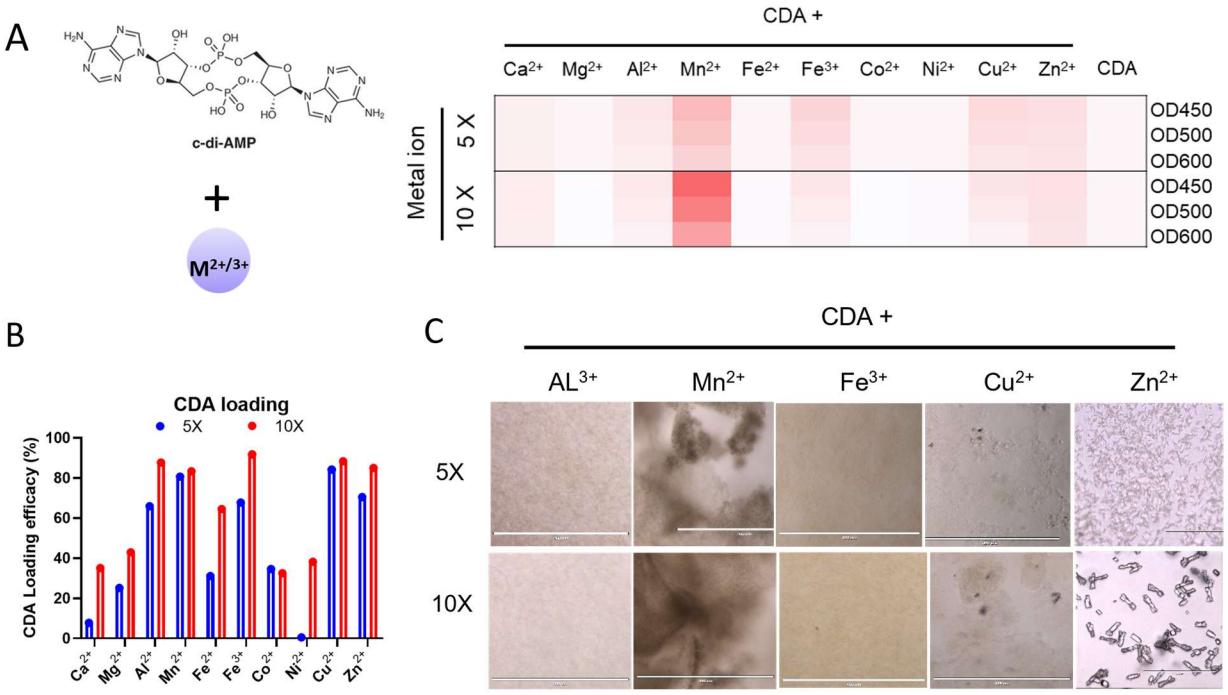

Figure 4-1-1. Synthesis of CDN STING agonist-metal coordination structure/polymorphs. A-C) screen for metal ions coordination with CDN STING agonists. 100mM $ZnCl_2$, $MgCl_2$, $MnCl_2$, CaCl2, $Al_2(SO_4)_3$, $CuCl_2$, $FeCl_2$, $FeCl_3$, $NiCl_2$ and $CoCl_2$ (Sigma-Aldrich) solutions in water were added to 2mg/ml CDA in 5 or 10 equivalents (n/n). The mixture solution was incubated for 2 hours at room temperature. A) The degree of precipitation of CDN-metal solution could be measured by measuring absorbance at OD450 nm, OD500 nm, and OD 600nm after subtracting the background absorbance. B) Loading efficacy of CDN in the coordination structure was measured by quantifying the CDN in the supernatant and pellets after centrifugation 10000 xg, 15 min. C) The resulting CDN-metal coordination structure could be observed under microscope.

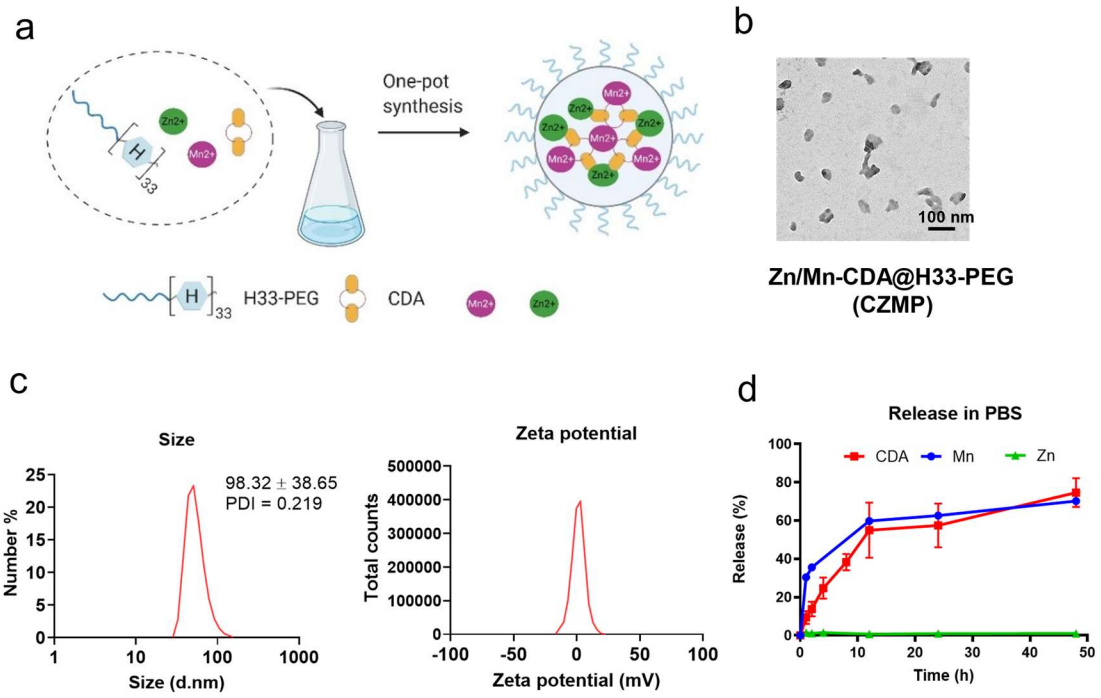

Figure 4-1-2. **One-pot synthesis of CDA-Zn/Mn@H33-PEG (CZMP)**. a) CDA, H33-PEG_{20k}, and Zn^{2+}/Mn^{2+} were mixed in order under continuous stirring in a one-pot synthesis. b) TEM image of the resulted CZMP nanoparticle. c) DLS size and zeta potential of CZMP. d) Release kinetics of CDA, Mn and Zn from CZMP in PBS media.

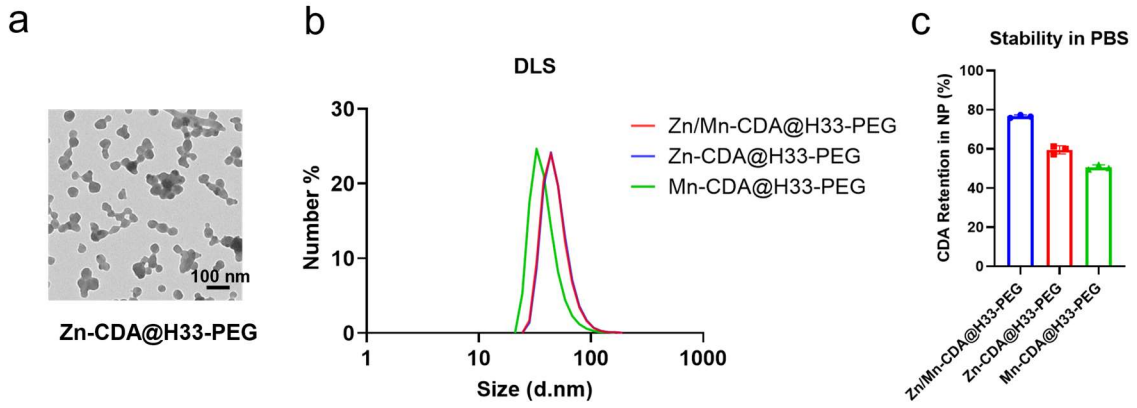

Figure 4-1-3. **One-pot synthesis of CZMP analogs and their characterization**. a) CDA, H33-PEG_{20k}, and Zn^{2+} were mixed in order under continuous stirring in a one-pot synthesis to get Zn-CDA@H33-PEG. b) DLS size of CZMP and its analogs. d) stability of CZMP, Zn-CDA@H33-PEG and Mn-CDA@H33-PEG in PBS media.

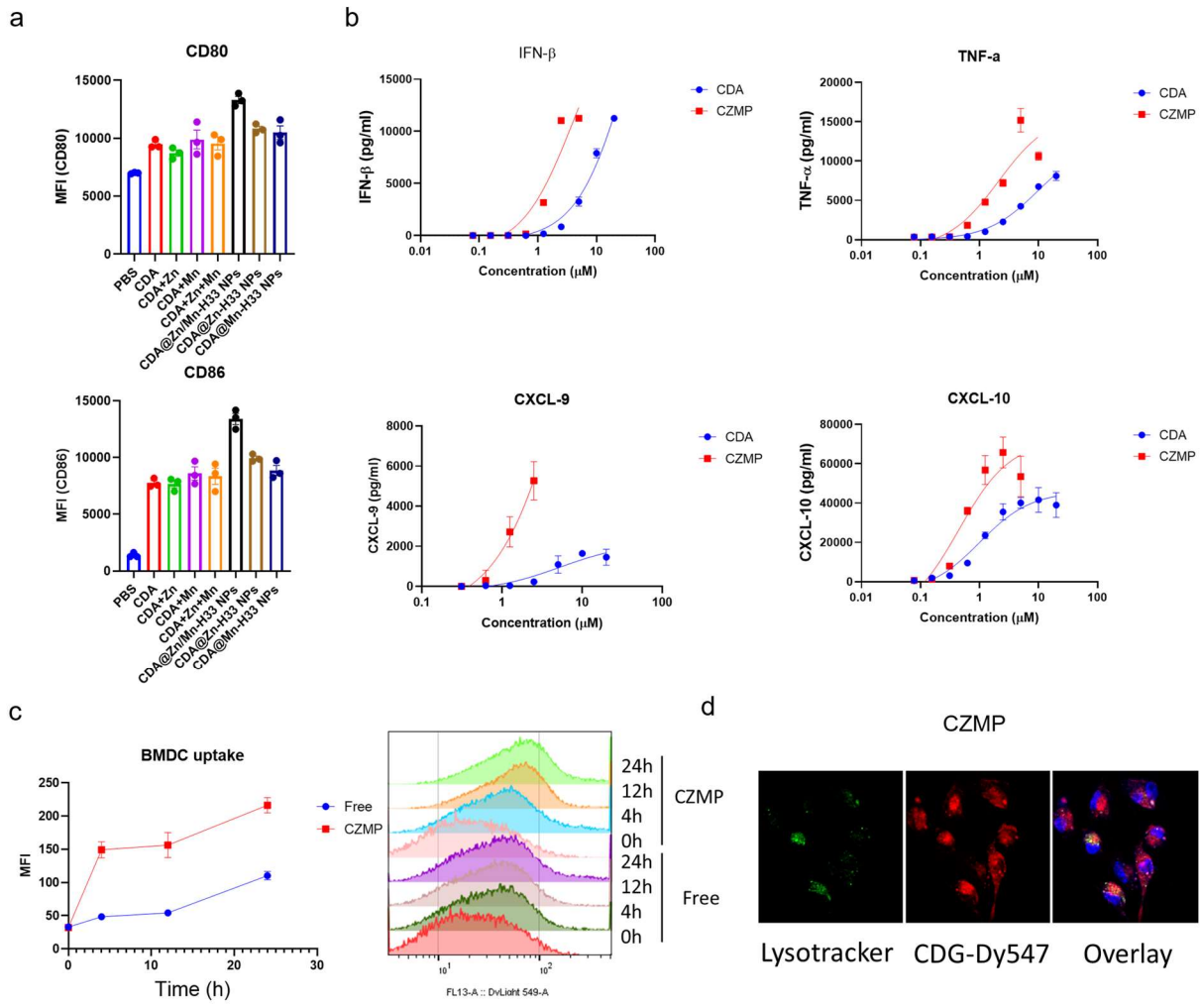

Figure 4-1-4. **In vitro evaluation of CZMP-induced immune activation**. a) CZMP could induce increased dendritic cell activation. b) CZMP could induce increased production of type-I IFNs and other pro-inflammatory cytokines. c) CZMP could increase cellular uptake of STING agonist. d) confocal imaging of subcellular distribution of CZMP shows effective endosome escape.

4.4.2. Cancer therapy by CZMP

To evaluate the therapeutic potential of CZMP in vivo, CT26 tumor-bearing BABL/c mice were treated with I.V. administration of CZMP or free CDA on days 11, 14, 17, and 21. Compared with the free CDA, CZMP increased the serum levels of IFN-β, TNF-α, CXCL-9, and CXCL-10 (**Fig. 4-2-1b**) demonstrating higher immune activation. Importantly, CZMP administered I.V. significantly inhibited CT26 tumor growth and

prolonged the survival of mice (**Fig. 4-2-1 c, e**). Flow cytometry analysis performed on day 27 showed that CZMP I.V. therapy significantly expanded NK cell population in PBMCs and induced high NK cell activation in tumor-draining lymph node (**Fig. 4-2-1 d, f**). The similar therapeutic response of CZMP was also validated in B16F10 melanoma that were treated after I.V. injection. CZMP I.V. therapy efficiently inhibited B16F10 tumor growth with significantly enhanced therapeutic efficacy, compared with free CDA (**Fig. 4-2-1 g-i**). Altogether, these results suggest that CZMP is a simple yet efficient formulation for systemic delivery of STING agonist for cancer immunotherapy.

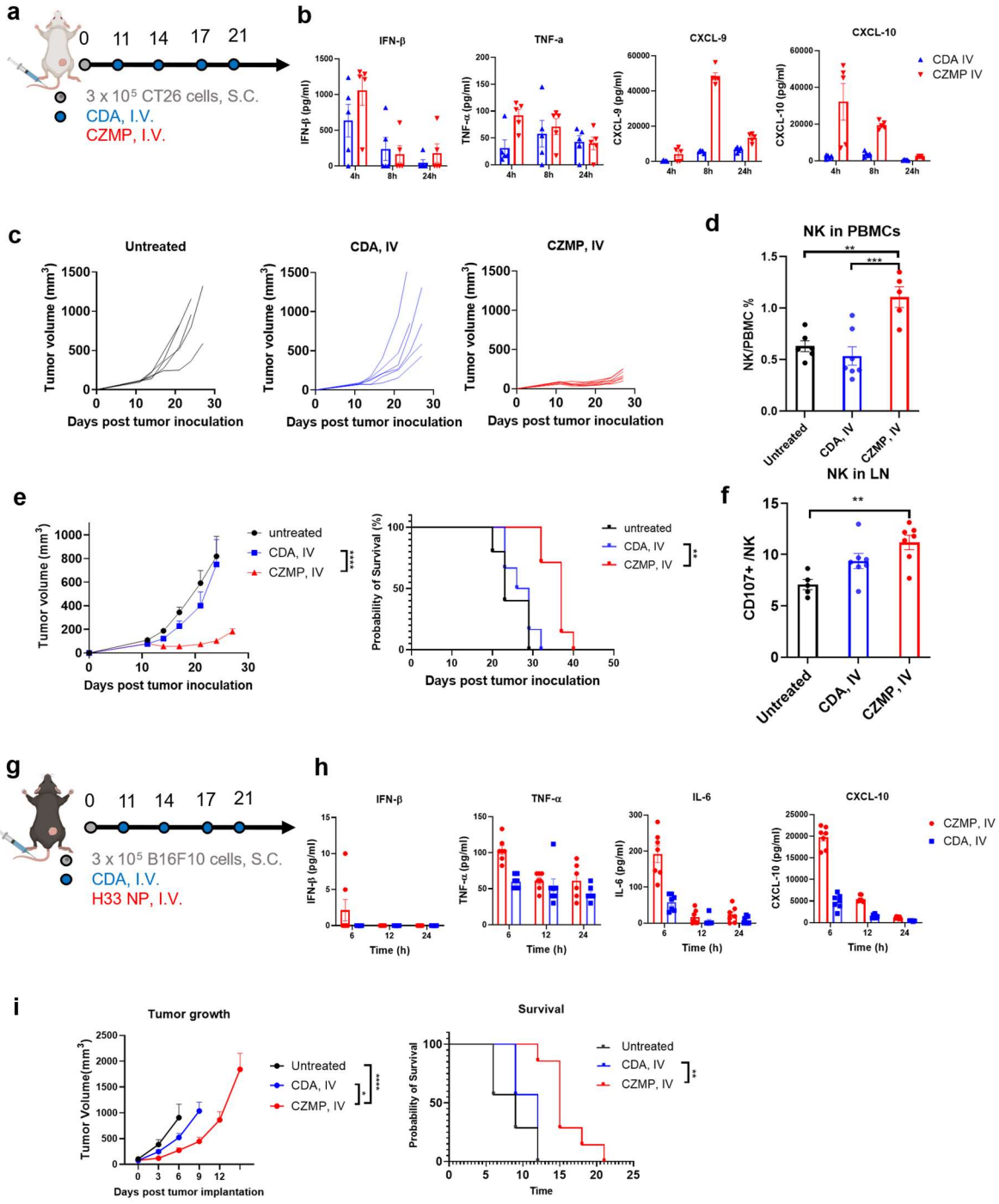

Figure 4-2-1. **In vivo cancer immunotherapy effect of CZMP**. a-f) Therapeutic effects of CZMP on CT26 tumors after I.V. administration. **a)** BALB/c mice were inoculated at S.C. flank with 3 x 105 CT26 tumor cells. 20 μg CDA in free form or CZMP were injected I.V. on days 11, 14, 17, and 21. **b)** Serum cytokines were measured by ELISA at 6 h post the second dose. **c, e)** Tumor growth **(c, e)** and animal survival **(e)** were

monitored over time. **d, f)** NK cell frequency in blood **(d)** and NK cell activation in tumor draining lymph node **(f)** were analyzed by flow cytometry. **g-i)** Therapeutic effects of CMPCDA administered I.V. on B16F10 tumors. C57BL/6 mice were inoculated at S.C. flank with 3 x 10^5 B16F10 tumor cells. 20 μg CDA in free form or CZMP were injected I.V. on days 11, 14, 17, and 21 **(g)**. **h)** Serum cytokines were measured by ELISA at 6 h post the second dose. **i)** tumor growth and survival were monitored over time. Data represent mean ± SEM, from a representative experiment from 2 independent experiments with $n = 5$ (b-), $n = 5$-7 (c-f, h-i). $^*P < 0.05$, $^{**}P < 0.01$, $^{***}P < 0.001$, $^{****}P < 0.0001$, analyzed by (d,f) one-way ANOVA or (e,i) two-way ANOVA with Bonferroni's multiple comparisons test, or (e, i) log-rank (Mantel-Cox) test.

4.4.3 CZMP as COVID-19 vaccine adjuvants

STING agonists have been reported as efficient vaccine adjuvants for vaccines of cancer and infectious diseases. Therefore, we further tested whether CZMP could be serve as effective vaccine adjuvant for COVID-19 vaccine. Interestingly, polyhistidine-tag technology are widely used for protein isolation and a large portion of recombinant proteins are grifted with polyhistidine-tags. Used the sample histidine-Zn/Mn coordination interaction, we could load various antigen with poly his tag onto CZMP. To confirm this, we added COVID-19 S1 protein RBD with 6x his tag into CZMP and quantified the protein loading after pulling down the nanoparticle. As shown in **Fig. 4-3-1**, >90% RBD could be effectively loaded onto CZMP based on SDS-PAGE result. As shown in the IVIS imaging result, we also found CZMP after subcutaneous injection could traffic to lymph node effectively. This indicates CZMP could home to LN for effective delivery of antigens to B cell and antigen presenting cells.

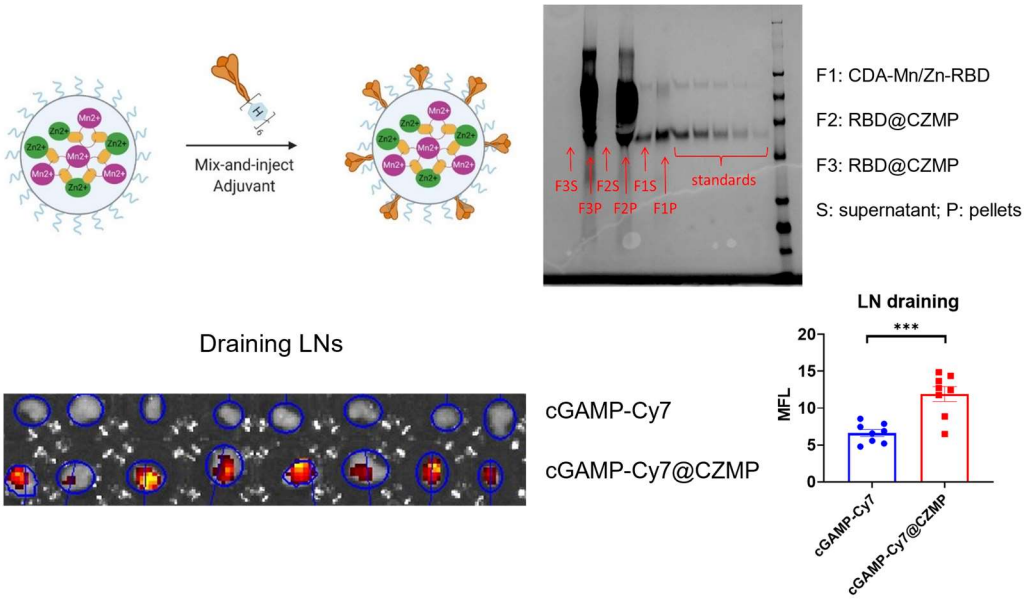

Figure 4-3-1. **Loading of COVID-19 S1 RBD proteins in CZMP for lymph node delivery as COVID-19 vaccine**.

To evaluate the vaccine response of RBD@CZMP in vivo, balb/c mice were vaccinated three times at tail base with 2 weeks intervals. 2 weeks after each vaccination and 4 and 8 weeks after the last vaccination, sera were collected for antibody titer measurement by ELISA. As shown in **Fig. 4-3-2a**, CZMP could significantly increase the neutralizing antibody production. In a separate study, spleens were harvested 1 week after the last vaccination for ELISPOT assay (**Fig. 4-3-2b**). We tested the T cell response of RBD@CZMP to a panel of epitopes within RBD. Strikingly, we found very high level of T cell response was observed (as high as 400/0.2M splenocytes), especially against sequence 438-458, 450-473. As shown in **Fig. 4-3-2c,** The ELISPOT study was also repeated in another separate study in comparison with RBD, RBD + free CDA, and RBD + free CDA+ Mn+ Zn. RBD@CZMP could induce significantly higher T cell response. In the same study, we also observed improved

germinal center formation after RBD@CZMP vaccination (**Fig. 4-3-2c, right panel**). Finally, we have also tested whether the antibody response induced by RBD@CZMP could neutralize SARS-CoV-2 virus infection. As shown in **Fig. 4-3-2d**, we treated the immunized mouse sera of week 6 and 14 to reporter cells and added SARS-CoV-2 pseudovirus or SARS-CoV-2 virus. We found RBD@CZMP could induce effective neutralizing antibody to neutralize SARS-CoV-2 pseudovirus and SARS-CoV-2 virus, which indicated CZMP is a potent vaccine adjuvant platform for COVID-19 vaccine and other vaccines.

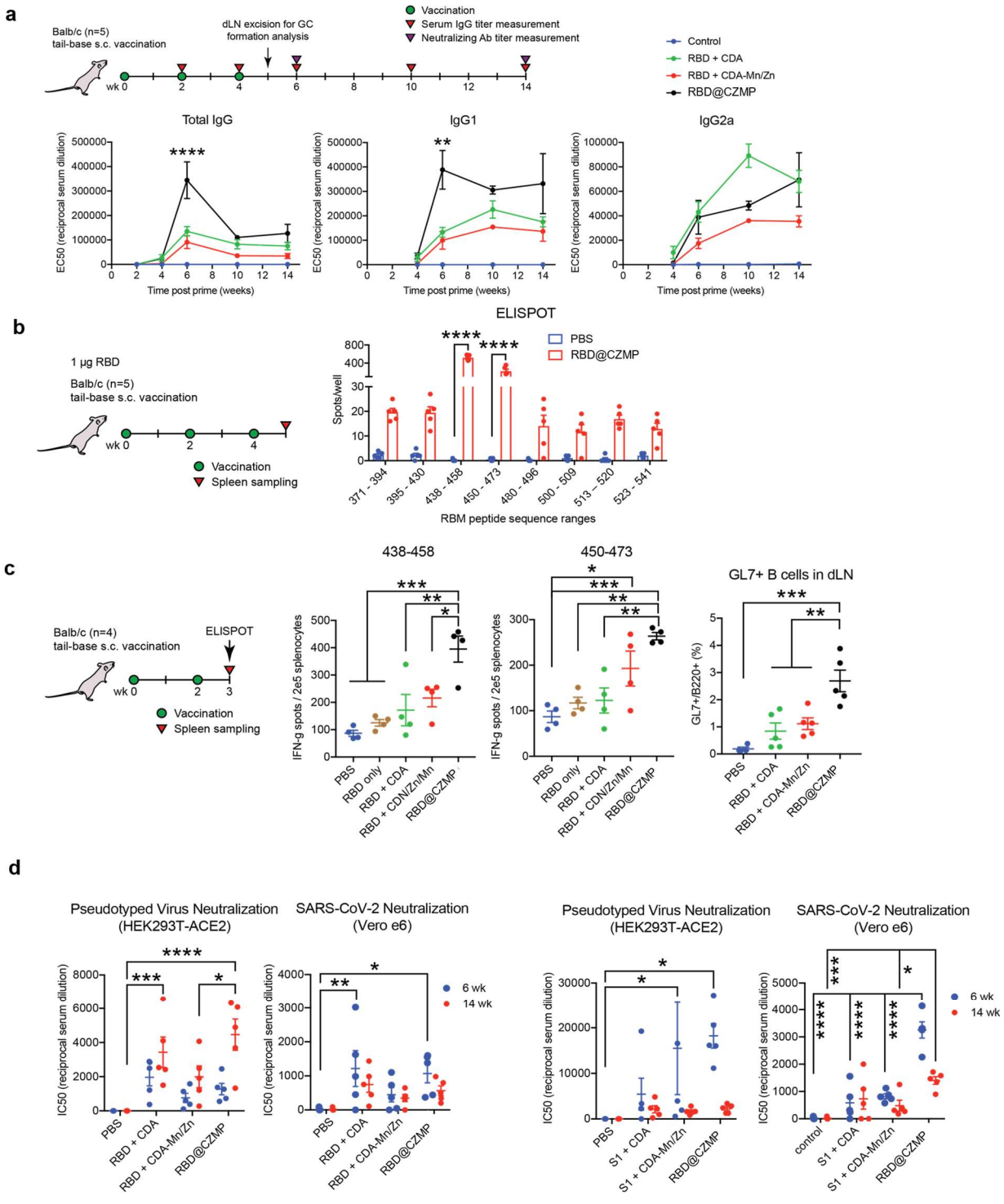

Figure 4-3-2. In-vivo immunization with RBD@CZMP as effective COVID-19 vaccine.

Chapter 5. Conclusions & Perspectives

Within this dissertation, I have explored metal immunotherapy as a new module of cancer immunotherapy. In the introduction, I systematically reviewed the status of metalloimmunotherapy and classified it into five categories. For each categories, I discussed the principle, the progresses, and future directions. The purpose is to provide a route map for metalloimmunotherapy development. The great potential of metalloimmunotherapy has motivated my work in Chapter 2-4: apply novel pharmaceutical formulation technologies to develop effective metalloimmunotherapies for disease treatment.

In the first project, I have screened various metal ions to look for metal ions that could potentiate STING agonists. I discovered Co^{2+} and Mn^{2+} metal ions augmented STING agonist activity, wherein Mn^{2+} promoted a 12- to 77-fold potentiation effect across the prevalent human STING haplotypes. CDA + Mn^{2+} combination significantly elevated the expression levels of CD80 and CD86 on BMDCs and eradicated CT26 tumors in 80% of mice after IT injection. Mice treated with CDA + Mn^{2+} exhibited significantly elevated antigen-specific T cell response and immune memory effect against second CT26 re-challenging. These results show that Mn^{2+} potentiates STING agonist activity *in vivo* and induces effective anti-tumor T cell response. The work in this part also indicate metal ions could be a simple yet effective component to synergize with existing cancer immunotherapies.

In the second project, I demonstrate a prototype of highly effective cancer metalloimmunotherapy based on CMP. CMP administered either by local intratumoral or systemic intravenous injection initiated robust anti-tumor immunity, achieving remarkable therapeutic efficacy with minute doses of STING agonists in multiple murine tumor models, including the immune checkpoint blockades-resistant tumors. Tumor microenvironment analysis revealed CMP could induce conversion of “cold tumor” to “hot tumor”. In a benchmark study, CMP also demonstrated a superior therapeutic effect than the leading STING agonist in clinical trials. This not only indicates CMP offers a robust platform for local and systemic cancer treatments but also suggests that pharmaceutical formulation may be critical for a successful metalloimmunotherapy. Given that metal ions usually lack selectivity, appropriate formulation design could greatly improve the therapeutic properties.

In the third project, I have screened different metal ions and found specific metal ions are more efficient to coordinate with CDNs. By simple one-pot synthesis, I got a homogeneous nanoparticle, CDA-Zn/Mn@H33-PEG (CZMP). After systemic administration, CZMP could induce higher immune activation for cancer immunotherapy. CZMP could also load protein antigen with polyhistidine tag to serve as both delivery system and adjuvant. After immunization in mice, S1 RBD@CZMP induced effective neutralizing antibodies to neutralize SARS-CoV-2 pseudovirus and SARS-CoV-2 virus. Overall, this highlighted coordination interaction as a new mechanism for CDN formulation. Broadly, this work, along with the second project, also underscores the great potential of coordination nanomedicine for precise delivery of metalloimmunotherapy.

I expect future studies on metalloimmunotherapy and precise nanomedicine development would greatly accelerate the development of more effective and safer metalloimmunotherapeutics. Here are some of my thoughts on the future directions:

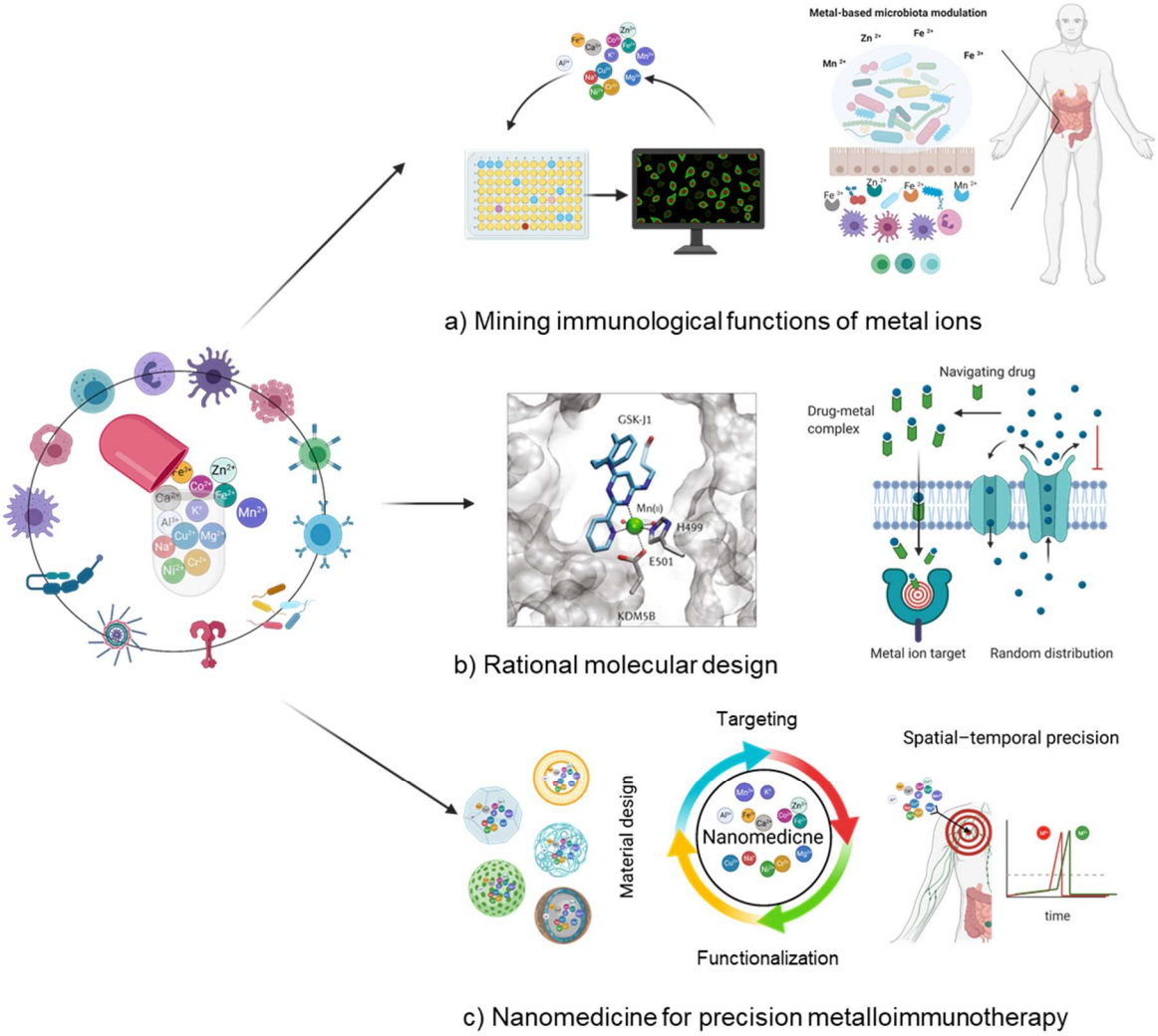

Figure 5-1. Perspective of metalloimmunotherapy.

5.1. Mining immunological functions of metal ions

Even though the past decades have witnessed some exciting discoveries of metal ions' immune functions and the underlying mechanisms, a more systematic research

approach is needed to facilitate the development of this field. For example, metallomics has been proposed to study the interaction of metal or metalloid elements with life processes in a systematic vision[179]. Even though metallomics is still in its very early stage and faces some technical challenges, its future development, especially in immune metallomics, may provide a powerful tool for us to study in metalloimmunology and help develop better metalloimmunotherapy. In addition to metallomics, high-throughput screening approaches could also be developed to look for metal ions' unknown immune functions. Moreover, the composition of gut microbiota has been identified as a critical modulator for various diseases, immunity and immunotherapies[64, 67]. Given metal's capability to affect microbes[65, 142], it is expected that metal ions in an appropriate manner could be leveraged to promote the outgrowth of the favored strains or specific compositions of host microbiota. In this scenario, metal-mediated gut microbiota modulation may become the next frontier of metalloimmunotherapy.

5.2. Rational molecular design for metalloimmunotherapy

To preciously control metal ions' physiological function in life, structure-based drug design is indispensable. Generally, molecular manipulation of metal ions includes two parts: 1) targeted modulate the activity of chelated metal ions in metalloprotein; 2) specifically manipulate the behavior of free metal ion in physiological process. For the first part, extensive efforts have been invested by medicinal chemists because metalloprotein account a large portion of all proteins and metal ions usually play critical structural or functional roles in the proteins. Taking advantage of ligand-metal interaction for drug design has proved to be a successful way to develop drugs for various targets, which has been reviewed in several reviews and would not be

expanded here[180-183]. For the second part, it is much less explored because it is usually challenging to target specific free metal ions in a specific process. Recently, Liam Guthrie et al. discovered that Elesclomol could target Cu and transport Cu to brain and specifically to cell mitochondria in brain to treat Menkes disease[184]. Menkes disease is a severe lethal disease caused by genetic deficiency in copper-transporting adenosine triphosphatase ATP7A and associated with progressive neurological injury due to impaired cytochrome c oxidase (CcO) activity in brain. Interestingly, Elesclomol could transport Cu across cell membrane and escorts it into mitochondria and restore cytochrome c oxidase (CcO) level in the brain. In animal model, ES-Cu2+ complex could prevent neurodegeneration in cortical and hippocampal neurons and achieve long-term disease control. This study indicates specific drugs are possible to target specific metal ions and deliver them in a specific physiological process for disease treatment. This strategy will also open space for rational design of small molecules to target free metal ions in immune processes for metalloimmunotherapy. Also, metal ions fluorescent probes development also benefits from the rational molecule design. For example, the biological studies of Ca^{2+} in life have greatly benefited the highly specific and sensitive fluorescent probes[7, 185]. For the long term, the development of more sensitive and specific probes of various metal ions may also allow us to real-time monitor the response of metalloimmunotherapies.

5.3. Nanomedicine for precision metalloimmunotherapy

Different from the traditional small molecules-based or macromolecules-based drugs, metal ions are usually less selective because the same metal ion may have many different targets in body and play different roles in different positions. Also, as

essential nutritional or functional components of human body, metal ions are usually finely tuned by inherent mechanisms. Nonselective administration of metal ions may result in physiological balance disorder and potential toxicity. Therefore, appropriate spatial-temporal control of metal ions would greatly accelerate the development of effective and precise metalloimmunotherapies. Nanomedicine, like super small robots, would provide an ideal platform to control metalloimmunotherapy delivery to achieve appropriate spatial-temporal resolution. To this end, the following three aspects should be taken into consideration of nanomedicine metalloimmunotherapy:

1) Material design: numerous metal-containing nanoparticles of various sizes and shapes have been developed over the past decades, such as nanoscale metal-organic frameworks (MOF)[100, 105], nano coordination polymer (NCP)[172, 174], metal-containing nanoprecipitation and various other nanoparticles that could encapsulate or absorb metal ions insides[186-188]. To develop a successful metalloimmunotherapy, appropriate material should be selected or designed based on the metal ion loading efficacy/capacity, stability of metal ions in the particle, release kinetics of metal ions from the particle in different physiological environments, physical properties (like size and shape), and biocompatibility of the nanoparticle.

2) Targeting: nanomedicine could target some specific organ by either passive targeting or active targeting. For passive targeting, the enhanced permeability and retention effect (EPR) could help nanomedicine accumulate in tumor after intravenous (IV) injection and nanomedicine of 5-50nm could effectively home to draining lymph node after subcutaneous injection[189-190]. For active targeting, nanomedicine could be modified with some targeting ligands to achieve targeted delivery of metal ions to specific immune

cells for disease treatment, such as antibody, peptide, aptamer and so on. However, multiple physiological barriers should be overcome for an effective targeted nanomedicine, such as reticuloendothelial system (RES) retention for targets in non-RES organs, Blood-Brain-Barrier (BBB) for central neutral system targets, endosome for intracellular targets, etc.

3) functionalization: nanomedicines could be functionalized with many unique properties to design smarter metalloimmunotherapy. For example, nanomedicine could be endowed with stimuli-responsive properties[191-194]. So they could release therapeutic metal ions on demand in response to environmental stimulation (pH, ROS, enzyme, glucose, etc) and artificial stimulation (light, X-ray, temperature, ultrasound, magnetic field, etc). Some nanomedicines could also be functionalized with imaging properties to allow for imaging-guided therapy. Moreover, some nanomedicines could co-deliver multiple drugs together with metal ions for synergistic therapy. Some metal-containing nanomedicines were reported to have catalytic properties and x-ray sensitizer properties[105, 195].

Overall, metalloimmunotherapy represents a paradigm shift of metallodrug development and I hope this dissertation would inspire more scientists to explore this exciting area. Furthermore, even though cancer immunotherapy is mainly discussed in this dissertation, the scope of indications of metalloimmunotherapy is not limited to cancer. As nutritional metal ions play crucial roles in various immune processes, the potential of metalloimmunotherapy as a novel strategy for treating other immune-related diseases should also be explored.

References

1. Partington, J. R., An Ancient Chinese Treatise on Alchemy. *Nature* **1935,** *136* (3434), 287-288.
2. Hambley, T. W., Chemistry. Metal-based therapeutics. *Science* **2007,** *318* (5855), 1392-3.
3. Thompson, K. H.; Orvig, C., Boon and bane of metal ions in medicine. *Science* **2003,** *300* (5621), 936-9.
4. Rosenberg, B.; VanCamp, L.; Trosko, J. E.; Mansour, V. H., Platinum compounds: a new class of potent antitumour agents. *Nature* **1969,** *222* (5191), 385-6.
5. Rosenberg, B.; Vancamp, L.; Krigas, T., Inhibition of Cell Division in Escherichia Coli by Electrolysis Products from a Platinum Electrode. *Nature* **1965,** *205*, 698-9.
6. Chaigne-Delalande, B.; Lenardo, M. J., Divalent cation signaling in immune cells. *Trends Immunol* **2014,** *35* (7), 332-44.
7. Wang, C.; Zhang, R.; Wei, X.; Lv, M.; Jiang, Z., Metalloimmunology: The metal ion-controlled immunity. *Adv Immunol* **2020,** *145*, 187-241.
8. Vodnala, S. K.; Eil, R.; Kishton, R. J.; Sukumar, M.; Yamamoto, T. N.; Ha, N. H.; Lee, P. H.; Shin, M.; Patel, S. J.; Yu, Z.; Palmer, D. C.; Kruhlak, M. J.; Liu, X.; Locasale, J. W.; Huang, J.; Roychoudhuri, R.; Finkel, T.; Klebanoff, C. A.; Restifo, N. P., T cell stemness and dysfunction in tumors are triggered by a common mechanism. *Science* **2019,** *363* (6434).
9. Chandy, K. G.; Norton, R. S., Immunology: Channelling potassium to fight cancer. *Nature* **2016,** *537* (7621), 497-499.
10. Shi, X.; Bi, Y.; Yang, W.; Guo, X.; Jiang, Y.; Wan, C.; Li, L.; Bai, Y.; Guo, J.; Wang, Y.; Chen, X.; Wu, B.; Sun, H.; Liu, W.; Wang, J.; Xu, C., Ca2+ regulates T-cell receptor activation by modulating the charge property of lipids. *Nature* **2013,** *493* (7430), 111-5.
11. Macian, F., NFAT proteins: key regulators of T-cell development and function. *Nat Rev Immunol* **2005,** *5* (6), 472-84.
12. Rossol, M.; Pierer, M.; Raulien, N.; Quandt, D.; Meusch, U.; Rothe, K.; Schubert, K.; Schoneberg, T.; Schaefer, M.; Krugel, U.; Smajilovic, S.; Brauner-Osborne, H.; Baerwald, C.; Wagner, U., Extracellular Ca2+ is a danger signal activating the NLRP3 inflammasome through G protein-coupled calcium sensing receptors. *Nat Commun* **2012,** *3*, 1329.
13. Munoz-Planillo, R.; Kuffa, P.; Martinez-Colon, G.; Smith, B. L.; Rajendiran, T. M.; Nunez, G., K(+) efflux is the common trigger of NLRP3 inflammasome activation by bacterial toxins and particulate matter. *Immunity* **2013,** *38* (6), 1142-53.
14. Scambler, T.; Jarosz-Griffiths, H. H.; Lara-Reyna, S.; Pathak, S.; Wong, C.; Holbrook, J.; Martinon, F.; Savic, S.; Peckham, D.; McDermott, M. F., ENaC-mediated sodium influx exacerbates NLRP3-dependent inflammation in cystic fibrosis. *Elife* **2019,** *8*.
15. Wang, C.; Guan, Y.; Lv, M.; Zhang, R.; Guo, Z.; Wei, X.; Du, X.; Yang, J.; Li, T.; Wan, Y., Manganese increases the sensitivity of the cGAS-STING pathway for double-stranded DNA and is required for the host defense against DNA viruses. *Immunity* **2018,** *48* (4), 675-687. e7.
16. Ahn, J.; Barber, G. N., STING signaling and host defense against microbial infection. *Experimental & Molecular Medicine* **2019,** *51* (12), 1-10.
17. Takeuchi, O.; Akira, S., Pattern Recognition Receptors and Inflammation. *Cell* **2010,** *140* (6), 805-820.
18. Schmidt, M.; Raghavan, B.; Müller, V.; Vogl, T.; Fejer, G.; Tchaptchet, S.; Keck, S.; Kalis, C.; Nielsen, P. J.; Galanos, C.; Roth, J.; Skerra, A.; Martin, S. F.; Freudenberg, M. A.; Goebeler, M., Crucial role for human Toll-like receptor 4 in the development of contact allergy to nickel. *Nature Immunology* **2010,** *11* (9), 814-819.

19. Anjum, S. A.; Lawrence, H.; Holland, J. P.; Kirby, J. A.; Deehan, D. J.; Tyson-Capper, A. J., Effect of cobalt-mediated Toll-like receptor 4 activation on inflammatory responses in endothelial cells. *Oncotarget; Vol 7, No 47* **2016**.
20. Liu, J.-T.; Chen, B.-Y.; Zhang, J.-Q.; Kuang, F.; Chen, L.-W., Lead exposure induced microgliosis and astrogliosis in hippocampus of young mice potentially by triggering TLR4–MyD88–NFκB signaling cascades. *Toxicology Letters* **2015,** *239* (2), 97-107.
21. Dutra, F. F.; Bozza, M. T., Heme on innate immunity and inflammation. *Frontiers in Pharmacology* **2014,** *5* (115).
22. Goebeler, M.; Roth, J.; Bröcker, E. B.; Sorg, C.; Schulze-Osthoff, K., Activation of nuclear factor-kappa B and gene expression in human endothelial cells by the common haptens nickel and cobalt. *The Journal of Immunology* **1995,** *155* (5), 2459.
23. She, H.; Xiong, S.; Lin, M.; Zandi, E.; Giulivi, C.; Tsukamoto, H., Iron activates NF-κB in Kupffer cells. *American Journal of Physiology-Gastrointestinal and Liver Physiology* **2002,** *283* (3), G719-G726.
24. Altura, B. M.; Kostellow, A. B.; Zhang, A.; Li, W.; Morrill, G. A.; Gupta, R. K.; Altura, B. T., Expression of the nuclear factor-κB and proto-oncogenes c-Fos and c-Jun are induced by low extracellular mg2+ in aortic and cerebral vascular smooth muscle cells: possible links to hypertension, atherogenesis, and stroke. *American Journal of Hypertension* **2003,** *16* (9), 701-707.
25. Liu, M.-J.; Bao, S.; Gálvez-Peralta, M.; Pyle, Charlie J.; Rudawsky, Andrew C.; Pavlovicz, Ryan E.; Killilea, David W.; Li, C.; Nebert, Daniel W.; Wewers, Mark D.; Knoell, Daren L., ZIP8 Regulates Host Defense through Zinc-Mediated Inhibition of NF-κB. *Cell Reports* **2013,** *3* (2), 386-400.
26. Martinon, F.; Burns, K.; Tschopp, J., The Inflammasome: A Molecular Platform Triggering Activation of Inflammatory Caspases and Processing of proIL-β. *Molecular Cell* **2002,** *10* (2), 417-426.
27. Mariathasan, S.; Monack, D. M., Inflammasome adaptors and sensors: intracellular regulators of infection and inflammation. *Nature Reviews Immunology* **2007,** *7* (1), 31-40.
28. Martinon, F.; Pétrilli, V.; Mayor, A.; Tardivel, A.; Tschopp, J., Gout-associated uric acid crystals activate the NALP3 inflammasome. *Nature* **2006,** *440* (7081), 237-241.
29. Eisenbarth, S. C.; Colegio, O. R.; O'Connor, W.; Sutterwala, F. S.; Flavell, R. A., Crucial role for the Nalp3 inflammasome in the immunostimulatory properties of aluminium adjuvants. *Nature* **2008,** *453* (7198), 1122-1126.
30. Hornung, V.; Bauernfeind, F.; Halle, A.; Samstad, E. O.; Kono, H.; Rock, K. L.; Fitzgerald, K. A.; Latz, E., Silica crystals and aluminum salts activate the NALP3 inflammasome through phagosomal destabilization. *Nature immunology* **2008,** *9* (8), 847.
31. Summersgill, H.; England, H.; Lopez-Castejon, G.; Lawrence, C. B.; Luheshi, N. M.; Pahle, J.; Mendes, P.; Brough, D., Zinc depletion regulates the processing and secretion of IL-1β. *Cell Death & Disease* **2014,** *5* (1), e1040-e1040.
32. Zhou, R.; Yazdi, A. S.; Menu, P.; Tschopp, J., A role for mitochondria in NLRP3 inflammasome activation. *Nature* **2011,** *469* (7329), 221-225.
33. Sarkar, S.; Rokad, D.; Malovic, E.; Luo, J.; Harischandra, D. S.; Jin, H.; Anantharam, V.; Huang, X.; Lewis, M.; Kanthasamy, A.; Kanthasamy, A. G., Manganese activates NLRP3 inflammasome signaling and propagates exosomal release of ASC in microglial cells. *Science Signaling* **2019,** *12* (563), eaat9900.
34. Guo, H.; Liu, H.; Jian, Z.; Cui, H.; Fang, J.; Zuo, Z.; Deng, J.; Li, Y.; Wang, X.; Zhao, L.; Geng, Y.; Ouyang, P.; Lai, W.; Chen, Z.; Huang, C., Nickel induces inflammatory activation via NF-κB, MAPKs, IRF3 and NLRP3 inflammasome signaling pathways in macrophages. *Aging* **2019,** *11* (23), 11659-11672.
35. Ip, W. K. E.; Medzhitov, R., Macrophages monitor tissue osmolarity and induce inflammatory response through NLRP3 and NLRC4 inflammasome activation. *Nature Communications* **2015,** *6* (1), 6931.
36. Lee, G.-S.; Subramanian, N.; Kim, A. I.; Aksentijevich, I.; Goldbach-Mansky, R.; Sacks, D. B.; Germain, R. N.; Kastner, D. L.; Chae, J. J., The calcium-sensing receptor regulates the NLRP3 inflammasome through Ca2+ and cAMP. *Nature* **2012,** *492* (7427), 123-127.
37. Pétrilli, V.; Papin, S.; Dostert, C.; Mayor, A.; Martinon, F.; Tschopp, J., Activation of the NALP3 inflammasome is triggered by low intracellular potassium concentration. *Cell Death & Differentiation* **2007,** *14* (9), 1583-1589.
38. Compan, V.; Baroja-Mazo, A.; López-Castejón, G.; Gomez, Ana I.; Martínez, Carlos M.; Angosto, D.; Montero, María T.; Herranz, Antonio S.; Bazán, E.; Reimers, D.; Mulero, V.; Pelegrín, P., Cell Volume Regulation Modulates NLRP3 Inflammasome Activation. *Immunity* **2012,** *37* (3), 487-500.

39. Ishikawa, H.; Ma, Z.; Barber, G. N., STING regulates intracellular DNA-mediated, type I interferon-dependent innate immunity. *Nature* **2009,** *461* (7265), 788-792.
40. Burdette, D. L.; Monroe, K. M.; Sotelo-Troha, K.; Iwig, J. S.; Eckert, B.; Hyodo, M.; Hayakawa, Y.; Vance, R. E., STING is a direct innate immune sensor of cyclic di-GMP. *Nature* **2011,** *478* (7370), 515-518.
41. Wu, J.; Sun, L.; Chen, X.; Du, F.; Shi, H.; Chen, C.; Chen, Z. J., Cyclic GMP-AMP is an endogenous second messenger in innate immune signaling by cytosolic DNA. *Science* **2013,** *339* (6121), 826-830.
42. Gao, P.; Ascano, M.; Wu, Y.; Barchet, W.; Gaffney, Barbara L.; Zillinger, T.; Serganov, Artem A.; Liu, Y.; Jones, Roger A.; Hartmann, G.; Tuschl, T.; Patel, Dinshaw J., Cyclic [G(2′,5′)pA(3′,5′)p] Is the Metazoan Second Messenger Produced by DNA-Activated Cyclic GMP-AMP Synthase. *Cell* **2013,** *153* (5), 1094-1107.
43. Wang, C.; Guan, Y.; Lv, M.; Zhang, R.; Guo, Z.; Wei, X.; Du, X.; Yang, J.; Li, T.; Wan, Y.; Su, X.; Huang, X.; Jiang, Z., Manganese Increases the Sensitivity of the cGAS-STING Pathway for Double-Stranded DNA and Is Required for the Host Defense against DNA Viruses. *Immunity* **2018,** *48* (4), 675-687.e7.
44. Zhao, Z.; Ma, Z.; Wang, B.; Guan, Y.; Su, X.-D.; Jiang, Z., Mn2+ Directly Activates cGAS and Structural Analysis Suggests Mn2+ Induces a Noncanonical Catalytic Synthesis of 2′3′-cGAMP. *Cell Reports* **2020,** *32* (7), 108053.
45. Du, M.; Chen, Z. J., DNA-induced liquid phase condensation of cGAS activates innate immune signaling. *Science* **2018,** *361* (6403), 704.
46. Liu, Y.-P.; Zeng, L.; Tian, A.; Bomkamp, A.; Rivera, D.; Gutman, D.; Barber, G. N.; Olson, J. K.; Smith, J. A., Endoplasmic Reticulum Stress Regulates the Innate Immunity Critical Transcription Factor IRF3. *The Journal of Immunology* **2012,** *189* (9), 4630.
47. Banerjee, I.; Behl, B.; Mendonca, M.; Shrivastava, G.; Russo, A. J.; Menoret, A.; Ghosh, A.; Vella, A. T.; Vanaja, S. K.; Sarkar, S. N.; Fitzgerald, K. A.; Rathinam, V. A. K., Gasdermin D Restrains Type I Interferon Response to Cytosolic DNA by Disrupting Ionic Homeostasis. *Immunity* **2018,** *49* (3), 413-426.e5.
48. Smith-Garvin, J. E.; Koretzky, G. A.; Jordan, M. S., T cell activation. *Annual review of immunology* **2009,** *27*, 591-619.
49. Palacios, E. H.; Weiss, A., Function of the Src-family kinases, Lck and Fyn, in T-cell development and activation. *Oncogene* **2004,** *23* (48), 7990-8000.
50. Weiss, A.; Littman, D. R., Signal transduction by lymphocyte antigen receptors. *Cell* **1994,** *76* (2), 263-274.
51. Shi, X.; Bi, Y.; Yang, W.; Guo, X.; Jiang, Y.; Wan, C.; Li, L.; Bai, Y.; Guo, J.; Wang, Y.; Chen, X.; Wu, B.; Sun, H.; Liu, W.; Wang, J.; Xu, C., Ca2+ regulates T-cell receptor activation by modulating the charge property of lipids. *Nature* **2013,** *493* (7430), 111-115.
52. Macian, F., NFAT proteins: key regulators of T-cell development and function. *Nature Reviews Immunology* **2005,** *5* (6), 472-484.
53. Verma, S.; Hoffmann, F. W.; Kumar, M.; Huang, Z.; Roe, K.; Nguyen-Wu, E.; Hashimoto, A. S.; Hoffmann, P. R., Selenoprotein K Knockout Mice Exhibit Deficient Calcium Flux in Immune Cells and Impaired Immune Responses. *The Journal of Immunology* **2011,** *186* (4), 2127.
54. Li, F.-Y.; Chaigne-Delalande, B.; Kanellopoulou, C.; Davis, J. C.; Matthews, H. F.; Douek, D. C.; Cohen, J. I.; Uzel, G.; Su, H. C.; Lenardo, M. J., Second messenger role for Mg2+ revealed by human T-cell immunodeficiency. *Nature* **2011,** *475* (7357), 471-476.
55. Chaigne-Delalande, B.; Li, F.-Y.; O'Connor, G. M.; Lukacs, M. J.; Jiang, P.; Zheng, L.; Shatzer, A.; Biancalana, M.; Pittaluga, S.; Matthews, H. F.; Jancel, T. J.; Bleesing, J. J.; Marsh, R. A.; Kuijpers, T. W.; Nichols, K. E.; Lucas, C. L.; Nagpal, S.; Mehmet, H.; Su, H. C.; Cohen, J. I.; Uzel, G.; Lenardo, M. J., Mg²⁺ Regulates Cytotoxic Functions of NK and CD8 T Cells in Chronic EBV Infection Through NKG2D. *Science* **2013,** *341* (6142), 186.
56. Kanellopoulou, C.; George, A. B.; Masutani, E.; Cannons, J. L.; Ravell, J. C.; Yamamoto, T. N.; Smelkinson, M. G.; Jiang, P. D.; Matsuda-Lennikov, M.; Reilley, J.; Handon, R.; Lee, P.-H.; Miller, J. R.; Restifo, N. P.; Zheng, L.; Schwartzberg, P. L.; Young, M.; Lenardo, M. J., Mg2+ regulation of kinase signaling and immune function. *Journal of Experimental Medicine* **2019,** *216* (8), 1828-1842.
57. Huang, J.; Zhang, D.; Xing, W.; Ma, X.; Yin, Y.; Wei, Q.; Li, G., An approach to assay calcineurin activity and the inhibitory effect of zinc ion. *Analytical Biochemistry* **2008,** *375* (2), 385-387.

58. Kim, P. W.; Sun, Z.-Y. J.; Blacklow, S. C.; Wagner, G.; Eck, M. J., A Zinc Clasp Structure Tethers Lck to T Cell Coreceptors CD4 and CD8. *Science* **2003,** *301* (5640), 1725.
59. Eil, R.; Vodnala, S. K.; Clever, D.; Klebanoff, C. A.; Sukumar, M.; Pan, J. H.; Palmer, D. C.; Gros, A.; Yamamoto, T. N.; Patel, S. J.; Guittard, G. C.; Yu, Z.; Carbonaro, V.; Okkenhaug, K.; Schrump, D. S.; Linehan, W. M.; Roychoudhuri, R.; Restifo, N. P., Ionic immune suppression within the tumour microenvironment limits T cell effector function. *Nature* **2016,** *537* (7621), 539-543.
60. Vodnala, S. K.; Eil, R.; Kishton, R. J.; Sukumar, M.; Yamamoto, T. N.; Ha, N.-H.; Lee, P.-H.; Shin, M.; Patel, S. J.; Yu, Z.; Palmer, D. C.; Kruhlak, M. J.; Liu, X.; Locasale, J. W.; Huang, J.; Roychoudhuri, R.; Finkel, T.; Klebanoff, C. A.; Restifo, N. P., T cell stemness and dysfunction in tumors are triggered by a common mechanism. *Science* **2019,** *363* (6434), eaau0135.
61. Wu, C.; Yosef, N.; Thalhamer, T.; Zhu, C.; Xiao, S.; Kishi, Y.; Regev, A.; Kuchroo, V. K., Induction of pathogenic TH17 cells by inducible salt-sensing kinase SGK1. *Nature* **2013,** *496* (7446), 513-517.
62. Hernandez, A. L.; Kitz, A.; Wu, C.; Lowther, D. E.; Rodriguez, D. M.; Vudattu, N.; Deng, S.; Herold, K. C.; Kuchroo, V. K.; Kleinewietfeld, M.; Hafler, D. A., Sodium chloride inhibits the suppressive function of FOXP3+ regulatory T cells. *The Journal of Clinical Investigation* **2015,** *125* (11), 4212-4222.
63. Sender, R.; Fuchs, S.; Milo, R., Are We Really Vastly Outnumbered? Revisiting the Ratio of Bacterial to Host Cells in Humans. *Cell* **2016,** *164* (3), 337-340.
64. Turnbaugh, P. J.; Ley, R. E.; Hamady, M.; Fraser-Liggett, C. M.; Knight, R.; Gordon, J. I., The Human Microbiome Project. *Nature* **2007,** *449* (7164), 804-810.
65. Fan, Y.; Pedersen, O., Gut microbiota in human metabolic health and disease. *Nature Reviews Microbiology* **2020**.
66. Zheng, D.; Liwinski, T.; Elinav, E., Interaction between microbiota and immunity in health and disease. *Cell Research* **2020,** *30* (6), 492-506.
67. Belkaid, Y.; Hand, Timothy W., Role of the Microbiota in Immunity and Inflammation. *Cell* **2014,** *157* (1), 121-141.
68. Mager, L. F.; Burkhard, R.; Pett, N.; Cooke, N. C. A.; Brown, K.; Ramay, H.; Paik, S.; Stagg, J.; Groves, R. A.; Gallo, M.; Lewis, I. A.; Geuking, M. B.; McCoy, K. D., Microbiome-derived inosine modulates response to checkpoint inhibitor immunotherapy. *Science* **2020,** *369* (6510), 1481.
69. Bachem, A.; Makhlouf, C.; Binger, K. J.; de Souza, D. P.; Tull, D.; Hochheiser, K.; Whitney, P. G.; Fernandez-Ruiz, D.; Dähling, S.; Kastenmüller, W.; Jönsson, J.; Gressier, E.; Lew, A. M.; Perdomo, C.; Kupz, A.; Figgett, W.; Mackay, F.; Oleshansky, M.; Russ, B. E.; Parish, I. A.; Kallies, A.; McConville, M. J.; Turner, S. J.; Gebhardt, T.; Bedoui, S., Microbiota-Derived Short-Chain Fatty Acids Promote the Memory Potential of Antigen-Activated CD8+ T Cells. *Immunity* **2019,** *51* (2), 285-297.e5.
70. Arpaia, N.; Campbell, C.; Fan, X.; Dikiy, S.; van der Veeken, J.; deRoos, P.; Liu, H.; Cross, J. R.; Pfeffer, K.; Coffer, P. J.; Rudensky, A. Y., Metabolites produced by commensal bacteria promote peripheral regulatory T-cell generation. *Nature* **2013,** *504* (7480), 451-455.
71. Hood, M. I.; Skaar, E. P., Nutritional immunity: transition metals at the pathogen–host interface. *Nature Reviews Microbiology* **2012,** *10* (8), 525-537.
72. Forbes, J. R.; Gros, P., Iron, manganese, and cobalt transport by Nramp1 (Slc11a1) and Nramp2 (Slc11a2) expressed at the plasma membrane. *Blood* **2003,** *102* (5), 1884-1892.
73. Posey, J. E.; Gherardini, F. C., Lack of a Role for Iron in the Lyme Disease Pathogen. *Science* **2000,** *288* (5471), 1651.
74. Schalk, I. J., Metal trafficking via siderophores in Gram-negative bacteria: specificities and characteristics of the pyoverdine pathway. *Journal of inorganic biochemistry* **2008,** *102* (5-6), 1159-1169.
75. Flo, T. H.; Smith, K. D.; Sato, S.; Rodriguez, D. J.; Holmes, M. A.; Strong, R. K.; Akira, S.; Aderem, A., Lipocalin 2 mediates an innate immune response to bacterial infection by sequestrating iron. *Nature* **2004,** *432* (7019), 917-921.
76. Honsa, E. S.; Maresso, A. W., Mechanisms of iron import in anthrax. *BioMetals* **2011,** *24* (3), 533-545.
77. Kehl-Fie, T. E.; Skaar, E. P., Nutritional immunity beyond iron: a role for manganese and zinc. *Current opinion in chemical biology* **2010,** *14* (2), 218-224.
78. Corbin, B. D.; Seeley, E. H.; Raab, A.; Feldmann, J.; Miller, M. R.; Torres, V. J.; Anderson, K. L.; Dattilo, B. M.; Dunman, P. M.; Gerads, R.; Caprioli, R. M.; Nacken, W.; Chazin, W. J.; Skaar, E. P., Metal Chelation and Inhibition of Bacterial Growth in Tissue Abscesses. *Science* **2008,** *319* (5865), 962.
79. Botella, H.; Peyron, P.; Levillain, F.; Poincloux, R.; Poquet, Y.; Brandli, I.; Wang, C.; Tailleux, L.; Tilleul, S.; Charrière, G. M.; Waddell, Simon J.; Foti, M.; Lugo-Villarino, G.; Gao, Q.; Maridonneau-Parini,

I.; Butcher, Philip D.; Castagnoli, Paola R.; Gicquel, B.; de Chastellier, C.; Neyrolles, O., Mycobacterial P1-Type ATPases Mediate Resistance to Zinc Poisoning in Human Macrophages. *Cell Host & Microbe* **2011,** *10* (3), 248-259.
80. He, P.; Zou, Y.; Hu, Z., Advances in aluminum hydroxide-based adjuvant research and its mechanism. *Hum Vaccin Immunother* **2015,** *11* (2), 477-88.
81. Eisenbarth, S. C.; Colegio, O. R.; O'Connor, W.; Sutterwala, F. S.; Flavell, R. A., Crucial role for the Nalp3 inflammasome in the immunostimulatory properties of aluminium adjuvants. *Nature* **2008,** *453* (7198), 1122-6.
82. Masson, J. D.; Thibaudon, M.; Belec, L.; Crepeaux, G., Calcium phosphate: a substitute for aluminum adjuvants? *Expert Rev Vaccines* **2017,** *16* (3), 289-299.
83. Bhakta, G.; Nurcombe, V.; Maitra, A.; Shrivastava, A., DNA-encapsulated magnesium phosphate nanoparticles elicit both humoral and cellular immune responses in mice. *Results Immunol* **2014,** *4*, 46-53.
84. Marques Neto, L. M.; Kipnis, A.; Junqueira-Kipnis, A. P., Role of Metallic Nanoparticles in Vaccinology: Implications for Infectious Disease Vaccine Development. *Front Immunol* **2017,** *8*, 239.
85. Zhang, R.; Wang, C.; Guan, Y.; Wei, X.; Sha, M.; Yi, M.; Jing, M.; Lv, M.; Guo, W.; Xu, J.; Wan, Y.; Jia, X. M.; Jiang, Z., Manganese salts function as potent adjuvants. *Cell Mol Immunol* **2021,** *18* (5), 1222-1234.
86. Li, F. Y.; Chaigne-Delalande, B.; Kanellopoulou, C.; Davis, J. C.; Matthews, H. F.; Douek, D. C.; Cohen, J. I.; Uzel, G.; Su, H. C.; Lenardo, M. J., Second messenger role for Mg2+ revealed by human T-cell immunodeficiency. *Nature* **2011,** *475* (7357), 471-6.
87. Chaigne-Delalande, B.; Li, F. Y.; O'Connor, G. M.; Lukacs, M. J.; Jiang, P.; Zheng, L.; Shatzer, A.; Biancalana, M.; Pittaluga, S.; Matthews, H. F.; Jancel, T. J.; Bleesing, J. J.; Marsh, R. A.; Kuijpers, T. W.; Nichols, K. E.; Lucas, C. L.; Nagpal, S.; Mehmet, H.; Su, H. C.; Cohen, J. I.; Uzel, G.; Lenardo, M. J., Mg2+ regulates cytotoxic functions of NK and CD8 T cells in chronic EBV infection through NKG2D. *Science* **2013,** *341* (6142), 186-91.
88. Kurugol, Z.; Akilli, M.; Bayram, N.; Koturoglu, G., The prophylactic and therapeutic effectiveness of zinc sulphate on common cold in children. *Acta Paediatr* **2006,** *95* (10), 1175-81.
89. Read, S. A.; Obeid, S.; Ahlenstiel, C.; Ahlenstiel, G., The Role of Zinc in Antiviral Immunity. *Adv Nutr* **2019,** *10* (4), 696-710.
90. Baum, M. K.; Shor-Posner, G.; Campa, A., Zinc status in human immunodeficiency virus infection. *J Nutr* **2000,** *130* (5S Suppl), 1421S-3S.
91. Rafiq, S.; Hackett, C. S.; Brentjens, R. J., Engineering strategies to overcome the current roadblocks in CAR T cell therapy. *Nat Rev Clin Oncol* **2020,** *17* (3), 147-167.
92. Lv, M.; Chen, M.; Zhang, R.; Zhang, W.; Wang, C.; Zhang, Y.; Wei, X.; Guan, Y.; Liu, J.; Feng, K.; Jing, M.; Wang, X.; Liu, Y. C.; Mei, Q.; Han, W.; Jiang, Z., Manganese is critical for antitumor immune responses via cGAS-STING and improves the efficacy of clinical immunotherapy. *Cell Res* **2020,** *30* (11), 966-979.
93. Ahmed, A.; Tait, S. W. G., Targeting immunogenic cell death in cancer. *Mol Oncol* **2020,** *14* (12), 2994-3006.
94. Englinger, B.; Pirker, C.; Heffeter, P.; Terenzi, A.; Kowol, C. R.; Keppler, B. K.; Berger, W., Metal Drugs and the Anticancer Immune Response. *Chem Rev* **2019,** *119* (2), 1519-1624.
95. Wang, L.; Guan, R.; Xie, L.; Liao, X.; Xiong, K.; Rees, T. W.; Chen, Y.; Ji, L.; Chao, H., An ER-Targeting Iridium(III) Complex That Induces Immunogenic Cell Death in Non-Small-Cell Lung Cancer. *Angew Chem Int Ed Engl* **2021,** *60* (9), 4657-4665.
96. Wernitznig, D.; Kiakos, K.; Del Favero, G.; Harrer, N.; Machat, H.; Osswald, A.; Jakupec, M. A.; Wernitznig, A.; Sommergruber, W.; Keppler, B. K., First-in-class ruthenium anticancer drug (KP1339/IT-139) induces an immunogenic cell death signature in colorectal spheroids in vitro. *Metallomics* **2019,** *11* (6), 1044-1048.
97. Kaur, P.; Johnson, A.; Northcote-Smith, J.; Lu, C.; Suntharalingam, K., Immunogenic Cell Death of Breast Cancer Stem Cells Induced by an Endoplasmic Reticulum-Targeting Copper(II) Complex. *Chembiochem* **2020,** *21* (24), 3618-3624.
98. Tang, R.; Xu, J.; Zhang, B.; Liu, J.; Liang, C.; Hua, J.; Meng, Q.; Yu, X.; Shi, S., Ferroptosis, necroptosis, and pyroptosis in anticancer immunity. *J Hematol Oncol* **2020,** *13* (1), 110.

99. Zheng, D. W.; Lei, Q.; Zhu, J. Y.; Fan, J. X.; Li, C. X.; Li, C.; Xu, Z.; Cheng, S. X.; Zhang, X. Z., Switching Apoptosis to Ferroptosis: Metal-Organic Network for High-Efficiency Anticancer Therapy. *Nano Lett* **2017,** *17* (1), 284-291.
100. Yang, J.; Ma, S.; Xu, R.; Wei, Y.; Zhang, J.; Zuo, T.; Wang, Z.; Deng, H.; Yang, N.; Shen, Q., Smart biomimetic metal organic frameworks based on ROS-ferroptosis-glycolysis regulation for enhanced tumor chemo-immunotherapy. *J Control Release* **2021,** *334*, 21-33.
101. Tang, Z. M.; Liu, Y. Y.; Ni, D. L.; Zhou, J. J.; Zhang, M.; Zhao, P. R.; Lv, B.; Wang, H.; Jin, D. Y.; Bu, W. B., Biodegradable Nanoprodrugs: "Delivering" ROS to Cancer Cells for Molecular Dynamic Therapy. *Adv Mater* **2020,** *32* (4), e1904011.
102. Xiong, K.; Qian, C.; Yuan, Y.; Wei, L.; Liao, X.; He, L.; Rees, T. W.; Chen, Y.; Wan, J.; Ji, L.; Chao, H., Necroptosis Induced by Ruthenium(II) Complexes as Dual Catalytic Inhibitors of Topoisomerase I/II. *Angew Chem Int Ed Engl* **2020,** *59* (38), 16631-16637.
103. Yu, P.; Zhang, X.; Liu, N.; Tang, L.; Peng, C.; Chen, X., Pyroptosis: mechanisms and diseases. *Signal Transduct Target Ther* **2021,** *6* (1), 128.
104. Zhou, B.; Zhang, J. Y.; Liu, X. S.; Chen, H. Z.; Ai, Y. L.; Cheng, K.; Sun, R. Y.; Zhou, D.; Han, J.; Wu, Q., Tom20 senses iron-activated ROS signaling to promote melanoma cell pyroptosis. *Cell Res* **2018,** *28* (12), 1171-1185.
105. Ni, K.; Lan, G.; Lin, W., Nanoscale Metal-Organic Frameworks Generate Reactive Oxygen Species for Cancer Therapy. *ACS Cent Sci* **2020,** *6* (6), 861-868.
106. Lau, H.; Khosrawipour, V.; Kocbach, P.; Mikolajczyk, A.; Ichii, H.; Zacharski, M.; Bania, J.; Khosrawipour, T., The association between international and domestic air traffic and the coronavirus (COVID-19) outbreak. *J Microbiol Immunol Infect* **2020,** *53* (3), 467-472.
107. Wan, Y.; Shang, J.; Graham, R.; Baric, R. S.; Li, F., Receptor Recognition by the Novel Coronavirus from Wuhan: an Analysis Based on Decade-Long Structural Studies of SARS Coronavirus. *J Virol* **2020,** *94* (7).
108. Tang, T.; Bidon, M.; Jaimes, J. A.; Whittaker, G. R.; Daniel, S., Coronavirus membrane fusion mechanism offers a potential target for antiviral development. *Antiviral Res* **2020,** *178*, 104792.
109. van Riel, D.; de Wit, E., Next-generation vaccine platforms for COVID-19. *Nat Mater* **2020,** *19* (8), 810-812.
110. Park, K. S.; Sun, X.; Aikins, M. E.; Moon, J. J., Non-viral COVID-19 vaccine delivery systems. *Adv Drug Deliv Rev* **2021,** *169*, 137-151.
111. Du, L.; He, Y.; Zhou, Y.; Liu, S.; Zheng, B. J.; Jiang, S., The spike protein of SARS-CoV--a target for vaccine and therapeutic development. *Nat Rev Microbiol* **2009,** *7* (3), 226-36.
112. Walls, A. C.; Park, Y. J.; Tortorici, M. A.; Wall, A.; McGuire, A. T.; Veesler, D., Structure, Function, and Antigenicity of the SARS-CoV-2 Spike Glycoprotein. *Cell* **2020,** *181* (2), 281-292.e6.
113. Tian, J.-H.; Patel, N.; Haupt, R.; Zhou, H.; Weston, S.; Hammond, H.; Lague, J.; Portnoff, A. D.; Norton, J.; Guebre-Xabier, M., SARS-CoV-2 spike glycoprotein vaccine candidate NVX-CoV2373 elicits immunogenicity in baboons and protection in mice. *BioRxiv* **2020**.
114. Bangaru, S.; Ozorowski, G.; Turner, H. L.; Antanasijevic, A.; Huang, D.; Wang, X.; Torres, J. L.; Diedrich, J. K.; Tian, J.-H.; Portnoff, A. D., Structural analysis of full-length SARS-CoV-2 spike protein from an advanced vaccine candidate. *BioRxiv* **2020**.
115. Magnusson, S. E.; Reimer, J. M.; Karlsson, K. H.; Lilja, L.; Bengtsson, K. L.; Stertman, L., Immune enhancing properties of the novel Matrix-M™ adjuvant leads to potentiated immune responses to an influenza vaccine in mice. *Vaccine* **2013,** *31* (13), 1725-33.
116. Keech, C.; Albert, G.; Reed, P.; Neal, S.; Plested, J. S.; Zhu, M.; Cloney-Clark, S.; Zhou, H.; Patel, N.; Frieman, M. B., First-in-Human Trial of a SARS CoV 2 Recombinant Spike Protein Nanoparticle Vaccine. *medRxiv* **2020**.
117. Garçon, N.; Vaughn, D. W.; Didierlaurent, A. M., Development and evaluation of AS03, an Adjuvant System containing α-tocopherol and squalene in an oil-in-water emulsion. *Expert Rev Vaccines* **2012,** *11* (3), 349-66.
118. O'Hagan, D. T.; Ott, G. S.; Nest, G. V.; Rappuoli, R.; Giudice, G. D., The history of MF59(®) adjuvant: a phoenix that arose from the ashes. *Expert Rev Vaccines* **2013,** *12* (1), 13-30.
119. Campbell, J. D., Development of the CpG Adjuvant 1018: A Case Study. *Methods Mol Biol* **2017,** *1494*, 15-27.
120. Kasturi, S. P.; Rasheed, M. A. U.; Havenar-Daughton, C.; Pham, M.; Legere, T.; Sher, Z. J.; Kovalenkov, Y.; Gumber, S.; Huang, J. Y.; Gottardo, R.; Fulp, W.; Sato, A.; Sawant, S.; Stanfield-Oakley,

S.; Yates, N.; LaBranche, C.; Alam, S. M.; Tomaras, G.; Ferrari, G.; Montefiori, D.; Wrammert, J.; Villinger, F.; Tomai, M.; Vasilakos, J.; Fox, C. B.; Reed, S. G.; Haynes, B. F.; Crotty, S.; Ahmed, R.; Pulendran, B., 3M-052, a synthetic TLR-7/8 agonist, induces durable HIV-1 envelope-specific plasma cells and humoral immunity in nonhuman primates. *Sci Immunol* **2020,** *5* (48).
121. Dowling, D. J., Recent Advances in the Discovery and Delivery of TLR7/8 Agonists as Vaccine Adjuvants. *Immunohorizons* **2018,** *2* (6), 185-197.
122. Moon, J. J.; Suh, H.; Bershteyn, A.; Stephan, M. T.; Liu, H.; Huang, B.; Sohail, M.; Luo, S.; Um, S. H.; Khant, H.; Goodwin, J. T.; Ramos, J.; Chiu, W.; Irvine, D. J., Interbilayer-crosslinked multilamellar vesicles as synthetic vaccines for potent humoral and cellular immune responses. *Nat Mater* **2011,** *10* (3), 243-51.
123. Knuschke, T.; Sokolova, V.; Rotan, O.; Wadwa, M.; Tenbusch, M.; Hansen, W.; Staeheli, P.; Epple, M.; Buer, J.; Westendorf, A. M., Immunization with biodegradable nanoparticles efficiently induces cellular immunity and protects against influenza virus infection. *J Immunol* **2013,** *190* (12), 6221-9.
124. Heße, C.; Kollenda, S.; Rotan, O.; Pastille, E.; Adamczyk, A.; Wenzek, C.; Hansen, W.; Epple, M.; Buer, J.; Westendorf, A. M.; Knuschke, T., A Tumor-Peptide-Based Nanoparticle Vaccine Elicits Efficient Tumor Growth Control in Antitumor Immunotherapy. *Mol Cancer Ther* **2019,** *18* (6), 1069-1080.
125. Howard, G. P.; Verma, G.; Ke, X.; Thayer, W. M.; Hamerly, T.; Baxter, V. K.; Lee, J. E.; Dinglasan, R. R.; Mao, H.-Q. J. N. R., Critical size limit of biodegradable nanoparticles for enhanced lymph node trafficking and paracortex penetration. **2019,** *12* (4), 837-844.
126. Carstens, M. G.; Camps, M. G.; Henriksen-Lacey, M.; Franken, K.; Ottenhoff, T. H.; Perrie, Y.; Bouwstra, J. A.; Ossendorp, F.; Jiskoot, W., Effect of vesicle size on tissue localization and immunogenicity of liposomal DNA vaccines. *Vaccine* **2011,** *29* (29-30), 4761-70.
127. Steinbuck, M. P.; Seenappa, L. M.; Jakubowski, A.; McNeil, L. K.; Haqq, C. M.; DeMuth, P. C., A Lymph Node Targeted Amphiphile Vaccine Induces Potent Cellular and Humoral Immunity to SARS-CoV-2. *bioRxiv* **2020**.
128. Mueller, S. N.; Tian, S.; DeSimone, J. M., Rapid and Persistent Delivery of Antigen by Lymph Node Targeting PRINT Nanoparticle Vaccine Carrier To Promote Humoral Immunity. *Mol Pharm* **2015,** *12* (5), 1356-65.
129. Couzin-Frankel, J., Cancer immunotherapy. *Science* **2013,** *342* (6165), 1432-1433.
130. Gubin, M. M.; Zhang, X.; Schuster, H.; Caron, E.; Ward, J. P.; Noguchi, T.; Ivanova, Y.; Hundal, J.; Arthur, C. D.; Krebber, W.-J., Checkpoint blockade cancer immunotherapy targets tumour-specific mutant antigens. *Nature* **2014,** *515* (7528), 577-581.
131. Lee, D. W.; Kochenderfer, J. N.; Stetler-Stevenson, M.; Cui, Y. K.; Delbrook, C.; Feldman, S. A.; Fry, T. J.; Orentas, R.; Sabatino, M.; Shah, N. N., T cells expressing CD19 chimeric antigen receptors for acute lymphoblastic leukaemia in children and young adults: a phase 1 dose-escalation trial. *The Lancet* **2015,** *385* (9967), 517-528.
132. Syn, N. L.; Teng, M. W.; Mok, T. S.; Soo, R. A., De-novo and acquired resistance to immune checkpoint targeting. *The Lancet Oncology* **2017,** *18* (12), e731-e741.
133. Duan, Q.; Zhang, H.; Zheng, J.; Zhang, L., Turning Cold into Hot: Firing up the Tumor Microenvironment. *Trends Cancer* **2020,** *6* (7), 605-618.
134. Sun, L.; Wu, J.; Du, F.; Chen, X.; Chen, Z. J., Cyclic GMP-AMP synthase is a cytosolic DNA sensor that activates the type I interferon pathway. *Science* **2013,** *339* (6121), 786-791.
135. Corrales, L.; Glickman, L. H.; McWhirter, S. M.; Kanne, D. B.; Sivick, K. E.; Katibah, G. E.; Woo, S.-R.; Lemmens, E.; Banda, T.; Leong, J. J., Direct activation of STING in the tumor microenvironment leads to potent and systemic tumor regression and immunity. *Cell reports* **2015,** *11* (7), 1018-1030.
136. Flood, B. A.; Higgs, E. F.; Li, S.; Luke, J. J.; Gajewski, T. F., STING pathway agonism as a cancer therapeutic. *Immunol Rev* **2019,** *290* (1), 24-38.
137. Shae, D.; Becker, K. W.; Christov, P.; Yun, D. S.; Lytton-Jean, A. K. R.; Sevimli, S.; Ascano, M.; Kelley, M.; Johnson, D. B.; Balko, J. M.; Wilson, J. T., Endosomolytic polymersomes increase the activity of cyclic dinucleotide STING agonists to enhance cancer immunotherapy. *Nat Nanotechnol* **2019,** *14* (3), 269-278.
138. Schadt, L.; Sparano, C.; Schweiger, N. A.; Silina, K.; Cecconi, V.; Lucchiari, G.; Yagita, H.; Guggisberg, E.; Saba, S.; Nascakova, Z.; Barchet, W.; van den Broek, M., Cancer-Cell-Intrinsic cGAS Expression Mediates Tumor Immunogenicity. *Cell Rep* **2019,** *29* (5), 1236-1248 e7.

139. Nicolai, C. J.; Wolf, N.; Chang, I. C.; Kirn, G.; Marcus, A.; Ndubaku, C. O.; McWhirter, S. M.; Raulet, D. H., NK cells mediate clearance of CD8(+) T cell-resistant tumors in response to STING agonists. *Sci Immunol* **2020,** *5* (45).
140. Harrington, K. J.; Brody, J.; Ingham, M.; Strauss, J.; Cemerski, S.; Wang, M.; Tse, A.; Khilnani, A.; Marabelle, A.; T., G., Preliminary results of the first-in-human study of MK-1454, an agonist of stimulator of interferon genes (STING), as monotherapy or in combination with Pembrolizumab (Pembro) in patients with advanced solid tumors or lymphomas. *ESCO, Abstract 5475* **2018**.
141. Meric-Bernstam, F.; Werner, T.; Hodi, S.; Messersmith, W.; Lewis, N.; Talluto, C.; Dostalek, M.; Tao, A.; McWhirter, S.; Trujillo, D.; Luke, J. J., Phase I dose-finding study of MIW815 (ADU-S100), an intratumoral STING agonist, in patients with advanced solid tumors or lymphomas. *SITC, Poster 309* **2018**.
142. Hood, M. I.; Skaar, E. P., Nutritional immunity: transition metals at the pathogen-host interface. *Nat Rev Microbiol* **2012,** *10* (8), 525-37.
143. Bessman, N. J.; Mathieu, J. R. R.; Renassia, C.; Zhou, L.; Fung, T. C.; Fernandez, K. C.; Austin, C.; Moeller, J. B.; Zumerle, S.; Louis, S.; Vaulont, S.; Ajami, N. J.; Sokol, H.; Putzel, G. G.; Arvedson, T.; Sockolow, R. E.; Lakhal-Littleton, S.; Cloonan, S. M.; Arora, M.; Peyssonnaux, C.; Sonnenberg, G. F., Dendritic cell-derived hepcidin sequesters iron from the microbiota to promote mucosal healing. *Science* **2020,** *368* (6487), 186-189.
144. Du, M.; Chen, Z. J., DNA-induced liquid phase condensation of cGAS activates innate immune signaling. *Science* **2018,** *361* (6403), 704-709.
145. Hou, L.; Tian, C.; Yan, Y.; Zhang, L.; Zhang, H.; Zhang, Z., Manganese-Based Nanoactivator Optimizes Cancer Immunotherapy via Enhancing Innate Immunity. *ACS Nano* **2020,** *14* (4), 3927-3940.
146. Chen, C.; Tong, Y.; Zheng, Y.; Shi, Y.; Chen, Z.; Li, J.; Liu, X.; Zhang, D.; Yang, H., Cytosolic Delivery of Thiolated Mn-cGAMP Nanovaccine to Enhance the Antitumor Immune Responses. *Small* **2021,** *17* (17), e2006970.
147. Yang, X.; Yang, Y.; Bian, J.; Wei, J.; Wang, Z.; Zhou, Z.; Li, Z.; Sun, M. J. N. T., Converting primary tumor towards an in situ STING-activating vaccine via a biomimetic nanoplatform against recurrent and metastatic tumors. **2021,** *38*, 101109.
148. Aschner, J. L.; Aschner, M., Nutritional aspects of manganese homeostasis. *Mol Aspects Med* **2005,** *26* (4-5), 353-62.
149. Wang, C., Mangafodipir trisodium (MnDPDP)-enhanced magnetic resonance imaging of the liver and pancreas. *Acta Radiol Suppl* **1998,** *415*, 1-31.
150. Takagi, Y.; Okada, A.; Sando, K.; Wasa, M.; Yoshida, H.; Hirabuki, N., Evaluation of indexes of in vivo manganese status and the optimal intravenous dose for adult patients undergoing home parenteral nutrition. *Am J Clin Nutr* **2002,** *75* (1), 112-8.
151. Pan, D.; Schmieder, A. H.; Wickline, S. A.; Lanza, G. M., Manganese-based MRI contrast agents: past, present and future. *Tetrahedron* **2011,** *67* (44), 8431-8444.
152. Lutz, M. B.; Kukutsch, N.; Ogilvie, A. L.; Rossner, S.; Koch, F.; Romani, N.; Schuler, G., An advanced culture method for generating large quantities of highly pure dendritic cells from mouse bone marrow. *J Immunol Methods* **1999,** *223* (1), 77-92.
153. Kuai, R.; Sun, X.; Yuan, W.; Xu, Y.; Schwendeman, A.; Moon, J. J., Subcutaneous Nanodisc Vaccination with Neoantigens for Combination Cancer Immunotherapy. *Bioconjug Chem* **2018,** *29* (3), 771-775.
154. Jin, L.; Hill, K. K.; Filak, H.; Mogan, J.; Knowles, H.; Zhang, B.; Perraud, A. L.; Cambier, J. C.; Lenz, L. L., MPYS is required for IFN response factor 3 activation and type I IFN production in the response of cultured phagocytes to bacterial second messengers cyclic-di-AMP and cyclic-di-GMP. *J Immunol* **2011,** *187* (5), 2595-601.
155. Li, L.; Yin, Q.; Kuss, P.; Maliga, Z.; Millan, J. L.; Wu, H.; Mitchison, T. J., Hydrolysis of 2'3'-cGAMP by ENPP1 and design of nonhydrolyzable analogs. *Nat Chem Biol* **2014,** *10* (12), 1043-8.
156. Ramanjulu, J. M.; Pesiridis, G. S.; Yang, J.; Concha, N.; Singhaus, R.; Zhang, S.-Y.; Tran, J.-L.; Moore, P.; Lehmann, S.; Eberl, H. C., Design of amidobenzimidazole STING receptor agonists with systemic activity. *Nature* **2018,** *564* (7736), 439.
157. Thanos, D.; Maniatis, T., Virus induction of human IFN beta gene expression requires the assembly of an enhanceosome. *Cell* **1995,** *83* (7), 1091-100.

158. Wang, J.; Basagoudanavar, S. H.; Wang, X.; Hopewell, E.; Albrecht, R.; Garcia-Sastre, A.; Balachandran, S.; Beg, A. A., NF-kappa B RelA subunit is crucial for early IFN-beta expression and resistance to RNA virus replication. *J Immunol* **2010,** *185* (3), 1720-9.
159. Ting, J. P.; Duncan, J. A.; Lei, Y., How the noninflammasome NLRs function in the innate immune system. *Science* **2010,** *327* (5963), 286-90.
160. Liu, S.; Cai, X.; Wu, J.; Cong, Q.; Chen, X.; Li, T.; Du, F.; Ren, J.; Wu, Y. T.; Grishin, N. V.; Chen, Z. J., Phosphorylation of innate immune adaptor proteins MAVS, STING, and TRIF induces IRF3 activation. *Science* **2015,** *347* (6227), aaa2630.
161. Shin, H. M.; Kim, M. H.; Kim, B. H.; Jung, S. H.; Kim, Y. S.; Park, H. J.; Hong, J. T.; Min, K. R.; Kim, Y., Inhibitory action of novel aromatic diamine compound on lipopolysaccharide-induced nuclear translocation of NF-kappaB without affecting IkappaB degradation. *FEBS Lett* **2004,** *571* (1-3), 50-4.
162. Smola, M.; Birkus, G.; Boura, E., No magnesium is needed for binding of the stimulator of interferon genes to cyclic dinucleotides. *Acta Crystallogr F Struct Biol Commun* **2019,** *75* (Pt 9), 593-598.
163. Kuai, R.; Yuan, W.; Son, S.; Nam, J.; Xu, Y.; Fan, Y.; Schwendeman, A.; Moon, J. J., Elimination of established tumors with nanodisc-based combination chemoimmunotherapy. *Sci Adv* **2018,** *4* (4), eaao1736.
164. Chin, E. N.; Yu, C.; Vartabedian, V. F.; Jia, Y.; Kumar, M.; Gamo, A. M.; Vernier, W.; Ali, S. H.; Kissai, M.; Lazar, D. C.; Nguyen, N.; Pereira, L. E.; Benish, B.; Woods, A. K.; Joseph, S. B.; Chu, A.; Johnson, K. A.; Sander, P. N.; Martinez-Pena, F.; Hampton, E. N.; Young, T. S.; Wolan, D. W.; Chatterjee, A. K.; Schultz, P. G.; Petrassi, H. M.; Teijaro, J. R.; Lairson, L. L., Antitumor activity of a systemic STING-activating non-nucleotide cGAMP mimetic. *Science* **2020,** *369* (6506), 993-999.
165. Pan, B. S.; Perera, S. A.; Piesvaux, J. A.; Presland, J. P.; Schroeder, G. K.; Cumming, J. N.; Trotter, B. W.; Altman, M. D.; Buevich, A. V.; Cash, B.; Cemerski, S.; Chang, W.; Chen, Y.; Dandliker, P. J.; Feng, G.; Haidle, A.; Henderson, T.; Jewell, J.; Kariv, I.; Knemeyer, I.; Kopinja, J.; Lacey, B. M.; Laskey, J.; Lesburg, C. A.; Liang, R.; Long, B. J.; Lu, M.; Ma, Y.; Minnihan, E. C.; O'Donnell, G.; Otte, R.; Price, L.; Rakhilina, L.; Sauvagnat, B.; Sharma, S.; Tyagarajan, S.; Woo, H.; Wyss, D. F.; Xu, S.; Bennett, D. J.; Addona, G. H., An orally available non-nucleotide STING agonist with antitumor activity. *Science* **2020,** *369* (6506).
166. Gajewski, T. F.; Higgs, E. F., Immunotherapy with a sting. *Science* **2020,** *369* (6506), 921-922.
167. Koshy, S. T.; Cheung, A. S.; Gu, L.; Graveline, A. R.; Mooney, D. J., Liposomal Delivery Enhances Immune Activation by STING Agonists for Cancer Immunotherapy. *Adv Biosyst* **2017,** *1* (1-2).
168. Tan, Y. S.; Sansanaphongpricha, K.; Xie, Y.; Donnelly, C. R.; Luo, X.; Heath, B. R.; Zhao, X.; Bellile, E.; Hu, H.; Chen, H.; Polverini, P. J.; Chen, Q.; Young, S.; Carey, T. E.; Nor, J. E.; Ferris, R. L.; Wolf, G. T.; Sun, D.; Lei, Y. L., Mitigating SOX2-potentiated Immune Escape of Head and Neck Squamous Cell Carcinoma with a STING-inducing Nanosatellite Vaccine. *Clin Cancer Res* **2018,** *24* (17), 4242-4255.
169. Liu, Y.; Crowe, W. N.; Wang, L.; Lu, Y.; Petty, W. J.; Habib, A. A.; Zhao, D., An inhalable nanoparticulate STING agonist synergizes with radiotherapy to confer long-term control of lung metastases. *Nat Commun* **2019,** *10* (1), 5108.
170. He, Y.; Hong, C.; Yan, E. Z.; Fletcher, S. J.; Zhu, G.; Yang, M.; Li, Y.; Sun, X.; Irvine, D. J.; Li, J.; Hammond, P. T., Self-assembled cGAMP-STINGDeltaTM signaling complex as a bioinspired platform for cGAMP delivery. *Sci Adv* **2020,** *6* (24), eaba7589.
171. Li, S.; Luo, M.; Wang, Z.; Feng, Q.; Wilhelm, J.; Wang, X.; Li, W.; Wang, J.; Cholka, A.; Fu, Y. X.; Sumer, B. D.; Yu, H.; Gao, J., Prolonged activation of innate immune pathways by a polyvalent STING agonist. *Nat Biomed Eng* **2021**.
172. Liu, D.; Poon, C.; Lu, K.; He, C.; Lin, W., Self-assembled nanoscale coordination polymers with trigger release properties for effective anticancer therapy. *Nat Commun* **2014,** *5*, 4182.
173. Liu, J.; Yang, G.; Zhu, W.; Dong, Z.; Yang, Y.; Chao, Y.; Liu, Z., Light-controlled drug release from singlet-oxygen sensitive nanoscale coordination polymers enabling cancer combination therapy. *Biomaterials* **2017,** *146*, 40-48.
174. Yang, Y.; Xu, L.; Zhu, W.; Feng, L.; Liu, J.; Chen, Q.; Dong, Z.; Zhao, J.; Liu, Z.; Chen, M., One-pot synthesis of pH-responsive charge-switchable PEGylated nanoscale coordination polymers for improved cancer therapy. *Biomaterials* **2018,** *156*, 121-133.
175. Sivick, K. E.; Desbien, A. L.; Glickman, L. H.; Reiner, G. L.; Corrales, L.; Surh, N. H.; Hudson, T. E.; Vu, U. T.; Francica, B. J.; Banda, T.; Katibah, G. E.; Kanne, D. B.; Leong, J. J.; Metchette, K.; Bruml, J. R.; Ndubaku, C. O.; McKenna, J. M.; Feng, Y.; Zheng, L.; Bender, S. L.; Cho, C. Y.; Leong, M. L.; van

Elsas, A.; Dubensky, T. W., Jr.; McWhirter, S. M., Magnitude of Therapeutic STING Activation Determines CD8(+) T Cell-Mediated Anti-tumor Immunity. *Cell Rep* **2018,** *25* (11), 3074-3085 e5.
176. Luo, X.; Donnelly, C. R.; Gong, W.; Heath, B. R.; Hao, Y.; Donnelly, L. A.; Moghbeli, T.; Tan, Y. S.; Lin, X.; Bellile, E.; Kansy, B. A.; Carey, T. E.; Brenner, J. C.; Cheng, L.; Polverini, P. J.; Morgan, M. A.; Wen, H.; Prince, M. E.; Ferris, R. L.; Xie, Y.; Young, S.; Wolf, G. T.; Chen, Q.; Lei, Y. L., HPV16 drives cancer immune escape via NLRX1-mediated degradation of STING. *J Clin Invest* **2020,** *130* (4), 1635-1652.
177. Lewis, R.; Tatken, R., Registry of Toxic Effects of Chemical Substances, Vol. 1. *US Department of Health and Human Services, National Institute for Occupational Safety and Health, Washington, DC* **1980**, 252.
178. Greger, J. L., Nutrition versus toxicology of manganese in humans: evaluation of potential biomarkers. *Neurotoxicology* **1999,** *20* (2-3), 205-12.
179. Mounicou, S.; Szpunar, J.; Lobinski, R., Metallomics: the concept and methodology. *Chem Soc Rev* **2009,** *38* (4), 1119-38.
180. Palermo, G.; Spinello, A.; Saha, A.; Magistrato, A., Frontiers of metal-coordinating drug design. *Expert Opin Drug Discov* **2021,** *16* (5), 497-511.
181. Haas, K. L.; Franz, K. J., Application of metal coordination chemistry to explore and manipulate cell biology. *Chem Rev* **2009,** *109* (10), 4921-60.
182. Cohen, S. M., A Bioinorganic Approach to Fragment-Based Drug Discovery Targeting Metalloenzymes. *Acc Chem Res* **2017,** *50* (8), 2007-2016.
183. Johnson, S.; Barile, E.; Farina, B.; Purves, A.; Wei, J.; Chen, L. H.; Shiryaev, S.; Zhang, Z.; Rodionova, I.; Agrawal, A.; Cohen, S. M.; Osterman, A.; Strongin, A.; Pellecchia, M., Targeting metalloproteins by fragment-based lead discovery. *Chem Biol Drug Des* **2011,** *78* (2), 211-23.
184. Guthrie, L. M.; Soma, S.; Yuan, S.; Silva, A.; Zulkifli, M.; Snavely, T. C.; Greene, H. F.; Nunez, E.; Lynch, B.; De Ville, C.; Shanbhag, V.; Lopez, F. R.; Acharya, A.; Petris, M. J.; Kim, B. E.; Gohil, V. M.; Sacchettini, J. C., Elesclomol alleviates Menkes pathology and mortality by escorting Cu to cuproenzymes in mice. *Science* **2020,** *368* (6491), 620-625.
185. Paredes, R. M.; Etzler, J. C.; Watts, L. T.; Zheng, W.; Lechleiter, J. D., Chemical calcium indicators. *Methods* **2008,** *46* (3), 143-51.
186. Li, J.; Chen, Y. C.; Tseng, Y. C.; Mozumdar, S.; Huang, L., Biodegradable calcium phosphate nanoparticle with lipid coating for systemic siRNA delivery. *J Control Release* **2010,** *142* (3), 416-21.
187. Soetaert, F.; Korangath, P.; Serantes, D.; Fiering, S.; Ivkov, R., Cancer therapy with iron oxide nanoparticles: Agents of thermal and immune therapies. *Adv Drug Deliv Rev* **2020,** *163-164*, 65-83.
188. Yoo, J. W.; Irvine, D. J.; Discher, D. E.; Mitragotri, S., Bio-inspired, bioengineered and biomimetic drug delivery carriers. *Nature reviews. Drug discovery* **2011,** *10* (7), 521-35.
189. Irvine, D. J.; Hanson, M. C.; Rakhra, K.; Tokatlian, T., Synthetic Nanoparticles for Vaccines and Immunotherapy. *Chem Rev* **2015,** *115* (19), 11109-46.
190. Schudel, A.; Francis, D. M.; Thomas, S. N., Material design for lymph node drug delivery. *Nat Rev Mater* **2019,** *4* (6), 415-428.
191. Crucho, C. I., Stimuli-responsive polymeric nanoparticles for nanomedicine. *ChemMedChem* **2015,** *10* (1), 24-38.
192. El-Sawy, H. S.; Al-Abd, A. M.; Ahmed, T. A.; El-Say, K. M.; Torchilin, V. P., Stimuli-Responsive Nano-Architecture Drug-Delivery Systems to Solid Tumor Micromilieu: Past, Present, and Future Perspectives. *ACS Nano* **2018,** *12* (11), 10636-10664.
193. Li, F.; Qin, Y.; Lee, J.; Liao, H.; Wang, N.; Davis, T. P.; Qiao, R.; Ling, D., Stimuli-responsive nano-assemblies for remotely controlled drug delivery. *J Control Release* **2020,** *322*, 566-592.
194. Li, L.; Yang, W. W.; Xu, D. G., Stimuli-responsive nanoscale drug delivery systems for cancer therapy. *J Drug Target* **2019,** *27* (4), 423-433.
195. Ni, K.; Luo, T.; Nash, G. T.; Lin, W., Nanoscale Metal-Organic Frameworks for Cancer Immunotherapy. *Acc Chem Res* **2020,** *53* (9), 1739-1748.